Patrick Jenny, BSc

The Structure of the Higgs and Electroweak Vector Bosons

A First Study of Electroweak Quasi-PDFs on the Lattice

MASTER'S THESIS

to achieve the university degree of
Master of Science
Master's degree program: Physics

submitted to

Graz University of Technology

Supervisor

Prof. Dr. Axel Maas
Institute of Physics
University of Graz

Graz, June 21, 2026

ABSTRACT

In the standard perturbative approach to describe electroweak scattering, elementary states are used as asymptotic scattering states. This approach yields results that show remarkable agreement with experimental data. However, these elementary states are not gauge-invariant and consequently cannot represent physical asymptotic states. From a theoretical standpoint, composite objects, similar to hadrons in QCD, provide a more appropriate description. This gauge-invariant formulation goes back to the work of Fröhlich, Morchio, and Strocchi and is commonly referred to as the FMS mechanism.

If electroweak states are indeed composite, it is natural to ask whether methods analogous to those developed for hadrons in QCD can be used to study their internal structure. Scattering experiments involving hadrons are described using Parton Distribution Functions (PDFs), which capture the non-perturbative aspects and structure of these composite objects. The calculation of PDFs from first principles on the lattice has become feasible in recent years through the quasi-PDF approach, which relates lattice-computable spatial correlation functions to the corresponding PDFs.

In this work, we extend and implement the quasi-PDF framework in an SU(2) gauge–scalar theory. In particular, we calculate several quasi-PDF channels of the physical Higgs and electroweak vector bosons on the lattice. The resulting distributions show nontrivial structure consistent with the composite description employed in the FMS framework. Furthermore, this work demonstrates the feasibility of applying the quasi-PDF framework in a reduced electroweak sector of the Standard Model. Future collider experiments may uncover electroweak compositeness, for which this work opens a PDF-based theoretical description.

KURZFASSUNG

Im üblichen perturbativen Ansatz zur Beschreibung elektroschwacher Streuprozesse werden elementare Felder als asymptotische Streuzustände verwendet. Dieser Ansatz liefert Ergebnisse, die eine bemerkenswerte Übereinstimmung mit den experimentellen Daten zeigen. Diese elementaren Zustände sind jedoch nicht eichinvariant und können deshalb keine physikalischen asymptotischen Zustände darstellen. Aus theoretischer Sicht bieten zusammengesetzte Objekte, ähnlich den Hadronen in der QCD, eine geeignetere Beschreibung. Diese eichinvariante Formulierung geht zurück auf die Arbeiten von Fröhlich, Morchio, und Strocchi und ist unter dem Namen FMS-Mechanismus bekannt.

Wenn elektroschwache Zustände tatsächlich zusammengesetzte Objekte sind, liegt die Frage nahe, ob Methoden, die für Hadronen in der QCD entwickelt wurden, auch zur Untersuchung ihrer inneren Struktur eingesetzt werden können. Streuprozesse mit Hadronen werden mithilfe von Partonverteilungsfunktionen (PDFs) beschrieben, welche die nichtperturbative Struktur dieser zusammengesetzten Objekte erfassen. Die Berechnung dieser PDFs auf Grundlage fundamentaler Prinzipien auf dem Gitter ist in den letzten Jahren im Rahmen des Quasi-PDF-Ansatzes möglich geworden. Dieser stellt eine Verbindung zwischen auf dem Gitter berechenbaren räumlichen Korrelationsfunktionen und den entsprechenden PDFs her.

In dieser Arbeit erweitern und implementieren wir das Quasi-PDF-Framework in einer SU(2)-Eich-Skalar-Theorie. Insbesondere berechnen wir verschiedene Quasi-PDF-Kanäle des physikalischen Higgs-Bosons sowie der elektroschwachen Vektorbosonen auf dem Gitter. Die resultierenden Verteilungen zeigen eine nichttriviale Struktur, die mit der zusammengesetzten Beschreibung des FMS-Mechanismus vereinbar ist. Darüber hinaus demonstriert diese Arbeit die Anwendbarkeit des Quasi-PDF-Frameworks in einem vereinfachten elektroschwachen Sektor des Standardmodells. Zukünftige Collider-Experimente könnten Hinweise auf Kompositheit elektroschwacher Zustände liefern, wofür diese Arbeit eine theoretische Beschreibung auf Basis von PDFs eröffnet.

Acknowledgments

I would like to express my sincere gratitude to my supervisor, Axel Maas, for guiding me through this thesis and for offering his theoretical insights whenever I needed help. I am also grateful to Georg Wieland for carrying out the generation of the lattice configurations and for the valuable discussions. I would further like to thank all the members of the Department of Theoretical Physics for providing a welcoming and inspiring environment throughout my studies.

Completing my studies would not have been possible without the support of my friends in Graz, whom I came to appreciate deeply during my years there. What began as a small group in the first semester, where each study session was somehow both shorter and longer than planned, quickly grew into a larger circle of lasting friendships. The trips we took were always a welcome change of pace.

A special word of appreciation is also due for my roommates throughout the years in Graz. In particular, I would like to mention Joshua and David, with whom I share four years' worth of memories across two different flats. They made sure that many long days ended with discussions considerably less demanding than those at the university, although occasionally the opposite was true.

In the final months of this thesis, I had the pleasure of spending much time with Miriam. Thank you for your encouragement, support, and company during this final stretch.

Finally, I would like to thank all those who accompanied me throughout these years, whether mentioned here by name or not. Your friendship and encouragement have meant a great deal to me.

Lastly, I would like to thank my family and, in particular, my mother, whose unwavering support I could always rely on and who made this entire endeavor possible in the first place. Throughout my studies, she understood that some goals require both time and persistence. I am deeply grateful for the trust she showed along the way. I would also like to remember my father, who helped shape the person who started this journey.

The author used ChatGPT, DeepL, and LanguageTool for proofreading and linguistic refinement of the thesis. All scientific content, analysis, interpretation of the results, and conclusions were developed independently by the author.

Let's see what comes next.

Contents

List of Figures

List of Tables

Chapter 1.

Introduction

The Standard Model (SM) of particle physics represents one of the most precisely tested theoretical frameworks in modern physics. It has been tested across a wide range of energies and experimental settings [1]. Despite its predictive success, various theoretical arguments indicate that the Standard Model cannot be the ultimate description, but should rather be regarded as an effective low-energy theory. For example, the exact cancellation of the gauge anomalies hints at a deeper organizing principle [2]. In addition, astrophysical observations provide strong evidence for dark matter, which cannot be explained within the Standard Model. Various replacements and extensions of the Standard Model have been theorized, usually collected under the term Beyond the Standard Model (BSM) theories, which try to resolve theoretical shortcomings and unaccounted-for experimental observations. However, in the absence of any definitive experimental signals, they remain speculative.

Presently, the primary experimental tool is the use of high-energy particle colliders, which allows for precision measurements in a controlled environment. Due to this precision, even small deviations from the SM prediction may be interpreted as a signal of new physics. In the past, tensions between prediction and experiment could often be resolved within the Standard Model itself, as in the case of the anomalous magnetic moment of the muon, a high-precision observable, where the apparent tension was resolved through improved Standard Model calculations [3]. Therefore, rigorous theoretical descriptions are needed to prevent false positives in searches for new physics.

In the perturbative treatment of the electroweak sector of the Standard Model, elementary fields are treated as the physical degrees of freedom. However, strict field-theoretical arguments, in particular the requirement of gauge invariance, indicate that composite objects are the appropriate physical description. This naturally raises the question of why the perturbative calculations still provide results that are in remarkable agreement with the experimental data. The Fröhlich–Morchio–Strocchi (FMS) mechanism resolves this issue by showing that the gauge-invariant description reproduces the same results, to a good approximation, as the perturbative description.

This situation may change in future experiments, for example, at the proposed FCC-ee collider [4], where deviations from the perturbative prediction could arise [5]. In collider experiments, such effects are probed through measurements of scattering cross sections.

Cross sections involving electroweak composite objects can be calculated using augmented perturbation theory [6], a gauge-invariant extension of standard perturbation theory. Alternatively, one can employ a framework originating in hadron physics, namely parton distribution functions (PDFs). In this approach, the cross section is factorized into a perturbative and a non-perturbative contribution, with the latter encoded in the PDFs that reflect the internal structure of the bound state. Parton in this context corresponds to an elementary field inside the gauge-invariant bound states predicted by the FMS mechanism. The calculation of these PDFs from first principles on the lattice has become feasible recently through the use of quasi-PDFs.

Electroweak parton distribution functions, including both gauge-boson and Higgs contributions, have also been discussed for hadronic bound states in the context of high-energy collisions [7–10]. They have likewise been studied in the context of high-energy lepton colliders, where they provide an effective description of electroweak radiation off elementary leptons [11–14].

At particle colliders, both the initial and final states are fermionic, and as a consequence, the quantities of primary interest are the PDFs of fermionic bound states. The present work, however, does not aim to provide a direct application to collider observables such as PDFs for lepton–lepton colliders. Instead, this thesis is an initial study of electroweak PDFs from the lattice, and thus neither fermionic bound states nor leptonic PDFs are considered.

In this work, we investigate the substructure of the physical electroweak bound states by computing quasi-PDFs in a simplified electroweak gauge–scalar theory using lattice methods. In particular, we calculate the W/Z-like and Higgs-like quasi-PDFs of the physical vector boson and the Higgs state. In chapter 2, we provide the theoretical background underlying this study, including gauge invariance, composite physical states, and the relevant features of the electroweak sector. An introduction to lattice field theory and the lattice formulation of the gauge–scalar theory employed in this work is given in chapter 3. The specific quasi-parton distribution functions, along with their lattice implementation, are defined and discussed in chapter 4. Details of the numerical setup and simulation strategy are presented in chapter 5. Chapter 6 contains an analysis of the resulting quasi-PDFs and their properties. The thesis concludes in chapter 7 with a summary and outlook.

Chapter 2.

Theoretical Background

This chapter introduces the theoretical framework underlying the present work. We begin with a brief review of the electroweak theory and the corresponding SU(2) gauge–scalar theory. Next, we discuss the gauge-invariant description of physical states and the concept of parton distribution functions.

2.1. Electroweak Theory

The Standard Model of particle physics consists of two main parts: quantum chromodynamics and the electroweak theory. The latter combines the weak and electromagnetic interactions into a single theoretical framework. From an experimental perspective, these interactions are mediated via the (massive) $\mathrm{W}^{\pm}$- and Z-bosons as well as the (massless) photons. These particles correspond to the physical mass eigenstates. The electroweak theory is formulated as a Yang–Mills theory based on the gauge group $\mathrm{SU}(2)_\mathrm{L} \times \mathrm{U}(1)_\mathrm{Y}$. The non-abelian group $\mathrm{SU}(2)_\mathrm{L}$ acts only on the left-handed fermions, reflecting the chiral nature of the theory, whereas the $\mathrm{U}(1)_\mathrm{Y}$ corresponds to the weak hypercharge.

In principle, gauge invariance of a Yang–Mills theory requires the gauge bosons to be massless, which conflicts with the observed massive exchange particles. This contradiction is resolved via the Brout–Englert–Higgs (BEH) mechanism, which, loosely speaking, gives masses to the gauge bosons via the introduction of a complex scalar doublet. In order for the BEH effect to take place, the Lagrangian needs to include a potential of the scalar field, which allows for a non-trivial minimum. In the standard literature, it is then said that the gauge symmetry is spontaneously broken according to $\mathrm{SU}(2)_\mathrm{L} \times \mathrm{U}(1)_\mathrm{Y} \to \mathrm{U}(1)_\mathrm{em}$ and the breaking introduces a mass term for the gauge boson.

In a chiral gauge theory, it is not possible to add an explicit fermion mass term to the Lagrangian, as such a term is not permitted by gauge invariance. However, fermion masses can arise through Yukawa couplings between the fermions and the scalar field, which introduce masses after symmetry breaking [2].

2.2. SU(2) Gauge–Scalar Theory

Simulations of the whole electroweak sector of the Standard Model are not feasible on the lattice. Therefore, this work focuses on a subpart, namely the SU(2) gauge–scalar theory. In this framework, fermions are neglected and the gauge group is reduced to SU(2). As a consequence, this alteration means the theory contains three degenerate massive gauge bosons.

The SU(2) gauge–scalar theory is defined by the Lagrangian

$$\begin{gathered}\mathcal{L} = -\frac{1}{4} W^a_{\mu\nu} W^{a\mu\nu} + (D_\mu \phi)^\dagger (D^\mu \phi) + \lambda(\phi^\dagger \phi - f^2)^2 \\ W^a_{\mu\nu} = \partial_\mu W^a_\nu - \partial_\nu W^a_\mu + g\epsilon^{abc} W^b_\mu W^c_\nu \quad \text{and} \quad D_\mu = \partial_\mu - igW^a_\mu \tau^a\end{gathered} \tag{2.1}$$

where ϕ denotes the complex scalar doublet and W^a_μ the gauge field and $W^a_{\mu\nu}$ the corresponding field strength tensor. We furthermore introduce the generators of the $\mathfrak{su}(2)$ Lie algebra $\tau^a = \frac{\sigma^a}{2}$. with σ^a the Pauli matrices, and ϵ^{abc} denotes the $\mathfrak{su}(2)$ structure constants. The parameters of the theory are the gauge coupling g, the scalar self-coupling λ, and the potential parameter f. For later convenience, we also introduce $\mu^2 = \lambda f^2$.

Under a local gauge transformation $G(x) \in \mathrm{SU}(2)$ the fields transform according to

$$W_\mu(x) \to G(x) W_\mu(x) G^\dagger(x) - \frac{i}{g} \left(\partial_\mu G(x)\right) G^\dagger(x) \quad \text{and} \quad \phi(x) \to G(x)\phi(x)\,, \tag{2.2}$$

where $W_\mu = W^a_\mu \tau^a$.

The standard perturbative approach is to expand the scalar field around the (classical) minimum at $\phi^\dagger\phi = f^2$ and to identify $v = \sqrt{2} f$

$$\phi(x) = \langle\phi\rangle + \eta(x) = \frac{v}{\sqrt{2}} N + \eta(x) \quad \text{with} \quad |N| = 1 \quad \text{and} \quad \langle H \rangle = 0 \tag{2.3}$$

The constant part $\langle\phi\rangle = \frac{v}{\sqrt{2}} N$ is the vacuum expectation value (VEV). A more convenient parametrization of Eq. (2.3) is the following

$$\phi(x) = \exp\left(2i \frac{\pi^a(x)\tau^a}{v}\right) \begin{pmatrix} 0 \\ \frac{v}{\sqrt{2}} + \frac{h(x)}{\sqrt{2}} \end{pmatrix} \tag{2.4}$$

where h is the field that is usually called the Higgs field. By fixing to unitary gauge ($\pi^a(x) = 0$) and inserting the expression for the scalar field from Eq. (2.4) back into the Lagrangian Eq. (2.1) one obtains mass terms for both the gauge fields as well as the Higgs field

$$\mathcal{L}_{\text{mass}} = \frac{1}{8} g^2 v^2 \left(W^a_\mu\right)^2 - 2\mu^2 h^2 = \frac{1}{2} m^2_{\mathrm{W}} \left(W^a_\mu\right)^2 - \frac{1}{2} m^2_{\mathrm{H}} h^2$$

An essential property of the SU(2) gauge–scalar theory for the analysis in this work is the custodial symmetry. This symmetry becomes apparent when the four degrees of freedom of the complex scalar doublet are considered, and the invariance of the potential in the Lagrangian Eq. (2.1), $V(\phi) = (\phi^\dagger\phi - f^2)^2$, under an O(4) transformation is considered. When gauging the subgroup SU(2), we obtain an additional global SU(2) symmetry – the custodial symmetry. This global group introduces a conserved quantum number called custodial charge. The fact that the custodial symmetry and the gauge symmetry are the same group is a special case for the theory at hand.

Extension to Fermions

The main focus of this work is the SU(2) gauge–scalar theory. However, one of the investigated parameter sets additionally includes fermionic degrees of freedom. While no fermionic observables are evaluated in this work, this allows, at least indirectly, to assess their influence on our observables. We therefore introduce N_g mass-degenerate generations of vectorial leptons. The Lagrangian is given by

$$\mathcal{L}_{\text{Fermion}} = \sum_{g=1}^{N_g} \bar{\psi}_g \left(i\not{D} - m\right) \psi_g \,. \tag{2.5}$$

This choice of fermionic action is well motivated and discussed in detail in Ref. [15]. Although the ultimate goal is to include fermionic observables directly, this formulation should be considered a first step toward this goal, with further developments left for future work [16].

2.3. Gauge-Invariant Formulation and Physical States

The preceding discussion was formulated in terms of elementary fields. To identify the physical states of the theory, however, a gauge-invariant description is required. For reviews of this topic see [6, 17].

There is an issue with the prior considerations that cannot be disregarded. Elitzur's theorem [18] states that only gauge-invariant operators can have non-vanishing expectation values and therefore gauge symmetries cannot be spontaneously broken. In the standard perturbative approach, this fact is hidden by choosing a specific gauge which breaks the gauge symmetry explicitly. Furthermore, if the perturbative states are treated as the physical ones, this gauge choice leads to ambiguities in the resulting physical observables. For example, there exist gauges in which $\langle\phi\rangle = 0$ holds and the gauge bosons remain massless. Since this cannot be the case, this perturbative description needs to be modified and different objects must be identified as the physical states.

The resolution of this apparent contradiction was provided by Fröhlich, Morchio and

Strocchi [19, 20]. They showed that the physical states must be described by gauge-invariant operators which are necessarily composite. Gauge-invariant operators can only be classified by their global quantum numbers, meaning primarily spin J and parity P. Additionally we have the custodial charge $\mathcal{C}$ introduced in the previous section and can therefore label our states according to $J^P_{\mathcal{C}}$.

To make the connection to perturbation theory we need to find states with similar properties as the elementary fields, i.e. same spin and parity. Starting with the analog to the elementary Higgs, with quantum numbers $J^P_{\mathcal{C}} = 0^+_0$, we can write down the following gauge-invariant operator

$$\mathcal{O}^{0^+_0}(x) = \phi^\dagger(x)\phi(x) = \frac{1}{2}\,\mathrm{Tr}\Big\{\chi^\dagger(x)\chi(x)\Big\} \quad \text{with} \quad \chi = \begin{pmatrix} \phi_1 & -\phi_2^* \\ \phi_2 & \phi_1^* \end{pmatrix}, \tag{2.6}$$

where we introduce the matrix notation of the scalar doublet χ. We will refer to this operator as the physical Higgs, or spin-0 singlet, in the remainder of this work.

Similar considerations for the elementary gauge fields yield the following gauge-invariant composite with quantum numbers $J^P_{\mathcal{C}} = 1^-_1$

$$\mathcal{O}^{1^-_1\,a}_\mu(x) = \frac{1}{2}\,\mathrm{Tr}\Big\{\tau^a\chi^\dagger(x)D_\mu\chi(x)\Big\}\,. \tag{2.7}$$

This operator transforms as a triplet under the custodial symmetry and will henceforth be referred to as physical vector bosons, or equivalently as the spin-1 triplet. A crucial property of the SU(2) gauge–scalar theory is that both the local gauge symmetry and the global custodial symmetry coincide. As a consequence, a one-to-one mapping exists between the elementary fields W^a_μ and the physical vector bosons, with both transforming in triplet representations.

Turning to the second question, the success of the perturbative description can be understood as follows. The gauge-invariant operators can be rewritten using the split in Eq. (2.3). At the level of correlation functions, this corresponds to an expansion in the VEV v, with the leading contribution corresponding to the standard perturbative term. This expansion is known as the Fröhlich–Morchio–Strocchi (FMS) mechanism [19, 20]. Additionally, one can combine the FMS mechanism with standard perturbation theory, corresponding to an expansion in both the gauge coupling and v. This reproduces the perturbative mass spectrum and, given the parameter values for the Standard Model, also explains why the perturbative description fits the observations so well.

The important consequence for this work is that the asymptotic scattering states cannot be identified with elementary fields. Instead, we need gauge-invariant operators, which correspond to composite and spatially extended objects, analogous to hadrons in QCD. This analogy suggests a partonic description based on that used to describe scattering in the strong sector. While current experiments are not sensitive to this distinction, this may change in the future. Consequently, this compositeness should be taken into account for our experimental descriptions.

2.4. Parton Distribution Functions (PDFs)

The physical states discussed in the previous section are composite objects and therefore possess a non-trivial internal structure. Parton distribution functions provide a framework for describing this structure. We follow the treatment of the topic in [21].

The parton model was initially proposed for quantum chromodynamics by Feynman and Bjorken [22, 23], to describe deep inelastic scattering. The basic idea is that a nucleon in high-energy scattering processes can be described as a collection of free massless partons. Denoting the nucleon momentum by $\mathbf{p}$ and the momentum of the parton by $\hat{\mathbf{p}}_i$, and splitting the parton momentum into a longitudinal part and a transverse part $\hat{\mathbf{p}}_i^{\mathrm{T}}$, we have

$$\hat{\mathbf{p}}_i = x_i \mathbf{p} + \hat{\mathbf{p}}_i^{\mathrm{T}} \qquad \mathbf{p}\hat{\mathbf{p}}_i = 0 \qquad x_i \geq 0 \qquad \sum_i x_i = 1 \,. \tag{2.8}$$

Here x_i denotes the longitudinal momentum fraction. For the parton model, the scattering is most naturally described in the infinite momentum frame, with M the rest mass of the nucleon and $Q^2 = -q^2$. The four-vectors are then defined as

$$q^\mu = \left(0, 0, 0, \sqrt{Q^2}\right) \qquad p^\mu = \left(\sqrt{M^2 + p^2}, 0, 0, p\right). \tag{2.9}$$

Considering the limit $p \to \infty$[1] and neglecting any transverse momentum $\hat{\mathbf{p}}_i^{\mathrm{T}}$ the parton four-momentum can approximately be described by having momentum fraction x_i of the nucleon's four-momentum, thus

$$\hat{p}_i^\mu \approx \left(x_i p^0, 0, 0, x_i p\right) = x_i p^\mu \,. \tag{2.10}$$

Consequently, one can then define the parton distribution function $f^i_{\mathcal{N}}(x)$, where $f^i_{\mathcal{N}}(x)\,\mathrm{d}x$ is the probability of probing parton i carrying a momentum fraction between x and $x + \mathrm{d}x$ in the nucleon. The total cross section of the DIS process can then be written as a sum over all elementary parton–lepton cross sections, multiplied by their PDFs and integrated over all possible momentum fractions x, so that

$$\sigma(e^- \mathcal{N} \to e^- X) = \sum_i \int_0^1 \mathrm{d}x\, f^i_{\mathcal{N}}(x) \hat{\sigma}(e^- p_i \to e^- X) \,.$$

This simple image serves only as an initial illustration of the concept of PDFs, and especially the probabilistic interpretation of PDFs breaks down beyond tree-level. However, in a more general framework, we can still factorize the cross section into a perturbative part, namely the cross sections of the elementary particles, and a non-perturbative part, the parton distribution functions. These PDFs are universal quantities, meaning they depend solely on the hadron and the type of parton, not on the specific process, i.e., the

[1] This is also known as the Bjorken limit [21].

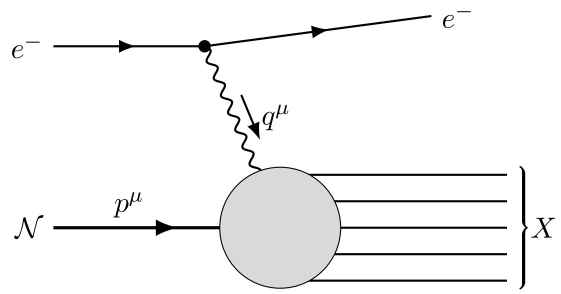

Fig. 2.1.: Kinematics of deep-inelastic lepton–hadron scattering. Figure adapted from Ref. [21].

interacting vector boson. This factorization can be written schematically as

$$\sigma = \sum_i f_i(x) \otimes \sigma_i \, . \tag{2.11}$$

This concept is not exclusive to QCD and can also be applied to the weak sector. In particular, it allows us to write cross sections involving the physical composite states predicted by the FMS mechanism in a PDF-type language. For example, considering the pair-production process $e^+e^- \to \bar{f}f$ in a gauge-invariant formulation, and denoting the composite initial and final states with capital letters, we can calculate the cross section of $E^+E^- \to \bar{F}F$ as [5]

$$\sigma_{E^+E^-\to\bar{F}F}(s) = \sum_i \int_0^1 \mathrm{d}x \int_0^1 \mathrm{d}y \, f_i(x) f_i(y) \sigma_{\bar{i}i\to\bar{f}f} \, , \tag{2.12}$$

where the f_i denotes the PDF and $\sigma_{\bar{i}i\to\bar{f}f}$ is the perturbative cross section of the elementary 'partons'.

After this brief introduction to the PDF framework, we conclude this section by providing the standard expression for the unpolarized quark PDF $f_q(x)$. This represents the corresponding PDF for the DIS process discussed above and serves as reference, as it is the most commonly discussed type of PDF in the literature. For derivations, we refer to [2]. It is given by

$$f_q(x) = \int_{-\infty}^{\infty} \frac{\mathrm{d}\xi^-}{4\pi} e^{-ixP^+\xi^-} \left\langle P|\bar{\psi}(\xi^-)\gamma^+\Omega(\xi^-,0)\psi(0)|P\right\rangle \, , \tag{2.13}$$

where $|P\rangle$ denotes the nucleon state with momentum P_μ, the light-cone components are defined as $v^\pm = (v^0 \pm v^3)/\sqrt{2}$, and $\Omega(\xi^-,0)$ denotes the gauge connection between the two light-cone points.

Chapter 3.

Lattice Formulation

Parton distribution functions are intrinsically non-perturbative objects, which motivates their study using lattice field theory. In this chapter, we provide a brief introduction to lattice field theory. Only the concepts and objects relevant to this work are discussed. For a general and more extensive introduction to lattice gauge theory, we refer the reader to [24, 25].

The main goal of lattice field theory is to calculate path integrals directly using numerical methods. The first step is to perform a Wick rotation such that the theory is formulated in Euclidean spacetime. The path integral then takes the form:

$$\langle \mathcal{O} \rangle = \frac{1}{Z} \int \mathcal{D}\Phi e^{-S_E} \mathcal{O} \tag{3.1}$$

where Φ denotes the generic field(s).

The exponential weight e^{-S_E} can be interpreted as a probability distribution. After discretizing the spacetime with lattice spacing a and finite extent $L = Na$, Monte Carlo methods can be used to generate field configurations $\Phi^{(i)}$, distributed according to this weight. A general observable can then be estimated as

$$\langle \mathcal{O} \rangle = \lim_{N \to \infty} \frac{1}{N} \sum_i^N \mathcal{O}\left[\Phi^{(i)}\right] \; . \tag{3.2}$$

In the following, we will apply these considerations to the SU(2) gauge–scalar theory.

3.1. Lattice Action

The first step in simulating the SU(2) gauge–scalar theory on the lattice is to obtain a discretized version of the Lagrangian in Eq. (2.1) and to sum over the space–time volume to arrive at the action S. This is a well-known procedure and can be found in the standard literature on lattice field theory (see, e.g., [25]). We follow the notation provided in [26]. The discretized action is then given by:

$$S = \sum_{x\in\Lambda}\left[\frac{\beta}{2}\sum_{\mu<\nu}\mathrm{Re}\{\mathrm{Tr}\{1-U_{\mu\nu}(x)\}\} + \phi^\dagger(x)\phi(x) + \gamma\left(\phi^\dagger(x)\phi(x)-1\right)^2 \right.$$
$$\left. - 2\kappa\sum_{\mu}\mathrm{Re}\Big\{\phi^\dagger(x)U_\mu(x)\phi(x+\hat{\mu})\Big\}\right] \quad (3.3)$$

with β the gauge coupling, κ the hopping parameter, and γ the quartic coupling. Instead of the gauge fields used in the continuum, the action on the lattice is written in terms of the link variables $U_\mu(x)$, which are SU(2)-valued. Under a gauge transformation they transform as

$$U_\mu(x) \to G(x)U_\mu(x)G^\dagger(x+\hat{\mu}) \quad (3.4)$$

and the following relation holds:

$$U_{-\mu}(x) = U^\dagger(x-\hat{\mu})\,. \quad (3.5)$$

We also introduce the plaquette $U_{\mu\nu}$ as the basic quantity in the gauge part of the action, which will be used again later on. It is defined as

$$U_{\mu\nu}(x) = U_\mu(x)U_\nu(x+\hat{\mu})U_\mu^\dagger(x+\hat{\nu})U_\nu^\dagger(x)\,. \quad (3.6)$$

The gauge links are related to the continuum field by

$$W_\mu(x) = \frac{1}{2agi}\left(U_\mu(x)-U_\mu^\dagger(x)\right) + \mathcal{O}(a^2) \quad \Leftrightarrow \quad U_\mu(x) = \exp\left\{iaW_\mu(x)\right\}\,, \quad (3.7)$$

and the lattice parameters are related to the continuum parameters by

$$\beta = \frac{4}{g^2}\,, \quad (3.8)$$
$$-2a^2\mu^2 = \frac{1-2\gamma}{\kappa} - 8\,, \quad (3.9)$$
$$\lambda = \frac{\gamma}{\kappa^2}\,. \quad (3.10)$$

Some further remarks should be made at this point. First of all, we set the lattice spacing $a=1$ for the rest of this work and therefore work in lattice units. Secondly, we will also assume an isotropic lattice, meaning $L_\mu = L$ and therefore the total volume is L^4. Lastly, we will use periodic boundary conditions which means that,

$$U_\mu(x) = U_\mu(x+\hat{\nu}L) \quad \text{and} \quad \phi(x) = \phi(x+\hat{\nu}L)\,. \quad (3.11)$$

3.2. Lattice Discretization of Gauge-Invariant Operators

The expression for the 0_0^+ state (Eq. (2.6)) and the 1_1^- state (Eq. (2.7)) must be reformulated using lattice variables. They are given by [27, 28]

$$\mathcal{O}^{0_0^+}(x) = \phi^\dagger(x)\phi(x) = \frac{1}{2}\,\mathrm{Tr}\Big\{\chi^\dagger(x)\chi(x)\Big\}\,, \tag{3.12}$$

$$\mathcal{O}_\mu^{1_1^-\,a}(x) = \mathrm{Tr}\left\{\tau^a \frac{\chi^\dagger(x)}{\sqrt{\det\chi^\dagger(x)}} U_\mu(x) \frac{\chi(x+e_\mu)}{\sqrt{\det\chi^\dagger(x+e_\mu)}}\right\}. \tag{3.13}$$

For the calculation of quasi-PDFs, the interpolators for the different states are needed in momentum space. To obtain operators with definite spatial momentum $\mathbf{p}$, we use the Fourier transformation [24]

$$\mathcal{O}(t,\mathbf{p}) = \frac{1}{\sqrt{|\Lambda_3|}} \sum_{\mathbf{x}\in\Lambda_3} e^{i\mathbf{p}\cdot\mathbf{x}}\mathcal{O}(t,\mathbf{x})\,, \tag{3.14}$$

where the momenta $\mathbf{p}$ have discretized components $p_i = 2\pi k_i/L$ with $k_i = -L/2 + 1, ..., L/2$.

Chapter 4.

Extraction of Quasi-PDFs

Parton distribution functions are inherently non-perturbative objects and thus a calculation on the lattice would, in principle, be the method of choice. However, the definition of a PDF includes light-cone correlations, which are not accessible on a Euclidean lattice. In 2015, Ji proposed to calculate a different distribution termed quasi-PDF, which is based on spatially separated correlations [29]. A review of this approach is given in [30].

In the following, we introduce the different quasi-PDFs that are used in this work and provide the necessary background. Throughout the rest of this work, we present only the lattice version of the operators entering the calculation of the quasi-PDFs.

4.1. Definition of Quasi-PDFs

Parton distribution functions are defined from correlations along the light cone, hence also the name light-cone distributions. This is a defining structural feature and therefore also present in the previously introduced unpolarized quark PDF, see Eq. (2.13). Although fermionic PDFs are not considered in this work, this expression still captures the essential ingredient of a PDF definition, the bilocal light-cone operator connected by a Wilson line to ensure gauge invariance. Lattice Field theory necessitates going to a Euclidean formulation, in which no light-like separation exists. As a consequence, the two fields cannot be separated along the light-cone direction, thus preventing a direct calculation.

The quasi-PDF framework circumvents this issue by employing a distribution through spatial correlations. Concretely, quasi-PDFs are defined from spatially separated, equal-time, bilocal operators connected by a Wilson line along the boost direction. The basic underlying idea from the formalism is then that both distributions share the same long-distance (infrared) behavior for large boost momentum P_3. To be more explicit, the infrared structure of the spatial correlations approaches that of the corresponding light-cone correlations. The short-distance (ultraviolet) behavior, on the other hand, can be treated perturbatively and subtracted from the quasi distribution to obtain the PDF.

This leads to the central principle in constructing quasi-PDFs: they must be defined such that they approach the light-cone distribution in the limit of an infinite momentum boost. Furthermore, this means in lattice calculations one should work at the highest feasible momenta. One additional remark is worth noting here, in the quasi-PDF framework – especially for finite boost momenta – the partonic picture no longer holds. This means that the partons can carry more momentum than the composite state ($x > 1$) or move in the opposite direction ($x < 0$).

Since quasi-PDFs are defined through gauge-invariant operators, they are labeled by global quantum numbers such as J^P. Consequently, for the electroweak theory it is not possible to directly define, for example, a Z-PDF [31]. This is in contrast to QCD, where PDFs for individual quark species can be defined since there exists a one-to-one mapping between flavor quantum numbers and quark species. For the SU(2) gauge–scalar theory, we probe two channels with quantum numbers $J^P = 0^+$ (Higgs-like) and $J^P = 1^-$ (W/Z-like).

Having established these general considerations, we can now write down the general form of the quasi-PDFs evaluated in this work. It is given by

$$\begin{aligned}\tilde{q}_i^j(x, P_3) &= \mathcal{N}(xP_3) \int_{-\infty}^{\infty} \frac{\mathrm{d}z}{2\pi} e^{-izxP_3} \langle i, p | F_j(z) | i, p \rangle \\ &= \mathcal{N}(xP_3) \int_{-\infty}^{\infty} \frac{\mathrm{d}z}{2\pi} e^{-izxP_3} M_i^j(P_3, z)\end{aligned} \tag{4.1}$$

where $|i, p\rangle$ denotes one of the two gauge-invariant states introduced in Eqs. (3.12) and (3.13), with four-momentum $(P_0, 0, 0, P_3)$. For clarity, we recall that the first state represents the physical Higgs and the second one the physical vector boson. The probe current $F_j(z)$ denotes the type of the PDF and corresponds either to a Higgs-like PDF (F_{0^+}) or a W/Z-like PDF (F_{1^-}). These are non-local operators with spatial separation z along the boost direction P_3. $\mathcal{N}(xP_3)$ denotes an operator-dependent kinematic factor, which arises from the specific structure of the probe current and differs between the Higgs-like and W/Z-like quasi-PDFs. Taken together, we have a composite state labeled by i and a probe current labeled by j, where the latter specifies the quantum-number combination being probed. Each such combination corresponds to a distinct quasi-PDF and an associated parton distribution function. However, several distinct quasi-PDF constructions may match onto the same PDF.

4.2. Matrix Elements

The integral in Eq. (4.1) can be carried out straightforwardly, which leaves the task of calculating the physical matrix elements $M_i^j(P_3, z)$. These can be obtained by evaluating ratios of three-point to two-point correlators, which implements the standard truncation, thus [30]

$$R(t_s, \tau; P_3, z) = \frac{C^{3\mathrm{pt}}(P_3, z; \tau, t_s)}{C^{2\mathrm{pt}}(P_3; \tau, t_s)} \overset{0 \ll \tau \ll t_s}{=} \mathcal{K}(P_3)\, M(P_3, z)\,, \tag{4.2}$$

where $\mathcal{K}(P_3)$ is the respective kinematic factor. Two Euclidean time slices, t_s and τ, are introduced in this intermediate step: τ is the insertion time of the probe current, while t_s denotes the sink–source separation. The definitions of these quantities and the construction of the required correlators are given below.

In the following, the expressions for the extracted matrix elements are simplified by omitting several overall prefactors. In particular, we set the kinematic factor $\mathcal{K}(P_3) = 1$, which for bosonic fields would otherwise be given by $\mathcal{K}(P_3) = \frac{1}{2E_i}$, as this does not affect the z-dependence or qualitative behavior of the matrix elements. Additional global prefactors – such as those appearing in the definition of the field-strength tensor – are also omitted at this stage. All omitted factors can be reinstated in a complete calculation, and the final normalization can be fixed using the standard sum rules of parton distribution functions.

Although Eq. (4.2) can be used directly by finding the region where the result is independent of the insertion time τ and doing a constant fit, further methods are also discussed in the literature. Besides the direct approach, two additional methods can be used to extract the matrix element from ratios of three- and two-point functions: the summation method and multi-state fits, of which we employ the former in this work [30]. In this approach, different sink–source separations are combined by summing over the insertion time τ. In principle, this leads to a better suppression of excited-state contamination, albeit at the cost of increased statistical noise. The relevant relation reads

$$\begin{aligned} \mathcal{R}(t_s, P_3, z) &= \sum_{\tau=1}^{t_s-1} \frac{C^{3\mathrm{pt}}(\tau, t_s; P_3, z)}{C^{2\mathrm{pt}}(t_s; P_3)} = \sum_{\tau=1}^{t_s-1} \frac{\left\langle \mathcal{O}_i(\mathbf{p}, t_s) F_j(\tau, z) \mathcal{O}_i^\dagger(\mathbf{p}, 0) \right\rangle}{\left\langle \mathcal{O}_i(\mathbf{p}, t_s) \mathcal{O}_i^\dagger(\mathbf{p}, 0) \right\rangle} \\ &= C + M_i^j(P_3, z) t_s + \mathcal{O}\left(e^{-(E_1 - E_0)t_s}\right)\,, \end{aligned} \tag{4.3}$$

where C is a constant and the sink and source time slices are excluded from the sum to avoid overlap. The matrix element $M(P_3, z)$ can then be obtained by taking the numerical derivative and performing a constant fit.

This means the lattice calculation yields $M_i^j(P_3, z)$ at discrete values of z and P_3 through ratios of the corresponding three- and two-point functions, which then enter the Fourier transform used to calculate the quasi-PDF.

4.3. Higgs-like Quasi-PDF

With the general consideration above in place, we now give an explicit construction of the Higgs-like quasi-PDF $\tilde{h}_i(x, P_3)$. This is done in analogy to the quark quasi-PDF, which serves as the general template [32], and we employ the same normalization $\mathcal{N}(xP_3) = \frac{1}{2}$. It is given by

$$\tilde{h}_i(x, P_3) = \int_{-\infty}^{\infty} \frac{\mathrm{d}z}{4\pi} e^{-izxP_3} \langle i, p|F_{0^+}(z)|i, p\rangle = \int_{-\infty}^{\infty} \frac{\mathrm{d}z}{4\pi} e^{-izxP_3} M_i^H(P_3, z)\,. \tag{4.4}$$

The corresponding discretized version of the integral reads

$$\tilde{h}_i(x, P_3) = \frac{2P_3}{4\pi} \sum_{z=-z_{\max}}^{z_{\max}} e^{-izxP_3} M_i^H(P_3, z)\,. \tag{4.5}$$

Here, $z_{\max}$ needs to be chosen such that the matrix element sufficiently decayed to zero and the additional factor of $2P_3$ follows the normalization used in the literature and is used here for consistency [30].

The probe current itself is given by two spatially separated scalar doublets connected by a straight Wilson line,

$$F_{0^+}(\tau, z) = \phi^\dagger(\hat{z})\Omega(\hat{z}, \hat{0})\phi(\hat{0})\,, \tag{4.6}$$

where the time slice τ is kept implicit through the hat notation, i.e., $\hat{z} = (0, 0, z, \tau)$ and $\hat{0} = (0, 0, 0, \tau)$. The Wilson line provides the gauge connection between the two points $\hat{z}$ & $\hat{0}$ such that the non-local operator is gauge invariant. For a straight path in z-direction $\Omega(\hat{z}, \hat{0})$ is given by

$$\begin{aligned} \Omega(z, 0) &= U_{-z}(z) \cdot \ldots U_{-z}(2) \cdot U_{-z}(1) \\ &= \left(U_z(0) \cdot U_z(1) \cdot \ldots U_z(z-2) U_z(z-1)\right)^\dagger\,, \end{aligned} \tag{4.7}$$

again with the time coordinate kept implicit. The important point to notice is that the Wilson line transforms under a gauge transformation as

$$\Omega(\hat{z}, \hat{0}) \to G(\hat{z})\Omega(\hat{z}, \hat{0})G^\dagger(\hat{0})\,, \tag{4.8}$$

which ensures the gauge invariance of the full probe current.

4.4. W/Z-like Quasi-PDF

Complementing the Higgs-like case, we construct the W/Z-like quasi-PDF $\tilde{w}_i(x, P_3)$ similar to the gluon quasi-PDF in the QCD sector. Here, an additional factor of the parton momentum appears, so $\mathcal{N}(xP_3) = 1/(xP_3)$ [33], and thus the whole expression reads

$$\tilde{w}_i(x, P_3) = \int_{-\infty}^{\infty} \frac{\mathrm{d}z}{2\pi x P_3} e^{-izxP_3} \langle i, p | F_{1^-}(z) | i, p \rangle = \int_{-\infty}^{\infty} \frac{\mathrm{d}z}{2\pi x P_3} e^{-izxP_3} M_i^W(P_3, z) \,. \tag{4.9}$$

In analogy to Eq. (4.5), the discretized form is

$$\tilde{w}_i(x, P_3) = \frac{1}{x\pi} \sum_{z=-z_{\max}}^{z_{\max}} e^{-izxP_3} M_i^W(P_3, z) \,. \tag{4.10}$$

For the actual probe current, several operators have been proposed in the literature, which all approach the same light-cone distribution [34–37]. A priori, it was not evident which one would yield reliable results; we therefore examined the following operators,

$$\begin{aligned} F_{1^-}^{(1)} &\equiv \sum_{\mu \neq z,t} \mathcal{O}(W^{z\mu}, W^{z\mu}; z) && (4.11) \\ &= \mathcal{O}(W^{zx}, W^{zx}; z) + \mathcal{O}(W^{zy}, W^{zy}; z) \,, \\ F_{1^-}^{(2)} &\equiv \sum_{\mu \neq z} \mathcal{O}(W^{z\mu}, W^{z\mu}; z) && (4.12) \\ &= \mathcal{O}(W^{zx}, W^{zx}; z) + \mathcal{O}(W^{zy}, W^{zy}; z) + \mathcal{O}(W^{zt}, W^{zt}; z) \,, \\ F_{1^-}^{(3)} &\equiv \sum_{\mu \neq z,t} \mathcal{O}(W^{t\mu}, W^{t\mu}; z) - \sum_{\mu,\nu \neq z,t} \mathcal{O}(W^{\mu\nu}, W^{\mu\nu}; z) && (4.13) \\ &= \mathcal{O}(W^{tx}, W^{tx}; z) + \mathcal{O}(W^{ty}, W^{ty}; z) - 2\mathcal{O}(W^{xy}, W^{xy}; z) \,. \end{aligned}$$

They are all built from the same underlying object, namely the field-strength tensor evaluated at two spatially separated points connected in a gauge-invariant way. On the lattice this becomes

$$\mathcal{O}(W^{\mu\nu}, W^{\mu\nu}; z) = \mathrm{Tr}\Big\{ W^{\mu\nu}(\hat{z}) \Omega(\hat{z}, \hat{0}) W^{\mu\nu}(\hat{0}) \Omega(\hat{0}, \hat{z}) \Big\} \,. \tag{4.14}$$

Here the hat notation and the Wilson line $\Omega(\hat{z}, \hat{0})$ are the same as defined in the previous section. The quantity $W^{\mu\nu}$ appearing in the operators above is the lattice field-strength tensor, for which we employ the standard definition:

$$W_{\mu\nu} = \frac{i}{8} \Big(\mathcal{P}_{[\mu,\nu]} + \mathcal{P}_{[\nu,-\mu]} + \mathcal{P}_{[-\mu,-\nu]} + \mathcal{P}_{[-\nu,\mu]} \Big) \quad \text{and} \quad \mathcal{P}_{[\mu,\nu]} = U_{\mu\nu} - U_{\nu\mu}$$

where $U_{\mu\nu}$ is the plaquette defined in Eq. (3.6).

During the analysis we observed that the operator $F_{1^-}^{(3)}$ yields matrix elements consistent with zero within statistical uncertainties. To investigate whether this originates from the subtraction, we additionally included the two parts separately,

$$F_{1^-}^{(3\,|\,ti)} \equiv \sum_{\mu \neq z,t} \mathcal{O}(W^{t\mu}, W^{t\mu}; z) \;, \tag{4.15}$$

$$F_{1^-}^{(3\,|\,xy)} \equiv \mathcal{O}(W^{xy}, W^{xy}; z) \;. \tag{4.16}$$

These probe currents have their own matrix element and corresponding quasi-PDF, which we include in the analysis presented in chapter 6.

4.5. Relevant Correlation Functions

As outlined in the previous sections, matrix elements are calculated via ratios of three- & two-point correlation functions. In the following, we provide the explicit construction for those needed in this work. Throughout this section we keep the P_3 dependence implicit with $\mathbf{p} = (0, 0, P_3)$.

We start with the two-point functions required for this analysis, which in the scalar and vector channels take the form

$$C_{\mathrm{H}}^{\mathrm{2pt}}(t_s; P_3) = \left\langle \mathcal{O}^{0_0^+}(\mathbf{p}, t_s) \mathcal{O}^{0_0^+}(\mathbf{p}, 0)^\dagger \right\rangle \tag{4.17}$$

$$C_{\mathrm{W}}^{\mathrm{2pt}}(t_s; P_3) = \left\langle \sum_{\mu=1}^{3} \sum_{a=1}^{3} \mathcal{O}_\mu^{1_1^-\,a}(\mathbf{p}, t_s) \mathcal{O}_\mu^{1_1^-\,a}(\mathbf{p}, 0)^\dagger \right\rangle \tag{4.18}$$

where in the second expression we sum over the custodial index a and over the spatial directions in the index μ.

The general form of the three-point functions is constructed following the approach in [32]. Based on the arguments given above, we should in principle have four different types of (quasi-)PDFs and therefore four corresponding three-point correlators: the Higgs-like PDFs of the spin-0 singlet (the physical Higgs) and of the spin-1 triplet (the physical W/Z bosons) as well as the W/Z-like PDFs of the same states. However, at the correlator level we can further distinguish our PDFs by probing different spin polarizations through different summations over the index μ of the spin-1 operator.

By selecting only the index parallel to the boost direction (and the Wilson line) we project onto the longitudinal spin polarization ($\lambda = 0$). Summing over the transverse indices accesses the transverse polarizations ($\lambda = \pm 1$). In the following, we use the notation $\mu_\perp$ and $\mu_\parallel$ to denote directions perpendicular and parallel to the boost direction, respectively.

This allows us to now list all three-point functions required for this work. The names reflect the corresponding PDFs.

HH: Higgs-like PDF of the spin-0 singlet.

$$C^{\text{3pt}}_{\text{HH}}(\tau, t_s; P_3, z) = \left\langle \mathcal{O}^{0^+_0}(\mathbf{p}, t_s) F_{0^+}(\tau, z) \mathcal{O}^{0^+_0}(\mathbf{p}, 0)^\dagger \right\rangle \tag{4.19}$$

HW: Higgs-like PDF of the spin-1 triplet.

$$C^{\text{3pt}}_{\text{HW}_\perp}(\tau, t_s; P_3, z) = \left\langle \sum_{\mu_\perp} \sum_{a=1}^{3} \mathcal{O}^{1^-_1\, a}_{\mu_\perp}(\mathbf{p}, t_s) F_{0^+}(\tau, z) \mathcal{O}^{1^-_1\, a}_{\mu_\perp}(\mathbf{p}, 0)^\dagger \right\rangle \tag{4.20}$$

$$C^{\text{3pt}}_{\text{HW}_\parallel}(\tau, t_s; P_3, z) = \left\langle \sum_{a=1}^{3} \mathcal{O}^{1^-_1\, a}_{\mu_\parallel}(\mathbf{p}, t_s) F_{0^+}(\tau, z) \mathcal{O}^{1^-_1\, a}_{\mu_\parallel}(\mathbf{p}, 0)^\dagger \right\rangle \tag{4.21}$$

WH: W/Z-like PDF of the spin-0 singlet.

$$C^{\text{3pt}}_{\text{WH}^{(i)}}(\tau, t_s; P_3, z) = \left\langle \mathcal{O}^{0^+_0}(\mathbf{p}, t_s) F^{(i)}_{1^-}(\tau, z) \mathcal{O}^{0^+_0}(\mathbf{p}, 0)^\dagger \right\rangle \tag{4.22}$$

WW: W/Z-like PDF of the spin-1 triplet.

$$C^{\text{3pt}}_{\text{WW}^{(i)}_\perp}(\tau, t_s; P_3, z) = \left\langle \sum_{\mu_\perp} \sum_{a=1}^{3} \mathcal{O}^{1^-_1\, a}_{\mu_\perp}(\mathbf{p}, t_s) F^{(i)}_{1^-}(\tau, z) \mathcal{O}^{1^-_1\, a}_{\mu_\perp}(\mathbf{p}, 0)^\dagger \right\rangle \tag{4.23}$$

$$C^{\text{3pt}}_{\text{WW}^{(i)}_\parallel}(\tau, t_s; P_3, z) = \left\langle \sum_{a=1}^{3} \mathcal{O}^{1^-_1\, a}_{\mu_\parallel}(\mathbf{p}, t_s) F^{(i)}_{1^-}(\tau, z) \mathcal{O}^{1^-_1\, a}_{\mu_\parallel}(\mathbf{p}, 0)^\dagger \right\rangle \tag{4.24}$$

Taking into account the five different versions of the probe current for the W/Z-like PDFs, this gives a total of 18 different combinations. In Table A.3 we provide an overview of the different combinations of correlation functions used in this work and provide the naming scheme for the matrix elements as well as the quasi-PDF.

4.6. Matching Quasi-PDFs to PDFs

Although the matching of the quasi-PDFs to the light-cone distributions is outside the scope of this work, we provide a simple argument for a first qualitative estimate of the corresponding PDFs. Following [30], the matching condition is given by

$$\tilde{q}(x, \mu^2, P_3) = \int_{-1}^{1} \frac{\mathrm{d}y}{|y|} C\left(\xi = \frac{x}{y}, \frac{\mu}{P_3}\right) q(y, \mu^2) + \mathcal{O}(v^2/P_3^2)\,, \tag{4.25}$$

where μ is the renormalization scale of the quasi-PDF $\tilde{q}(x, \mu^2, P_3)$, $C(\xi, \frac{\mu}{P_3})$ denotes the matching coefficient and v the Higgs VEV, which gives the mass scale. At tree level, the matching kernel reduces to a Dirac delta, $\delta(1-\xi)$, and the quasi-PDF and PDF formally coincide. However, this identification strictly holds only in the infinite momentum limit $P_3 \to \infty$. At finite momentum, deviations arise due to power-suppressed corrections of order $\mathcal{O}(v^2/P_3^2)$. Beyond tree level, additional corrections are encoded in the matching kernel.

While, in comparison to QCD, one may expect smaller perturbative corrections entering the matching kernel due to the weaker coupling in the electroweak sector, deviations between quasi- and light-cone PDFs at finite momentum remain controlled by both matching and power corrections.

Chapter 5.

Simulation Setup & Numerical Details

This chapter provides a summary of the numerical setup used in this work. We briefly discuss the simulation algorithm, the processing steps, and the simulation ensembles.

5.1. Algorithm

The configurations are generated using the publicly available HiRep codebase [38]. The simulation strategy, based on heat-bath and overrelaxation updates for the gauge links combined with Metropolis updates of the scalar fields, is identical to that described in Refs. [26, 39, 40], and therefore no description is provided here.

5.2. Processing

In addition to the generation of the lattice configurations described in the previous section, further processing steps are necessary to obtain reliable results for the correlation functions and subsequently the matrix elements and quasi-PDFs. These include the removal of disconnected contributions, the application of smearing, the exploitation of lattice symmetries, and the improvement of the matrix element itself to reduce unphysical oscillations.

Disconnected Contributions. A generic issue that appears in theories involving a scalar field is the presence of disconnected contributions. In the SU(2) gauge–scalar theory, this is particularly relevant for the 0_0^+ two-point function (Eq. (4.17)), due to mixing with the vacuum. To remove these contributions, the vacuum expectation value is subtracted from the operator, via the following transformation

$$\mathcal{O}_i(\mathbf{p}, t) \to \mathcal{O}_i(\mathbf{p}, t) - \langle \mathcal{O}_i(\mathbf{p}, t) \rangle \ . \tag{5.1}$$

These transformed operators are only used for the two-point functions.

Smearing. A standard technique in lattice calculations for suppressing short-distance fluctuations is the use of smearing algorithms [24]. To improve the signal, we employ APE smeared fields for both the sink–source operators as well as the probe currents, following the approach in [40, 41]. In order to keep the time slices of the sink–source operators separated, the smearing is applied only in spatial directions (x, y, z). The smeared fields are defined as

$$U_\mu^{(n)}(x) = \frac{1}{\sqrt{\det R_\mu^{(n)}(x)}} R_\mu^{(n)}(x) \tag{5.2}$$

$$\begin{aligned} R_\mu^{(n)}(x) =& \alpha U_\mu^{(n-1)}(x) + \frac{1-\alpha}{4} \\ & \times \sum_{\substack{\nu\neq\mu \\ \nu\neq t}} \Big(U_\nu^{(n-1)}(x) U_\mu^{(n-1)}(x+\hat\nu) U_\nu^{(n-1)\dagger}(x+\hat\mu) \\ & + U_\nu^{(n-1)\dagger}(x-\hat\nu) U_\mu^{(n-1)}(x-\hat\nu) U_\nu^{(n-1)}(x+\hat\mu-\hat\nu) \Big) \end{aligned} \tag{5.3}$$

$$\begin{aligned} \phi^{(n)}(x) =& \frac{1}{7} \Big(\phi^{(n-1)}(x) \\ & + \sum_{\mu\neq t} \Big(U_\mu^{(n-1)}(x) \phi^{(n-1)}(x+\hat\mu) + U_\mu^{(n-1)\dagger}(x-\hat\mu) \phi^{(n-1)}(x-\hat\mu) \Big) \Big) \,. \end{aligned} \tag{5.4}$$

Here, n denotes the number of smearing steps and α is a real smearing parameter. For the calculation of the probe currents, we used isotropic smearing, meaning we used the averaged fields in all four spacetime directions. This changes the sums in the above expression accordingly to

$$\begin{aligned} R_\mu^{(n)}(x) =& \alpha U_\mu^{(n-1)}(x) + \frac{1-\alpha}{6} \\ & \times \sum_{\nu\neq\mu} \Big(U_\nu^{(n-1)}(x) U_\mu^{(n-1)}(x+\hat\nu) U_\nu^{(n-1)\dagger}(x+\hat\mu) \\ & + U_\nu^{(n-1)\dagger}(x-\hat\nu) U_\mu^{(n-1)}(x-\hat\nu) U_\nu^{(n-1)}(x+\hat\mu-\hat\nu) \Big) \end{aligned} \tag{5.5}$$

$$\begin{aligned} \phi^{(n)}(x) =& \frac{1}{9} \Big(\phi^{(n-1)}(x) \\ & + \sum_{\mu} \Big(U_\mu^{(n-1)}(x) \phi^{(n-1)}(x+\hat\mu) + U_\mu^{(n-1)\dagger}(x-\hat\mu) \phi^{(n-1)}(x-\hat\mu) \Big) \Big) \,. \end{aligned} \tag{5.6}$$

For all results obtained in this work we used $n = 4$ and $\alpha = 0.55$.

Symmetry Averaging. There are various symmetries on the lattice that can be exploited to reduce the statistical noise in the correlation functions. These include translational invariance both in time and spatial directions as well as rotational symmetry. Using temporal translational invariance, both the two- and the three-point functions can be averaged over all time slices. This results in the following expression in the expectation values:

$$\mathcal{O}_i(\mathbf{p},t_s)F_j(\tau)\mathcal{O}_i^\dagger(\mathbf{p},0) \coloneqq \frac{1}{L_T}\sum_{t_0=0}^{L_T-1}\mathcal{O}_i(\mathbf{p},t_s+t_0)F_j(\tau+t_0)\mathcal{O}_i^\dagger(\mathbf{p},t_0) \tag{5.7}$$

$$\mathcal{O}_i(\mathbf{p},t_s)\mathcal{O}_i^\dagger(\mathbf{p},0) \coloneqq \frac{1}{L_T}\sum_{t_0=0}^{L_T-1}\mathcal{O}_i(\mathbf{p},t_s+t_0)\mathcal{O}_i^\dagger(\mathbf{p},t_0) \tag{5.8}$$

Similarly, we can average the probe current over all spatial coordinates, which in the case of F_{0^+} leads to

$$F_{0^+}(\tau,z) = \frac{1}{|\Lambda_3|}\sum_{\mathbf{y}\in\Lambda_3}\phi^\dagger(\hat{y}+z)\Omega(\hat{y}+z,\hat{y})\phi(\hat{y}) \quad \text{with} \quad \hat{y}=(\mathbf{y},\tau)\,. \tag{5.9}$$

Rotational invariance permits an arbitrary choice of the z-direction, i.e., the boost direction and the direction of the Wilson line. This allows one to average over all equivalent permutations of the spatial axes.

Improved matrix element. Quasi-PDFs are defined as the Fourier transform of their corresponding matrix elements. Thus, the distance z at which the matrix element decays to zero plays a crucial role, as insufficiently small values at the boundary lead to unphysical oscillations in the Fourier transform. To mitigate this effect, we use an improved matrix element in which we subtract an estimator of the constant boundary part. This is done by

$$\begin{gathered}\left\langle M_i^j\right\rangle_\partial = \frac{1}{|B|}\sum_{z\in B}M_i^j(z) \quad \text{and} \quad B \coloneqq \{-z_{\max},-z_{\max}+1,z_{\max}-1,z_{\max}\} \\ M_i^j(z)\to M_i^j(z)-\left\langle M_i^j\right\rangle_\partial\,.\end{gathered} \tag{5.10}$$

We expect this procedure to be justified if, for increased lattice sizes, this constant part decreases. This behavior is also present in the QCD case. For a discussion of this issue and other strategies for mitigating it, see [30].

5.3. Ensembles

The lattice simulations in this work are performed for the parameter sets summarized in Table 5.1. The parameters (β,κ,γ) define the gauge coupling, the hopping parameter, and the quartic coupling of the lattice action. The mass of the lightest state, the vector boson, was fixed to $m_{\mathrm{W}}\approx 80.4\,\mathrm{GeV}$. The corresponding values for the Higgs mass m_{H} and the lattice spacing a are taken from the quoted references.

Set 1 and Set 5 are pure SU(2) gauge–scalar ensembles, whereas the third ensemble

Table 5.1.: Simulation parameter sets used in this work.

Name	$\boldsymbol{\beta}$	$\boldsymbol{\kappa}$	$\boldsymbol{\gamma}$	$\boldsymbol{a^{-1}}$ [GeV]	$\boldsymbol{m_{\mathrm{H}}}$ [GeV]
Set 1	2.7894	0.2984	1.317	287	148
Set 5	8.0000	0.1310	0.0033	400	125
Set 5 (with fermions)	8.0000	0.1310	0.0033	400	

Name	$\boldsymbol{N_g}$	$\boldsymbol{m_\psi}$	**Reference**
Set 1	0	–	Jenny et al. [28]
Set 5	0	–	Wurtz et al. [42]
Set 5 (with fermions)	2	0.3103	–

Notes. The values for m_{H} and a^{-1} are taken from the cited references. Both parameter sets correspond to a (physical) W-boson mass of $m_{\mathrm{W}} = 80.375\,\mathrm{GeV}$.

extends Set 5 by including $N_g = 2$ degenerate fermions with a bare mass of m_ψ. This follows the discussion presented in section 2.2.

The statistics used for each lattice volume L^4 are summarized in Table 5.2. The listed values correspond to thermalized and uncorrelated configurations. The statistics decrease with increasing lattice size due to computational cost.

Table 5.2.: Number of configurations used for each parameter set and lattice size.

$\boldsymbol{L}$	**Set 1**	**Set 5**	**Set 5 (with fermions)**
8	972 947	–	–
12	436 890	404 193	–
16	399 404	332 568	37 771
20	207 920	227 103	19 900
24	199 550	216 280	–
28	119 353	139 495	–
32	96 839	–	–

Chapter 6.

Results

In this chapter, we present the numerical results of the lattice calculation. We begin by discussing representative two- and three-point functions to analyze their statistical behavior. We then study the finite-size effects of the matrix elements, followed by their momentum dependence. Finally, we present the resulting quasi-PDFs.

6.1. Representative Two- and Three-Point Correlation Functions

Before discussing the extracted matrix elements we begin by examining representative two- and three-point correlation functions entering any further observables.

Fig. 6.1 shows representative two-point functions for both the spin-0 singlet, Eq. (4.17), and the spin-1 triplet, Eq. (4.18), for different boost momenta on a lattice of size $L = 16$. In the range of source–sink separations employed in this work (see Table A.1), we obtain reasonable signal-to-noise ratio. For large momentum the decay becomes more rapid and the relative errors increase for large t_s. This further limits the accessible range of time separations. Since the two-point functions enter only through ratios with

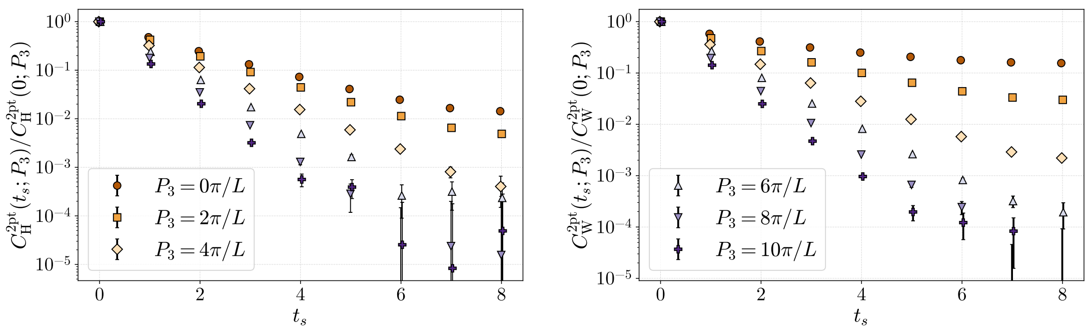

(a) $C_{\mathrm{H}}^{2\mathrm{pt}}$ (b) $C_{\mathrm{W}}^{2\mathrm{pt}}$

Fig. 6.1.: Two-point function for different momenta P_3 for Set 1 on a lattice of size $L = 16$.

three-point functions an explicit fit of the bound-state energy is not required for the ratio construction used in this work.

In Fig. 6.2, representative three-point correlation functions, associated with the Higgs-like quasi-PDF of the spin-0 singlet are shown. As expected, an exponential dependence on the sink–source separation t_s is observed, indicating that the displayed correlation functions correspond to the untruncated Green's function. The cancellation of external propagator contributions occurs after forming the ratios defined in Eq. (4.2). Within a given value for t_s we see no visual dependence on the current insertion time τ.

Furthermore, we do not see a significant imaginary component compared to the real part, so we can disregard it in future discussions. The same plot for the $C^{\text{3pt}}_{\text{WW}^{(2)}_{\parallel}}$ correlation is shown in Fig. B.1.

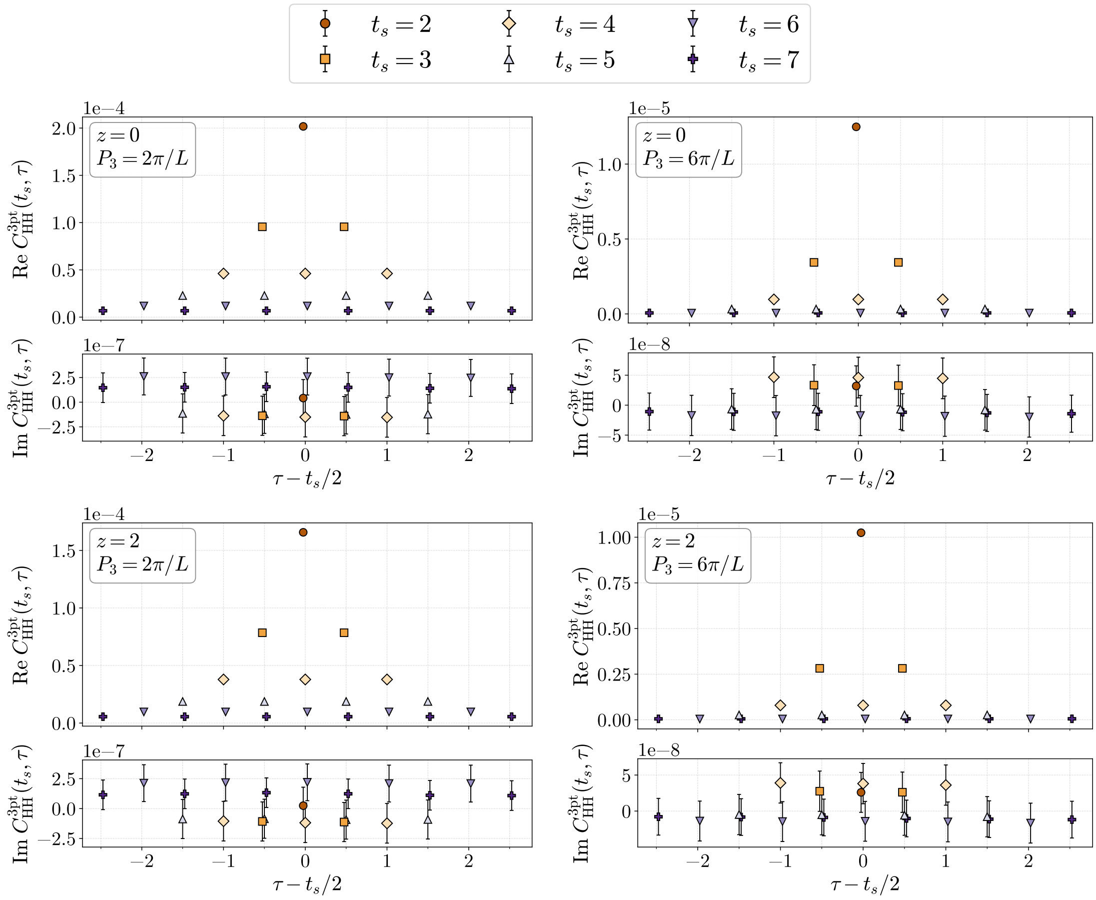

Fig. 6.2.: Representative three-point correlation functions $C^{\text{3pt}}_{\text{HH}}$ for different sink–source separations t_s, plotted as a function of $\tau - t_s/2$. The left column shows results for $P_3 = 2\pi/L$, while the right column corresponds to $P_3 = 6\pi/L$. Data are taken from Set 1 on a lattice of size $L = 16$.

Figs. 6.3 to 6.5 show illustrative plots of the ratios $R^i_j(t_s, \tau; z, P_3)$, defined in Eq. (4.2).

The first figure corresponds to the Higgs-like PDF of the physical Higgs ($R^{\mathrm{H}}_{\mathrm{H}}$) while the latter two correspond to the W/Z-like PDF of the physical vector bosons ($R^{\mathrm{W}^{(2)}}_{\mathrm{W}_{\parallel}}$ & $R^{\mathrm{W}^{(3)}}_{\mathrm{W}_{\perp}}$). [1] The gray band indicates the value for the matrix element obtained through the summation method.

For $R^{\mathrm{H}}_{\mathrm{H}}(t_s, \tau; z, P_3)$ we observe no visible dependence on either t_s or τ. The ratios appear constant within statistical uncertainties for the observed combination of sink–source separations and current insertion times, which indicates no statistically significant excited-state effects. The summation result is consistent with the ratio values across all time separations.

In the case of $R^{\mathrm{W}^{(2)}}_{\mathrm{W}_{\parallel}}(t_s, \tau; z, P_3)$ a mild dependence on t_s is visible, particularly for low momenta, while within a given value of the sink–source separation no significant dependence on τ is observed. This behavior suggests the ratios could, in principle, be used directly to extract the matrix element and for sufficiently large t_s, the extracted values are compatible. Nevertheless, the summation method provides a systematic and robust determination.

The ratio $R^{\mathrm{W}^{(3)}}_{\mathrm{W}_{\perp}}(t_s, \tau; z, P_3)$ varies both in the sink–source separations and current insertion times. A plateau-like region emerges around $\tau = t_s/2$ and the matrix element obtained from the summation method is consistent with the values in this region. In this case, the summation method provides a reliable and controlled extraction.

Overall, the summation method yields consistent results for all investigated cases and enables a controlled extraction, albeit with slightly larger statistical uncertainties, as can be expected from the cumulative nature of the method.

[1] The naming scheme reflects the naming scheme of the corresponding matrix elements (see Table A.3).

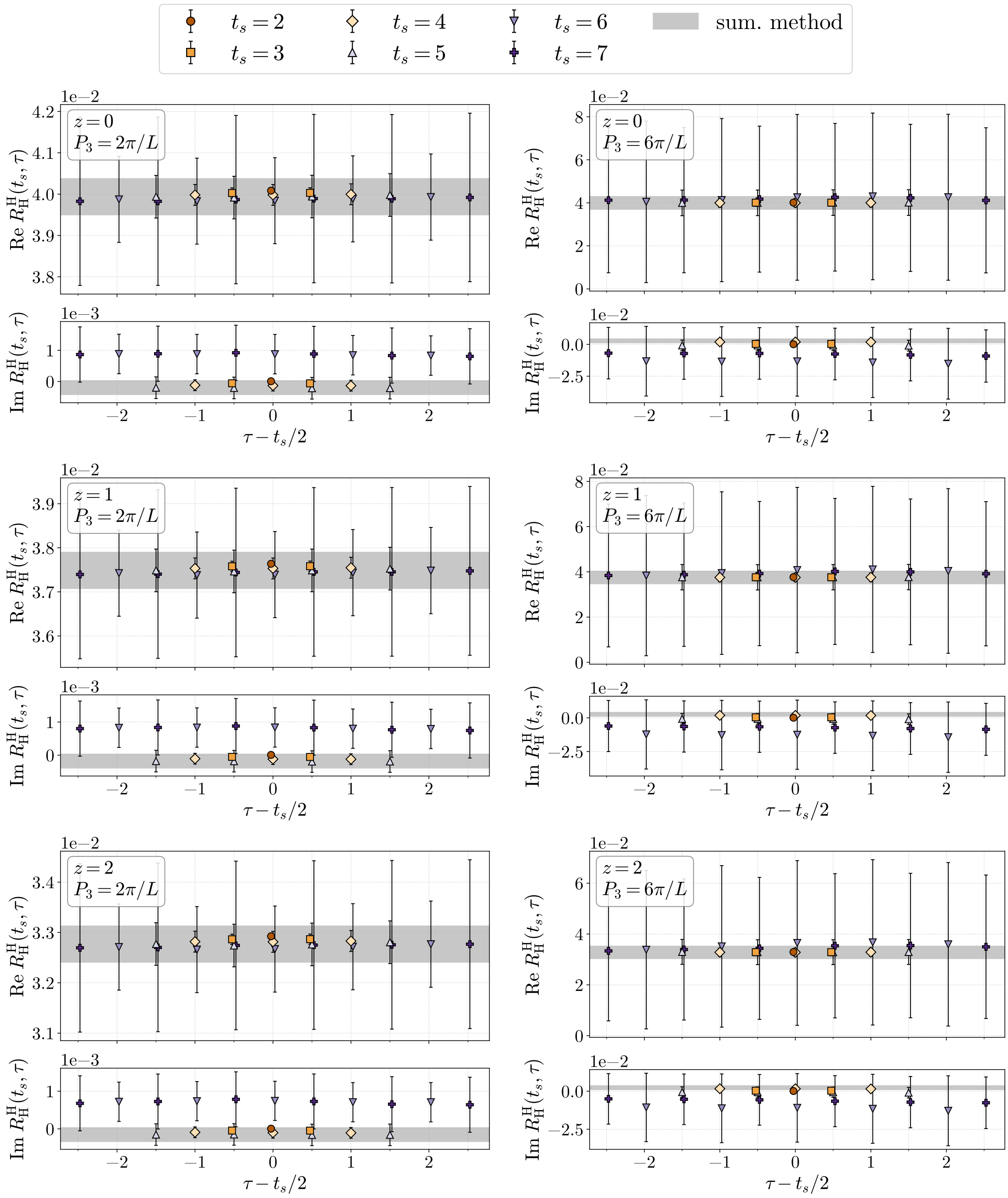

Fig. 6.3.: Representative ratios $R_{\mathrm{H}}^{\mathrm{H}}$ for different sink–source separations t_s, shown as functions of $\tau - t_s/2$. The gray band indicates the matrix element extracted using the summation method. The left (right) column corresponds to momentum $P_3 = 2\pi/L$ ($P_3 = 6\pi/L$). Results are obtained from Set 1 on a lattice of size $L = 16$.

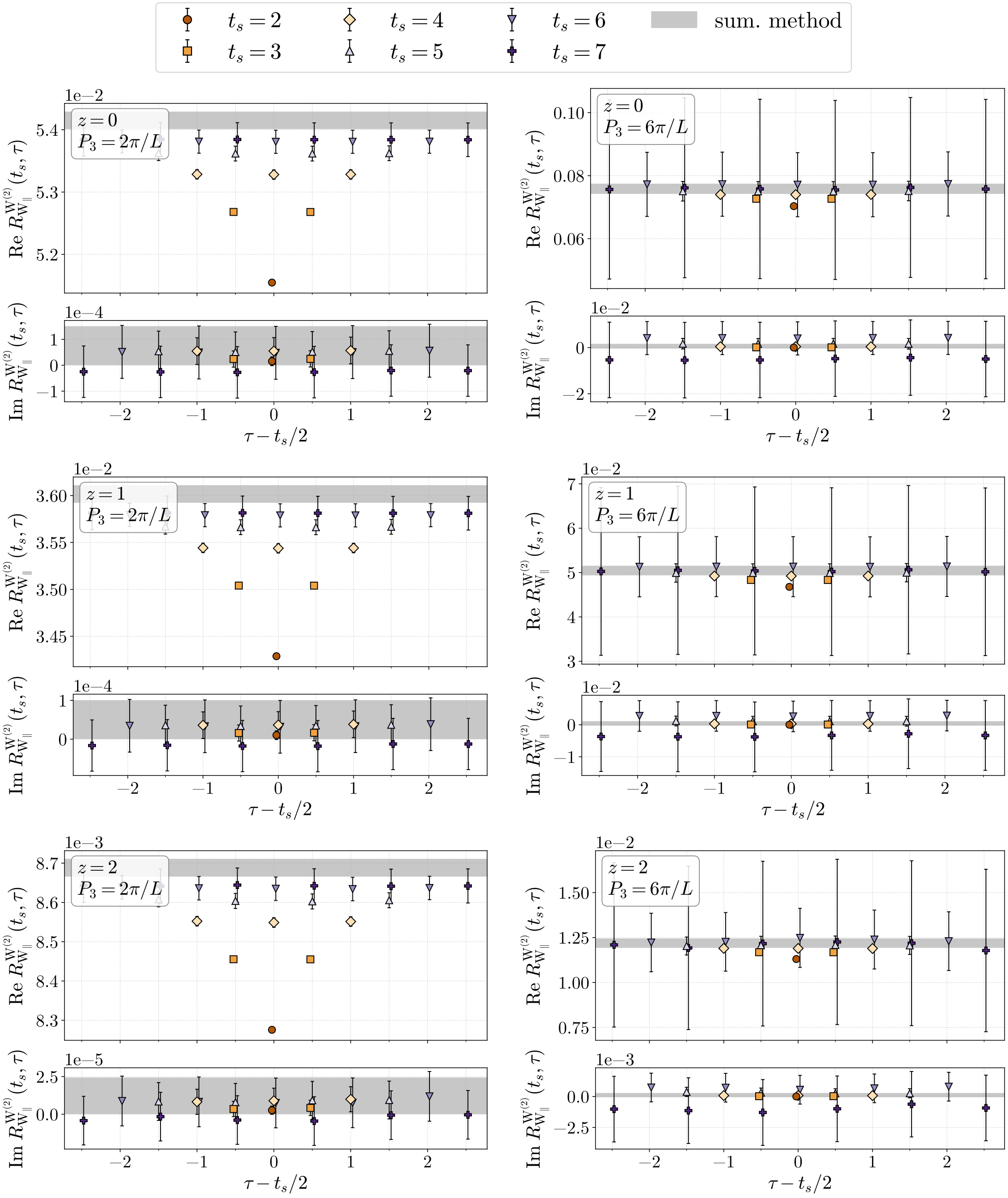

Fig. 6.4.: Representative ratios $R^{\mathrm{W}^{(2)}}_{\mathrm{W}_\parallel}$ for different sink–source separations t_s, shown as functions of $\tau - t_s/2$. The gray band indicates the matrix element extracted using the summation method. The left (right) column corresponds to momentum $P_3 = 2\pi/L$ ($P_3 = 6\pi/L$). Results are obtained from Set 1 on a lattice of size $L = 16$.

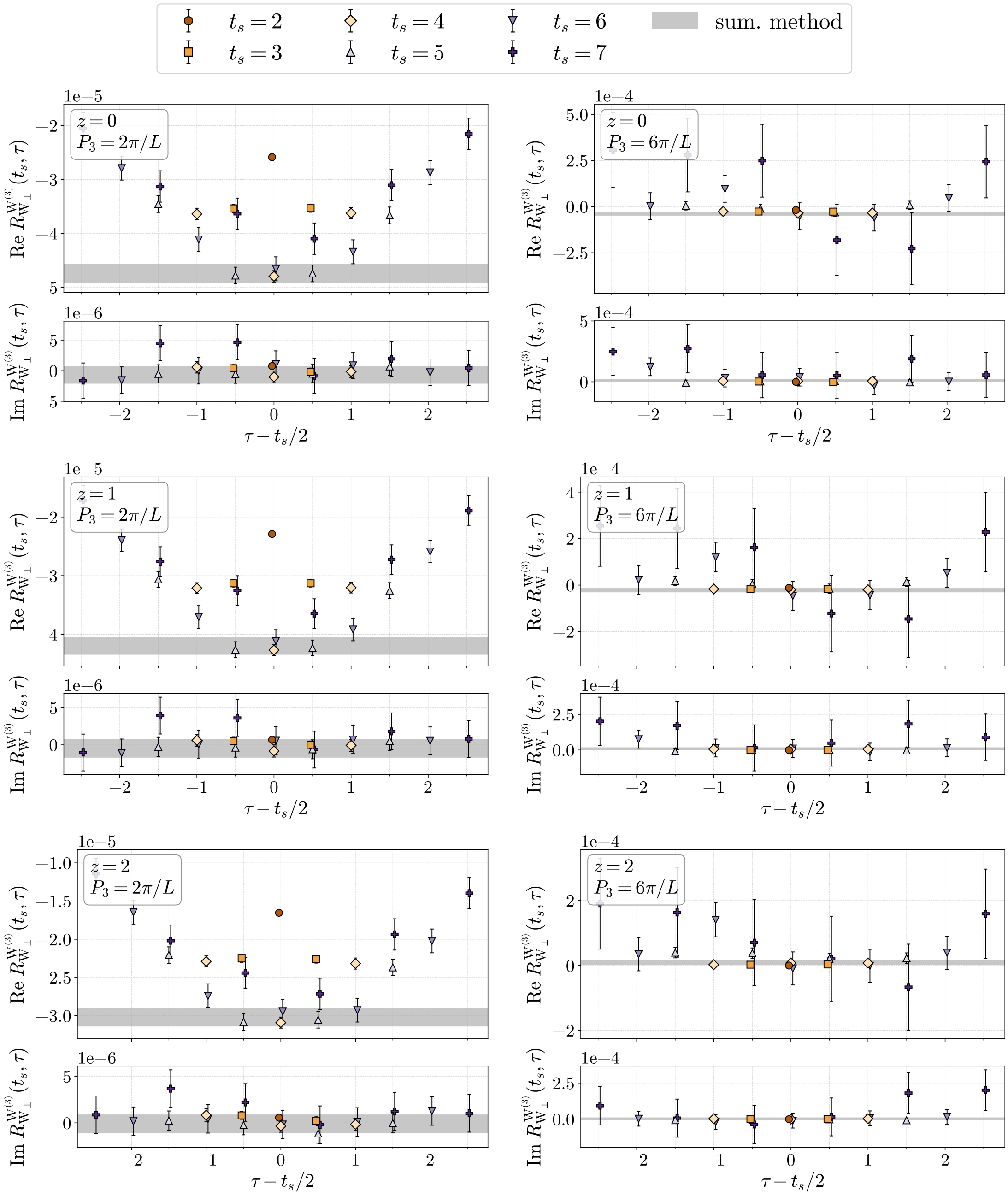

Fig. 6.5.: Representative ratios $R^{\mathrm{W}^{(3)}}_{\mathrm{W}_\perp}$ for different sink–source separations t_s, shown as functions of $\tau - t_s/2$. The gray band indicates the matrix element extracted using the summation method. The left (right) column corresponds to momentum $P_3 = 2\pi/L$ ($P_3 = 6\pi/L$). Results are obtained from Set 1 on a lattice of size $L = 16$.

6.2. Finite-Volume Effects on the Matrix Elements

To investigate finite-size systematics, we compare the observables for different lattice volumes, in the following.

The influence of the lattice size on all 18 different matrix elements for Set 1 is displayed in Figs. 6.6 to 6.8. The obtained matrix element as a function of the Wilson-line length z is shown for four different lattice sizes $L = 8, 16, 24, 32$ and a single fixed momentum $P_3 = \frac{2\pi}{8} \approx 0.79$. The corresponding results for Set 5 are presented in the appendix (see section B.4).

For the matrix elements corresponding to the Higgs-like PDFs (Figs. 6.6a to 6.6c) we observe the largest apparent dependence on the lattice volume. However, this behavior appears not to be a genuine finite-volume effect. It originates largely in the use of the improved matrix element, Eq. (5.10), where we subtract an estimator for the constant part of the matrix element. Since the constant part decreases with increasing lattice size, its subtraction induces an artificial finite-volume effect. Without the subtraction, the values for different lattice sizes mostly coincide within the uncertainties. By comparing the difference between $L = 8$ and $L = 16$ to the difference between $L = 24$ and $L = 32$, we observe a clear reduction. This reduction suggests that the constant component will eventually converge to zero for lattice sizes of sufficient size, thereby providing support for the subtraction procedure. For comparison the unimproved matrix elements M_i^{H} are shown in the appendix, see Fig. B.7.

The remaining observables exhibit a much weaker volume dependence. For the matrix elements built from the $F_{1^-}^{(i)}$ probe currents and the $\mathcal{O}^{0_0^+}$ state (Figs. 6.6d, 6.6e, 6.7a and 6.7b), no significant finite-size effects are visible. The results for the matrix elements $M_{\mathrm{W}_\parallel}^{\mathrm{W}^{(i)}}$ and $M_{\mathrm{W}_\perp}^{\mathrm{W}^{(i)}}$ at $L = 8$ deviate noticeably from the larger volumes. However, for $L \geq 16$, the values largely coincide within uncertainties. This indicates that the finite size effects are already sufficiently suppressed.

As expected, finite-size effects arise when the spatial extent of the Wilson-line becomes close to the lattice size. Such data points are excluded from the analysis through an appropriate choice of $z_{\max}$.

The matrix elements built from the whole $F_{1^-}^{(3)}$ probe current Figs. 6.6f, 6.7e and 6.8d show qualitatively different behavior and are therefore discussed in section 6.5.

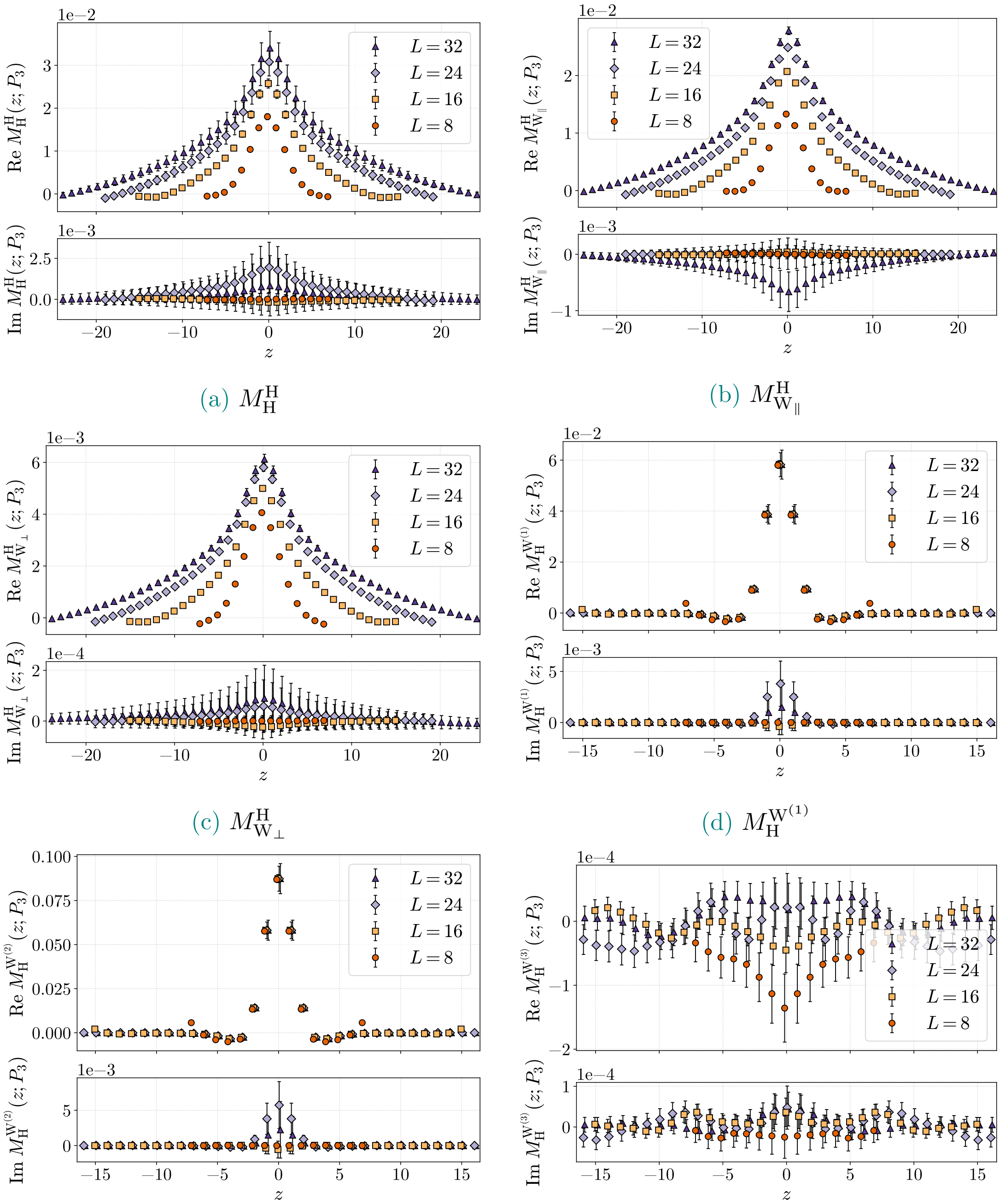

(a) $M_{\mathrm{H}}^{\mathrm{H}}$ (b) $M_{\mathrm{W}_{\parallel}}^{\mathrm{H}}$

(c) $M_{\mathrm{W}_{\perp}}^{\mathrm{H}}$ (d) $M_{\mathrm{H}}^{\mathrm{W}^{(1)}}$

(e) $M_{\mathrm{H}}^{\mathrm{W}^{(2)}}$ (f) $M_{\mathrm{H}}^{\mathrm{W}^{(3)}}$

Fig. 6.6.: Finite-size effects in the real and imaginary parts of the matrix elements $M_i(z, P_3)$ for parameter Set 1 at fixed boost momentum $P_3 = 2\pi/8$ (in lattice units). For each matrix element, results from four lattice volumes $L = 8, 16, 24, 32$ are compared. Panels (a)–(f) show matrix elements 1–6.

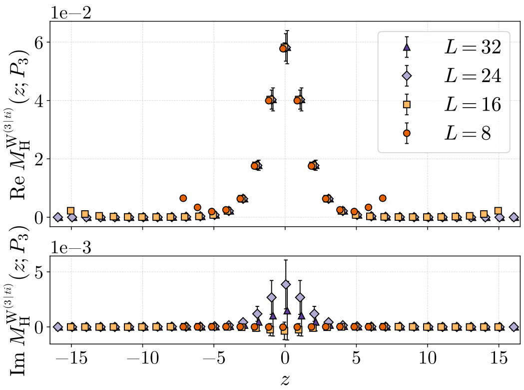

(a) $M_{\mathrm{H}}^{\mathrm{W}^{(3\,|\,ti)}}$

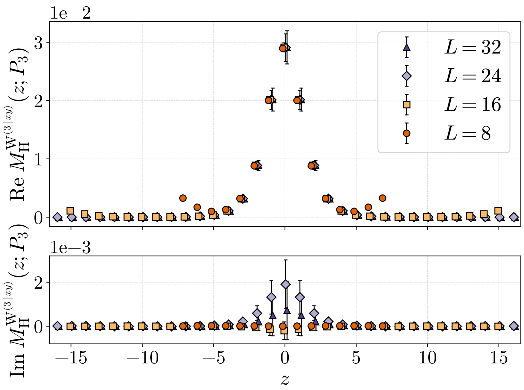

(b) $M_{\mathrm{H}}^{\mathrm{W}^{(3\,|\,sy)}}$

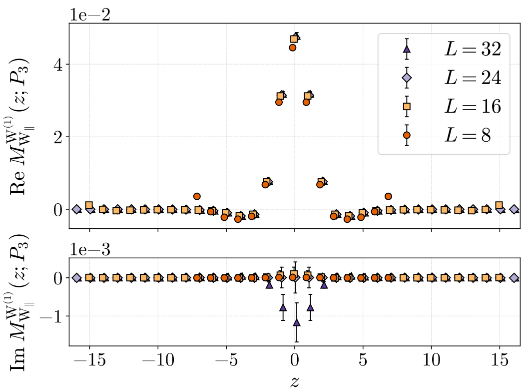

(c) $M_{\mathrm{W}_\parallel}^{\mathrm{W}^{(1)}}$

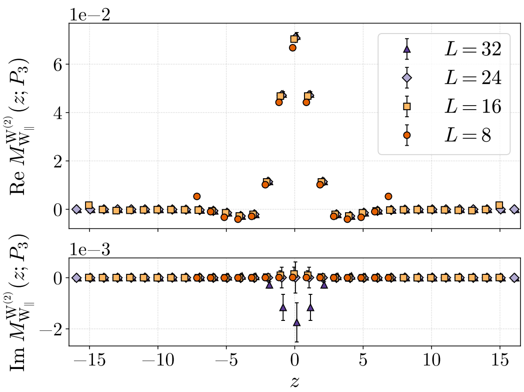

(d) $M_{\mathrm{W}_\parallel}^{\mathrm{W}^{(2)}}$

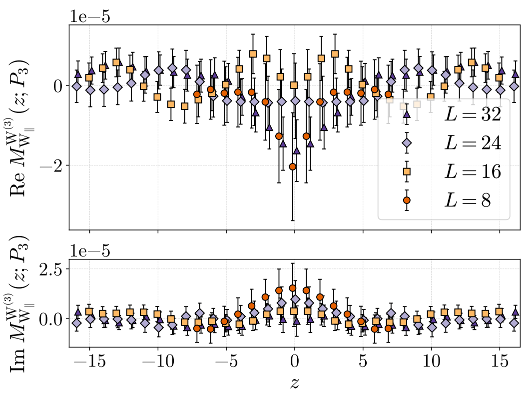

(e) $M_{\mathrm{W}_\parallel}^{\mathrm{W}^{(3)}}$

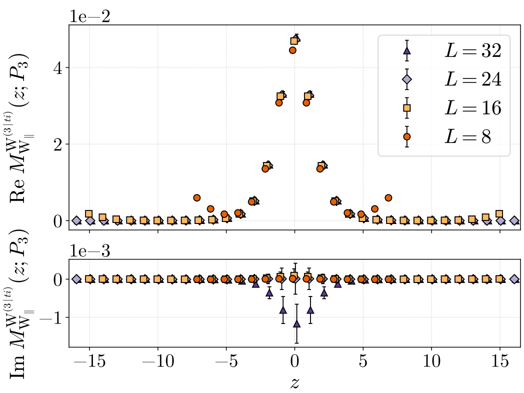

(f) $M_{\mathrm{W}_\parallel}^{\mathrm{W}^{(3\,|\,ti)}}$

Fig. 6.7.: Same as Fig. 6.6, but for matrix elements 7–12.

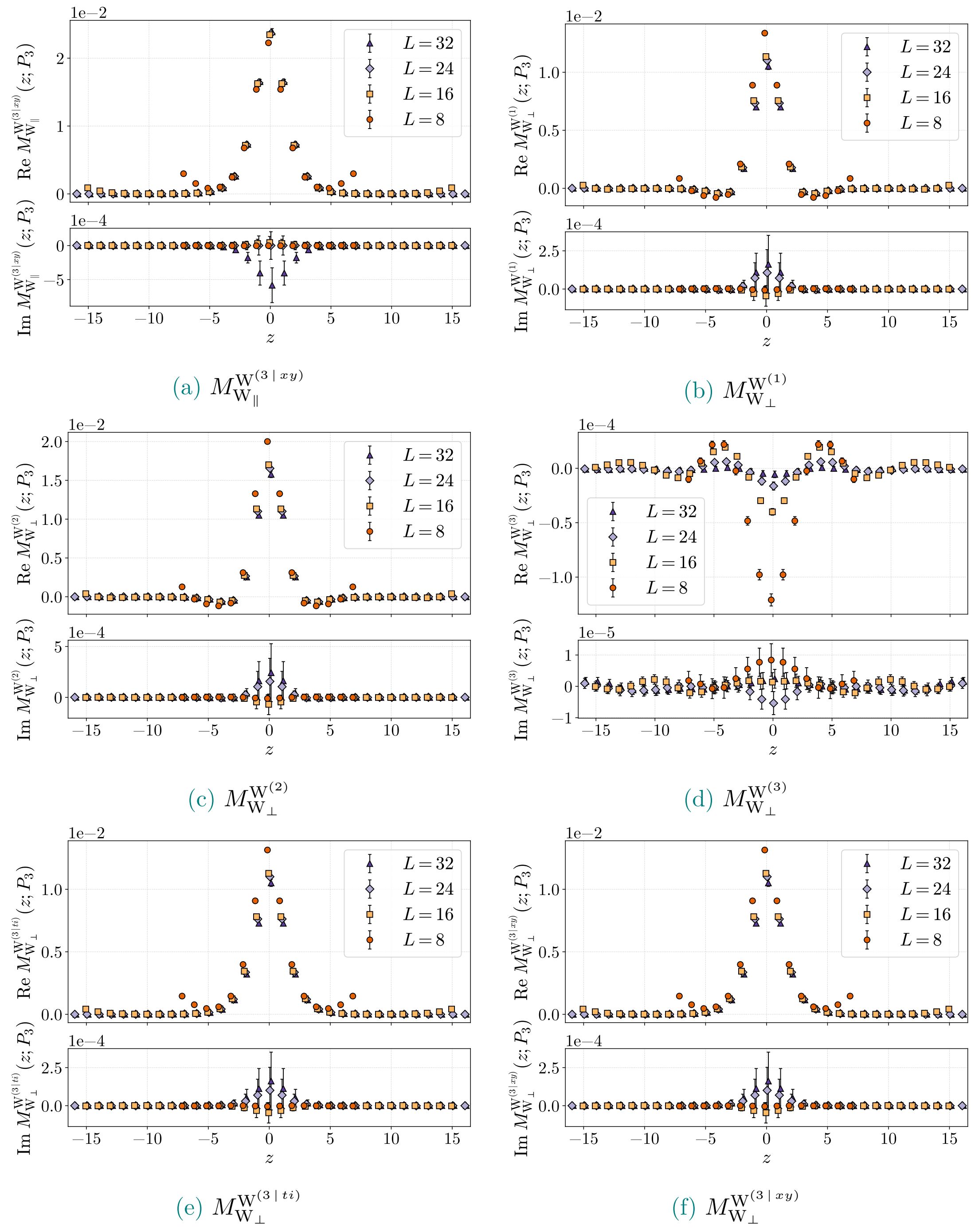

(a) $M^{\mathrm{W}^{(3\,|\,xy)}}_{\mathrm{W}_\parallel}$ (b) $M^{\mathrm{W}^{(1)}}_{\mathrm{W}_\perp}$

(c) $M^{\mathrm{W}^{(2)}}_{\mathrm{W}_\perp}$ (d) $M^{\mathrm{W}^{(3)}}_{\mathrm{W}_\perp}$

(e) $M^{\mathrm{W}^{(3\,|\,ti)}}_{\mathrm{W}_\perp}$ (f) $M^{\mathrm{W}^{(3\,|\,xy)}}_{\mathrm{W}_\perp}$

Fig. 6.8.: Same as Fig. 6.6, but for matrix elements 13–18.

6.3. Momentum Dependence of the Matrix Elements

In this section we investigate the dependence of the matrix elements on the boost momentum P_3. The analysis is based on Set 1, while the corresponding results for Set 5 are provided in section B.5. As discussed in section 4.2, the trivial kinematic prefactor $\mathcal{K}(P_3)$ was set to one, so that only the intrinsic momentum dependence is displayed.

The matrix element corresponding to the Higgs-like PDF of the physical Higgs shows no significant momentum dependence. As shown in Fig. 6.9, the values remain stable across the investigated range of P_3 and for all spatial separations z. As expected, the uncertainties increase for higher momenta, which is due to the decreasing signal-to-noise ratio in the underlying correlation functions.

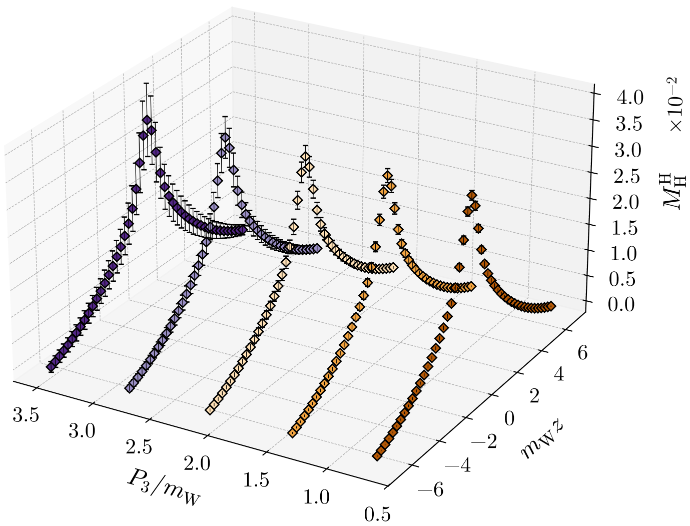

Fig. 6.9.: Momentum dependence of the matrix element $M_{\mathrm{H}}^{\mathrm{H}}(z, P_3)$ for parameter Set 1 on the largest lattice volume $L = 32$. The Wilson-line length z is plotted as $m_W z$ and the boost momentum P_3 as P_3/m_W.

The respective plots for the matrix elements $M_{\mathrm{W}_\parallel}^{\mathrm{H}}$ and $M_{\mathrm{W}_\perp}^{\mathrm{H}}$ (Higgs-like PDFs of the physical vector boson) are shown in Figs. 6.10 and 6.11. For these observables, we see a dependence on the boost momentum primarily in the magnitude, while the overall shape in z remains largely unchanged. In the case of longitudinal spin polarization, the magnitude seems to approach a plateau at higher momenta. In contrast, the matrix element for transverse spin polarization appears to be suppressed at large momenta.

The matrix element corresponding to the W/Z-like PDF of the physical Higgs (probed by the $F_{1^-}^{(2)}$ current) shows behavior similar to $M_{\mathrm{H}}^{\mathrm{H}}$. We see no apparent dependence within the investigated range of P_3 and z, see Fig. 6.12. In comparison, $M_{\mathrm{H}}^{\mathrm{W}^{(2)}}$ exhibits a narrower peak in the z direction.

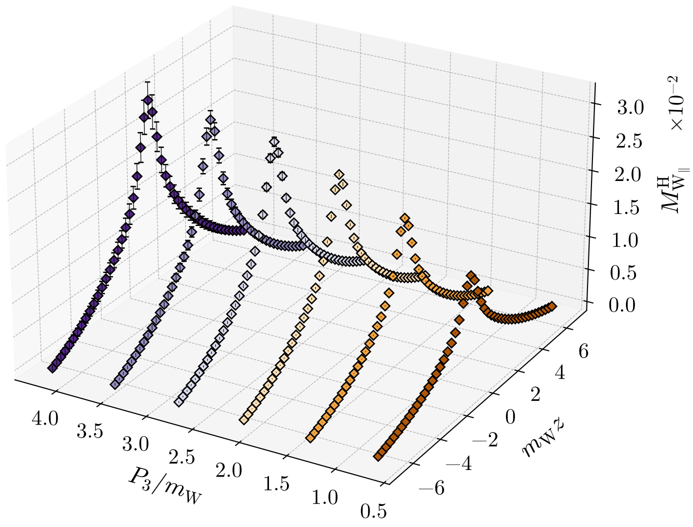

Fig. 6.10.: Momentum dependence of the matrix element $M^{\mathrm{H}}_{\mathrm{W}_\parallel}(z, P_3)$ for parameter Set 1 on the largest lattice volume $L = 32$.

The matrix elements $M^{\mathrm{W}^{(2)}}_{\mathrm{W}_\parallel}$ and $M^{\mathrm{W}^{(2)}}_{\mathrm{W}_\perp}$, which describe the W/Z-like PDF of the vector boson probed by $F^{(2)}_{1^-}$, are shown in Figs. 6.13 and 6.14. As in the case of $M^{\mathrm{H}}_{\mathrm{W}_\parallel}$ and $M^{\mathrm{H}}_{\mathrm{W}_\perp}$, we observe a momentum dependence primarily in the magnitude, with no additional z dependence. A similar suppression at large momenta is visible for the transverse spin polarization, while longitudinal polarization exhibits plateau-like behavior.

Finally, we consider the momentum dependence of the $M^{\mathrm{W}^{(3)}}_{\mathrm{W}_\perp}$ matrix element, see Fig. 6.15. In contrast to the previously discussed matrix elements, we observe a more involved dependence on P_3, reflected in a modification of the z-dependence. However, this is more clearly visible in the results of Set 5 and will therefore be discussed separately in section 6.5.

The behavior of the matrix elements forms the basis of the corresponding quasi-PDFs, which are obtained via the Fourier Transform and analyzed in the next section.

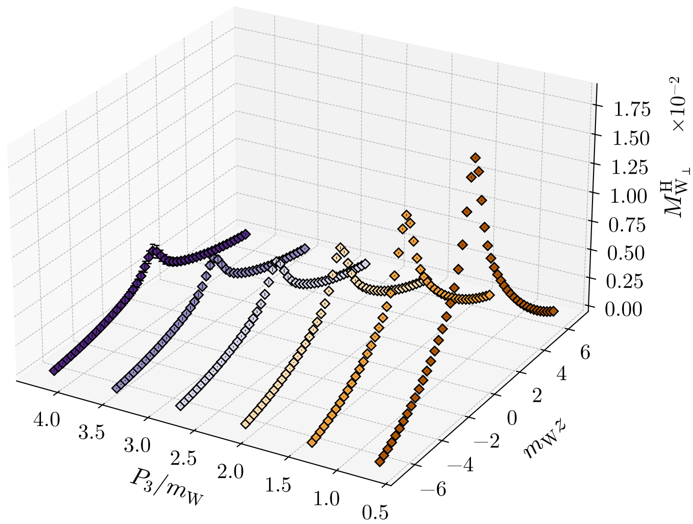

Fig. 6.11.: Momentum dependence of the matrix element $M^{\rm H}_{\rm W_\perp}(z, P_3)$ for parameter Set 1 on the largest lattice volume $L = 32$.

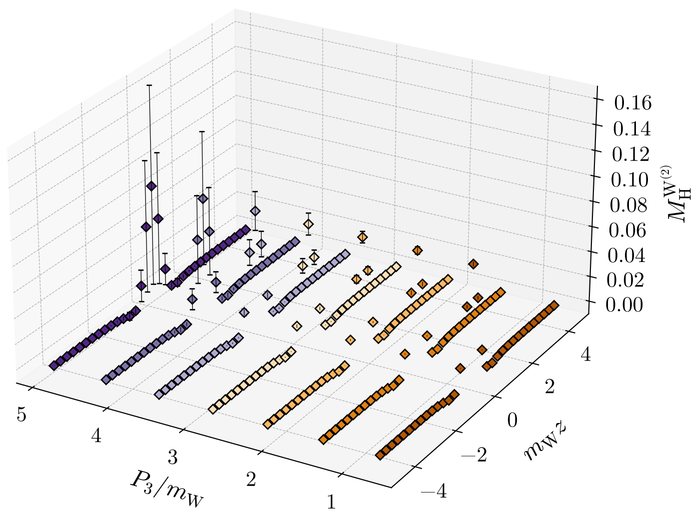

Fig. 6.12.: Momentum dependence of the matrix element $M^{\rm W^{(2)}}_{\rm H}(z, P_3)$ for parameter Set 1 on the largest lattice volume $L = 32$.

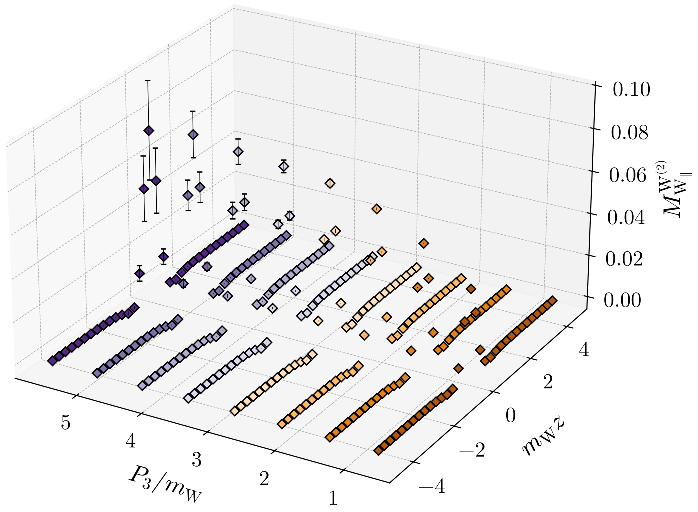

Fig. 6.13.: Momentum dependence of the matrix element $M_{W_\parallel}^{W^{(2)}}(z, P_3)$ for parameter Set 1 on the largest lattice volume $L = 32$.

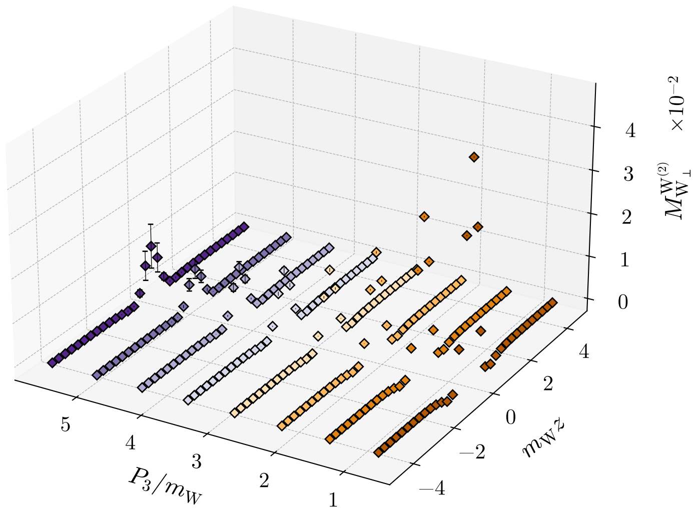

Fig. 6.14.: Momentum dependence of the matrix element $M_{W_\perp}^{W^{(2)}}(z, P_3)$ for parameter Set 1 on the largest lattice volume $L = 32$.

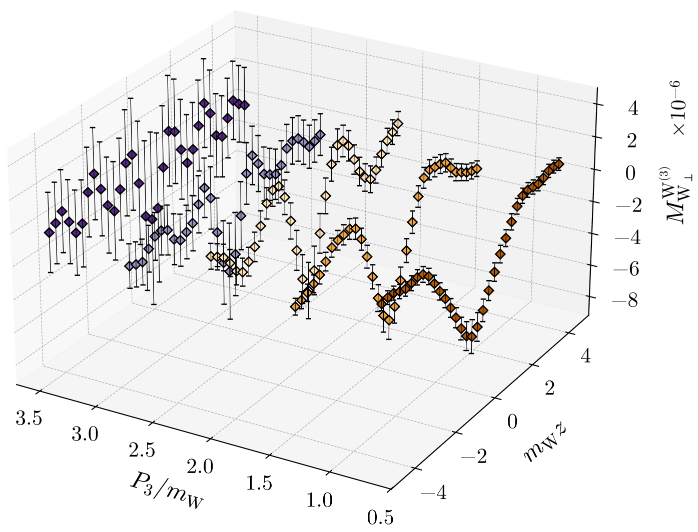

Fig. 6.15.: Momentum dependence of the matrix element $M_{\mathrm{W}_\perp}^{\mathrm{W}^{(3)}}(z, P_3)$ for parameter Set 1 on the largest lattice volume $L = 32$.

6.4. Results for the Quasi-PDFs

After discussing the properties of the matrix elements, we will now turn to the corresponding quasi-PDFs obtained through the Fourier transform in Eq. (4.1). We first study their momentum dependence, then compare the different channels at the largest accessible momenta, and finally investigate the effect of including a fermion term.

6.4.1. Representative Quasi-PDFs

In this section, we investigate the dependence of the obtained quasi-PDFs on the boost momentum P_3. The analysis is based on Set 1, while the corresponding results for Set 5 are provided in section B.6. The quasi-PDFs are plotted as $x\,\tilde{q}(x, P_3)$, including both negative x and values with $|x| > 1$. This representation avoids numerical instabilities associated with a division by x for the W/Z-like quasi-PDFs, but leads to a vanishing value at $x = 0$ for the Higgs-like quasi-PDFs.

As shown in the previous section, the matrix elements exhibit only a mild dependence on the boost momentum P_3. This general trend is largely reflected in the Fourier transform, i.e., in the resulting quasi-PDFs. As stated in Eq. (4.25), the quasi-PDFs differ from the light-cone distributions through perturbative matching and finite-momentum power corrections. The observed mild P_3 dependence suggests moderate finite-momentum effects and therefore, at tree level, the quasi-PDFs may already provide a reasonable approximation to the corresponding PDFs.

The Higgs-like quasi-PDFs of the physical Higgs and the vector state in different polarizations show qualitatively similar behavior, see Figs. 6.16 to 6.18. In all cases, a peak forms at small to intermediate values of x, followed by a steady decline towards larger momentum fractions in $x\,\tilde{h}(x, P_3)$. Although we employed the improved matrix element, strong oscillatory behavior is still observed at large boost momenta. These effects are further amplified in the chosen representation, where multiplication by x enhances the fluctuations at large x and leads to increased relative uncertainties.

The magnitude of the quasi-PDFs appears to remain approximately constant over the investigated range of P_3 for $\tilde{h}_{\mathrm{H}}$, increases slightly for $\tilde{h}_{\mathrm{W}_\parallel}$, and decreases for $\tilde{h}_{\mathrm{W}_\perp}$ at higher momenta.

Within the current statistical precision, the highest reliably controlled boost momentum, for the Higgs-like PDFs corresponds to the fourth or fifth lattice momentum, depending on the composite state, as statistical uncertainties increase significantly at larger momenta. Although results at higher momenta are shown, quantitative statements regarding the Higgs-like PDFs in this regime become challenging.

In contrast, the W/Z-like quasi-PDFs are statistically better behaved, which conse-

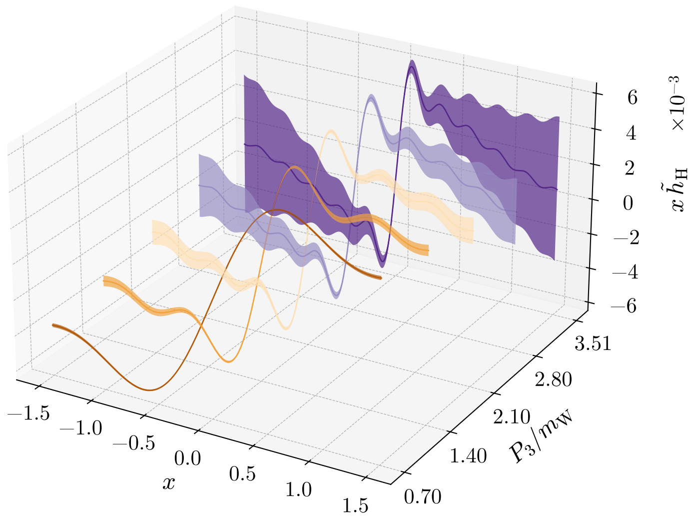

Fig. 6.16.: Quasi-PDF $x\,\tilde{h}_{\mathrm{H}}(x, P_3)$ as a function of x and P_3/m_{W} (Set 1, $L = 32$).

quently allows for higher boost momenta to be accessed. For example, the ninth lattice momentum still exhibits well-controlled uncertainties for $\tilde{w}^{(2)}_{\mathrm{W}_{\parallel}}$ (see Fig. 6.20). The momentum dependence of the other two quasi-PDFs probed by $F^{(2)}_{1^-}$ is displayed in Figs. 6.19 and 6.21.

The distributions again share common characteristics. At low momenta, they show only weak x dependence in the investigated range and behave almost constantly in $x\,\tilde{w}(x, P_3)$, while for higher momenta a pronounced enhancement around $x = 0$ develops, followed by a decay towards large x. Given the mild momentum dependence of the underlying matrix elements, it remains unclear whether this structure is primarily an artifact of the Fourier transformation or a genuine physical feature.

Fig. 6.22 shows the quasi-PDF corresponding to the matrix element in Fig. 6.15 and is included here for completeness.

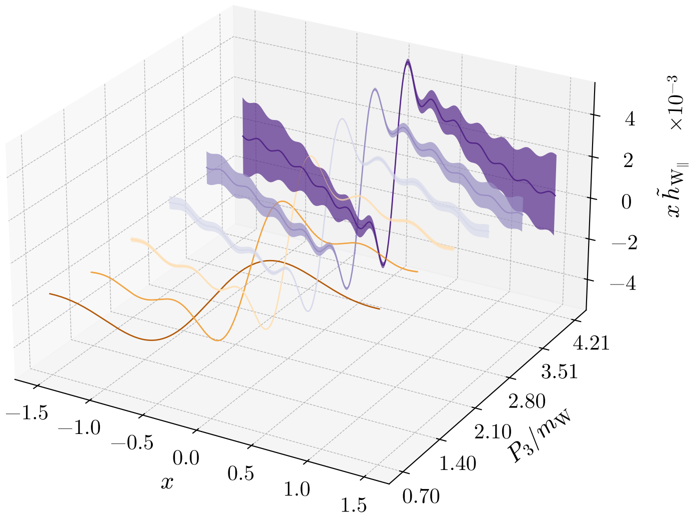

Fig. 6.17.: Quasi-PDF $x\,\tilde{h}_{\mathrm{W}_\parallel}(x, P_3)$ as a function of x and P_3/m_W (Set 1, $L = 32$).

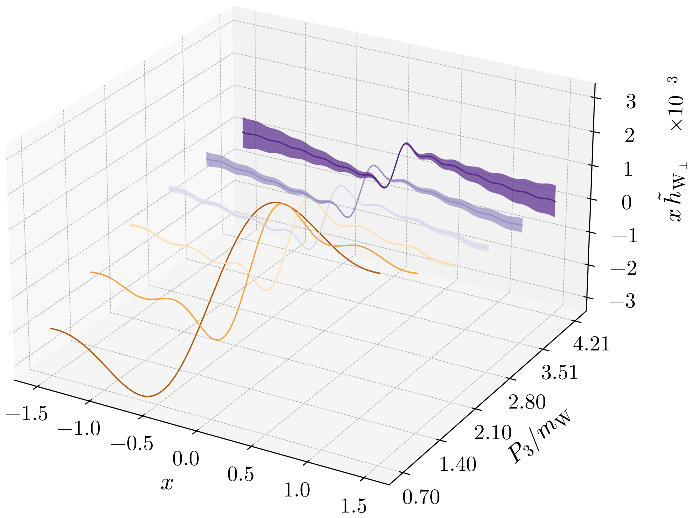

Fig. 6.18.: Quasi-PDF $x\,\tilde{h}_{\mathrm{W}_\perp}(x, P_3)$ as a function of x and P_3/m_W (Set 1, $L = 32$).

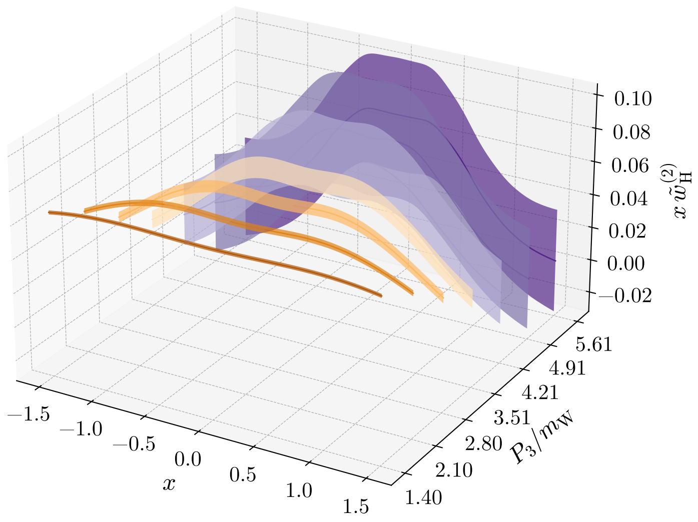

Fig. 6.19.: Quasi-PDF $x\,\tilde{w}_{\mathrm{H}}^{(2)}(x, P_3)$ as a function of x and P_3/m_{W} (Set 1, $L = 32$).

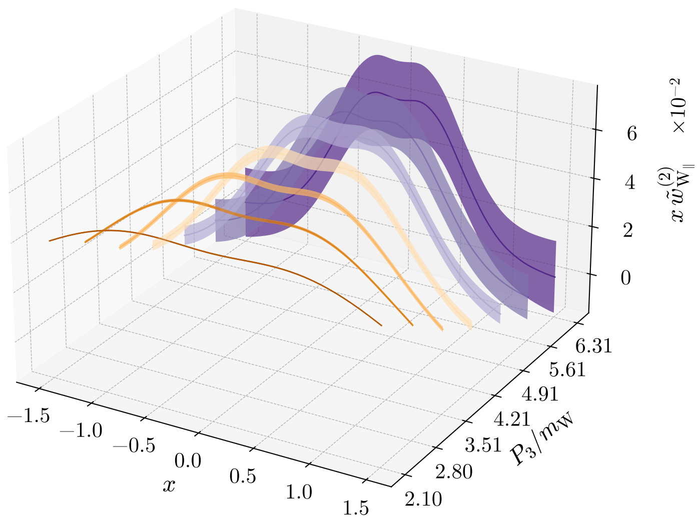

Fig. 6.20.: Quasi-PDF $x\,\tilde{w}_{\mathrm{W}_\parallel}^{(2)}(x, P_3)$ as a function of x and P_3/m_{W} (Set 1, $L = 32$).

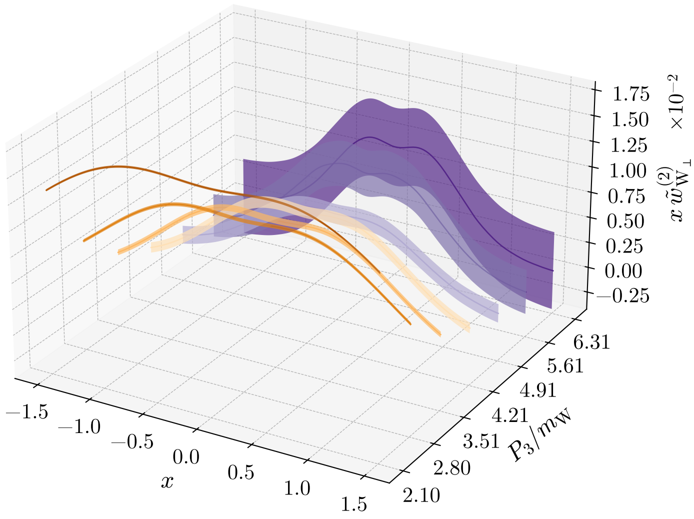

Fig. 6.21.: Quasi-PDF $x\,\tilde{w}^{(2)}_{\mathrm{W}_\perp}(x, P_3)$ as a function of x and P_3/m_{W} (Set 1, $L = 32$).

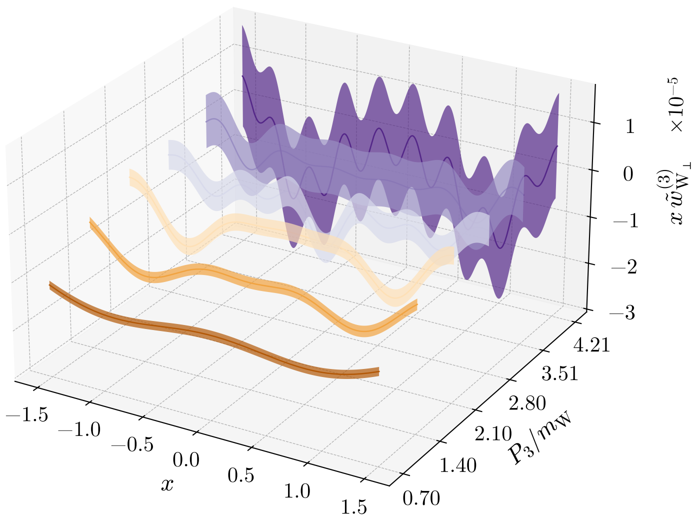

Fig. 6.22.: Quasi-PDF $x\,\tilde{w}^{(3)}_{\mathrm{W}_\perp}(x, P_3)$ as a function of x and P_3/m_{W} (Set 1, $L = 32$).

6.4.2. Comparison at Highest Momentum

Since quasi-PDFs are expected to approach their light-cone counterparts with increasing boost momentum, it is instructive to compare the obtained distributions at the largest accessible momenta. In the following, the quasi-PDFs of the different composite states are shown together at these momenta. Figs. 6.23 to 6.26 display the resulting distributions for the vector boson ($\mathrm{W}_\parallel$ and $\mathrm{W}_\perp$) and the Higgs (H) states for the parameter sets Set 1 and Set 5. All distributions are plotted as $x\,\tilde{q}(x, P_3)$ and, to allow better comparison, are normalized to the quasi-PDF(s) obtained in the $\mathrm{W}_\parallel$ mode at the respective momentum.

In Fig. 6.23, the results for Set 1 at momentum $P_3 = 2.80\,m_\mathrm{W}$ and lattice size $L = 32$ are shown. At this momentum, the signal of the Higgs-like quasi-PDFs is still well controlled in the chosen representation, which is no longer the case for higher momenta. Overall, the quasi-PDFs exhibit qualitatively similar behavior, with no pronounced differences in their overall shape across the different composite states and spin polarizations. The W/Z-like quasi-PDFs remain mostly flat in the investigated range of momentum fraction x in $x\,\tilde{w}(x, P_3)$, whereas the Higgs-like channels show a peak at intermediate x with an oscillatory structure and gradual decline towards large x, consistently across all considered states. This behavior has been discussed in the previous section.

A comparison of the quasi-PDFs probed by $F^{(1)}_{1^-}$ and $F^{(2)}_{1^-}$ shows that they exhibit nearly identical overall shapes, differing primarily in their magnitude. This is consistent with the operator definitions, as the sole distinction between the two currents is the additional term $\mathcal{O}(W^{zt}, W^{zt}; z)$, which appears to contribute comparably to the spatial components $\mathcal{O}(W^{zi}, W^{zi}; z)$.

A second observation is that the $\mathrm{W}_\perp$ channel is noticeably suppressed compared to the $\mathrm{W}_\parallel$ channel for all quasi-PDFs presented in this comparison. This suppression is observed consistently across the investigated momentum range, indicating that this is a pronounced polarization dependence. At higher momentum, this behavior becomes even more noticeable, which can be seen in Fig. 6.24. This plot shows the quasi-PDFs for a boost momentum of $P_3 = 5.61\,m_\mathrm{W}$ again for Set 1 and $L = 32$. The Higgs-like distributions are excluded due to insufficient statistical precision.

Apart from the more pronounced suppression and the now rapid fall-off in the intermediate x region, the qualitative characteristics remain largely unchanged compared to the lower-momentum quasi-PDFs. In particular, we again see the same overall shapes across $\mathrm{W}_\parallel$, $\mathrm{W}_\perp$ and H and furthermore the quasi-PDFs obtained from $F^{(1)}_{1^-}$ and $F^{(2)}_{1^-}$ appear to differ once more only in magnitude.

In Figs. 6.25 and 6.26, the same comparison is shown for Set 5 for a lattice size of $L = 28$ and boost momenta $P_3 = 3.35\,m_\mathrm{W}$ and $P_3 = 8.93\,m_\mathrm{W}$, respectively. The parameters of Set 5 correspond to a smaller lattice spacing compared to Set 1 (see Table 5.1), which allows for investigating larger momenta. Qualitatively, the results of the two sets are consistent with one another and we see largely comparable quasi-PDFs across the

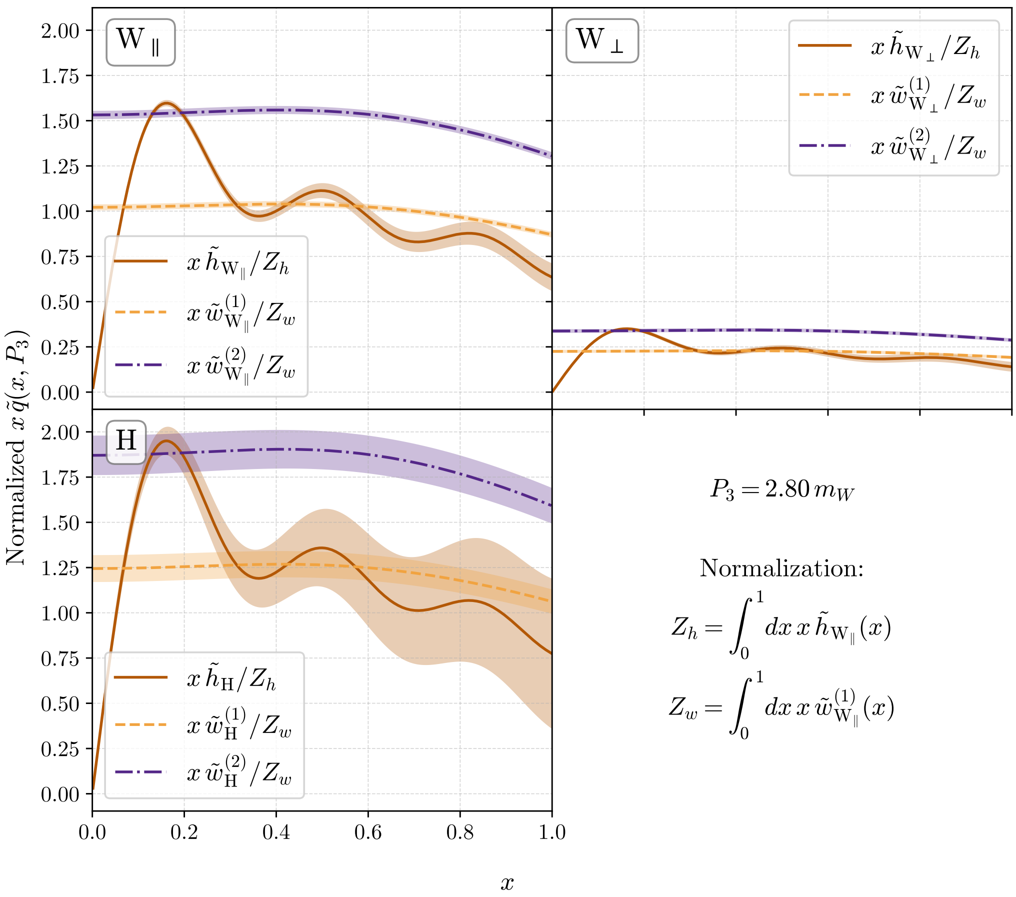

Fig. 6.23.: Obtained quasi-PDFs plotted as $x\tilde{q}(x, P_3)$ for Set 1 at the largest volume $L = 32$ and the largest feasible value of the boost momentum $P_3 = 2.80\,m_\mathrm{W} \approx 225\,\mathrm{GeV}$ (where the Higgs-like quasi-PDFs still exhibit well-controlled uncertainties). The subplots correspond to the different composite states $\mathrm{W}_\parallel$, $\mathrm{W}_\perp$, and H. The quasi-PDFs are normalized to the quasi-PDFs in the $\mathrm{W}_\parallel$ mode.

different channels.

In Fig. 6.26 a small enhancement for $x \approx 0.3$ is visible both in the $\mathrm{W}_\parallel$ and H channel after which we see a rapid decline towards large x. At this momentum the quasi-PDFs in $\mathrm{W}_\perp$ are nearly an order of magnitude below the corresponding distributions in the longitudinal spin polarization.

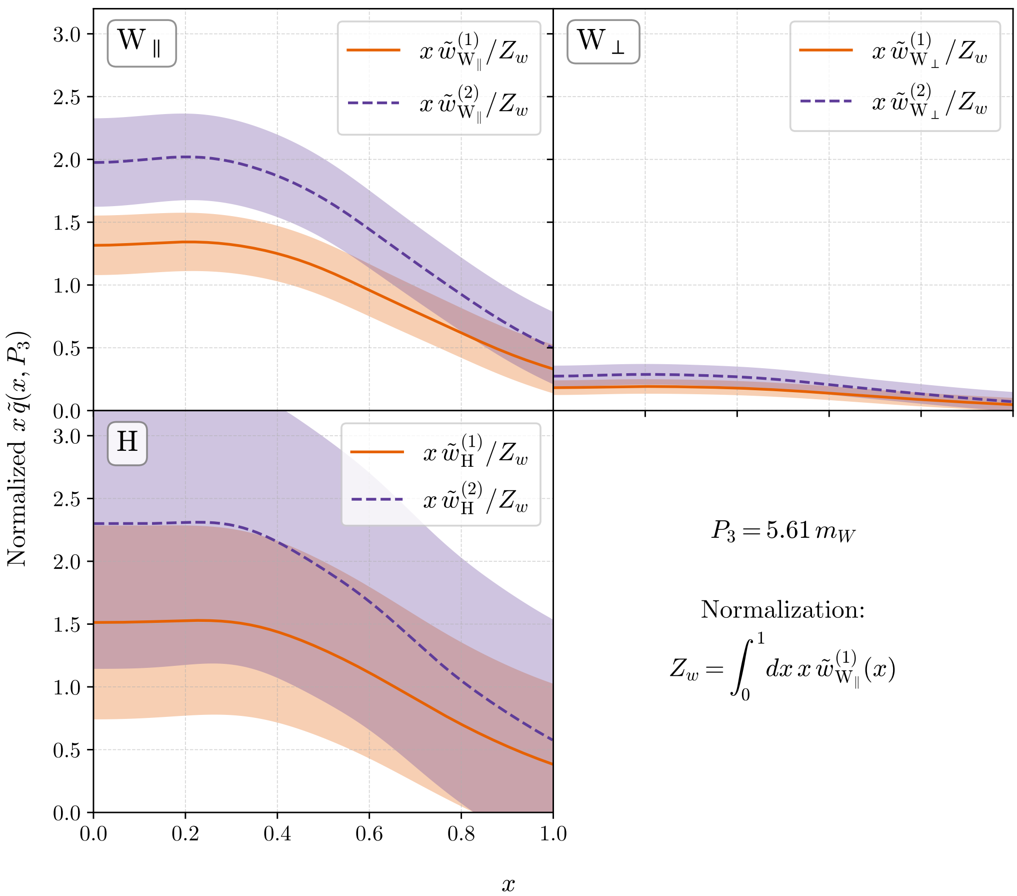

Fig. 6.24.: Same as Fig. 6.23, but for a larger boost momentum $P_3 = 5.61\, m_{\mathrm{W}} \approx 451\,\mathrm{GeV}$, with the Higgs-like quasi-PDFs excluded due to insufficient statistical precision.

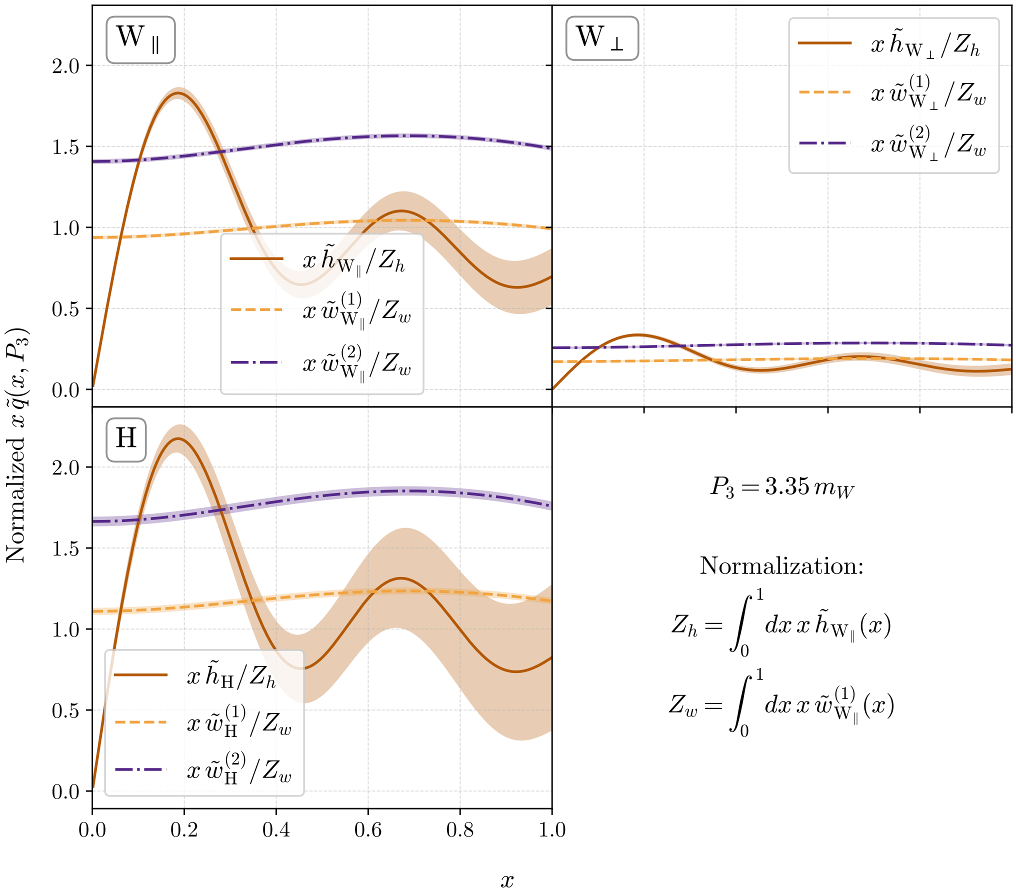

Fig. 6.25.: Obtained quasi-PDFs plotted as $x\tilde{q}(x, P_3)$ for Set 5 at the largest volume $L = 28$ and the largest feasible value of the boost momentum $P_3 = 3.35\,m_{\mathrm{W}} \approx 270\,\mathrm{GeV}$ (where the Higgs-like quasi-PDFs still exhibit well-controlled uncertainties). The subplots correspond to the different composite states $\mathrm{W}_\parallel$, $\mathrm{W}_\perp$, and H. The quasi-PDFs are normalized to the quasi-PDFs in the $\mathrm{W}_\parallel$ mode.

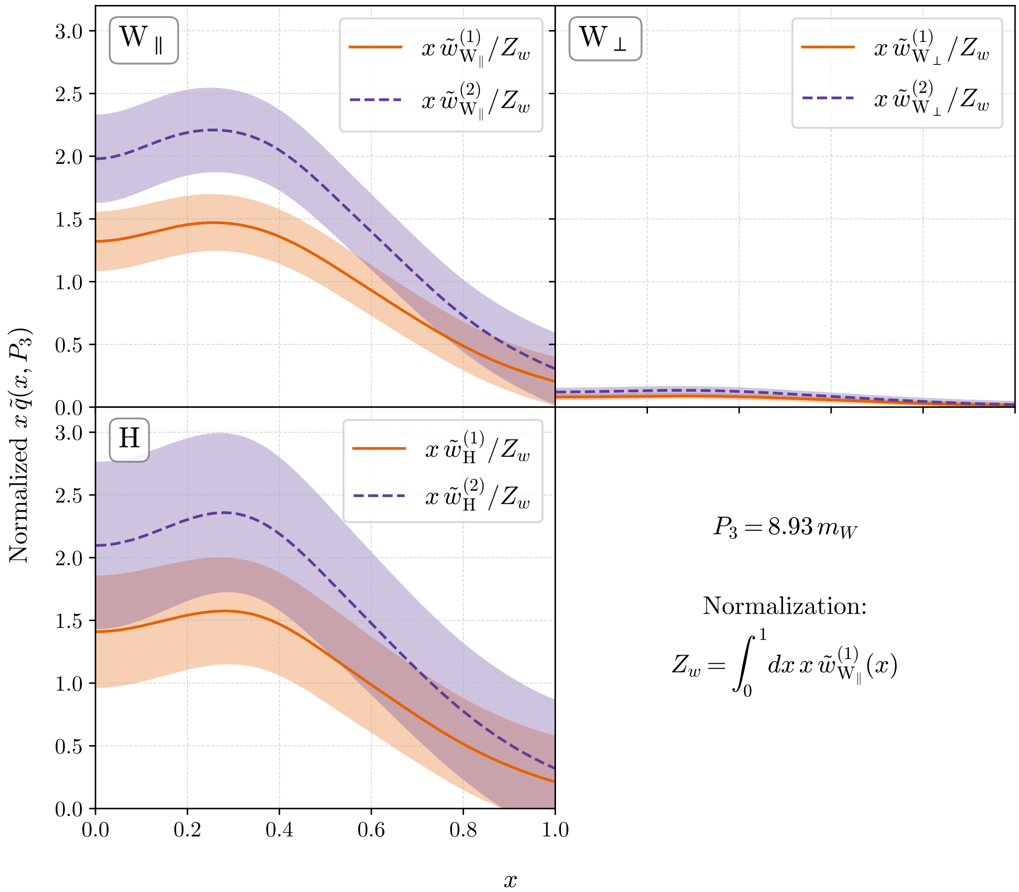

Fig. 6.26.: Same as Fig. 6.25, but for a larger boost momentum $P_3 = 8.93\,m_\mathrm{W} \approx 718\,\mathrm{GeV}$, with the Higgs-like quasi-PDFs excluded due to insufficient statistical precision.

6.4.3. Stability under Inclusion of a Fermion Term

To further test the stability of these results, we repeat the analysis including a fermion term in the Lagrangian. Fig. 6.27 shows similar plots as in Fig. 6.25, now including the fermion term in the Lagrangian, as specified in Table 5.1 (see Set 5 with fermions), on a smaller lattice of size $L = 20$ and at a smaller boost momentum $P_3 = 3.13\,m_\mathrm{W} \approx 252\,\mathrm{GeV}$. Since volume and momentum differ between the two setups, this comparison does not isolate the effect of the fermion term. Nonetheless, we observe that the overall structure of the quasi-PDFs remains unchanged.

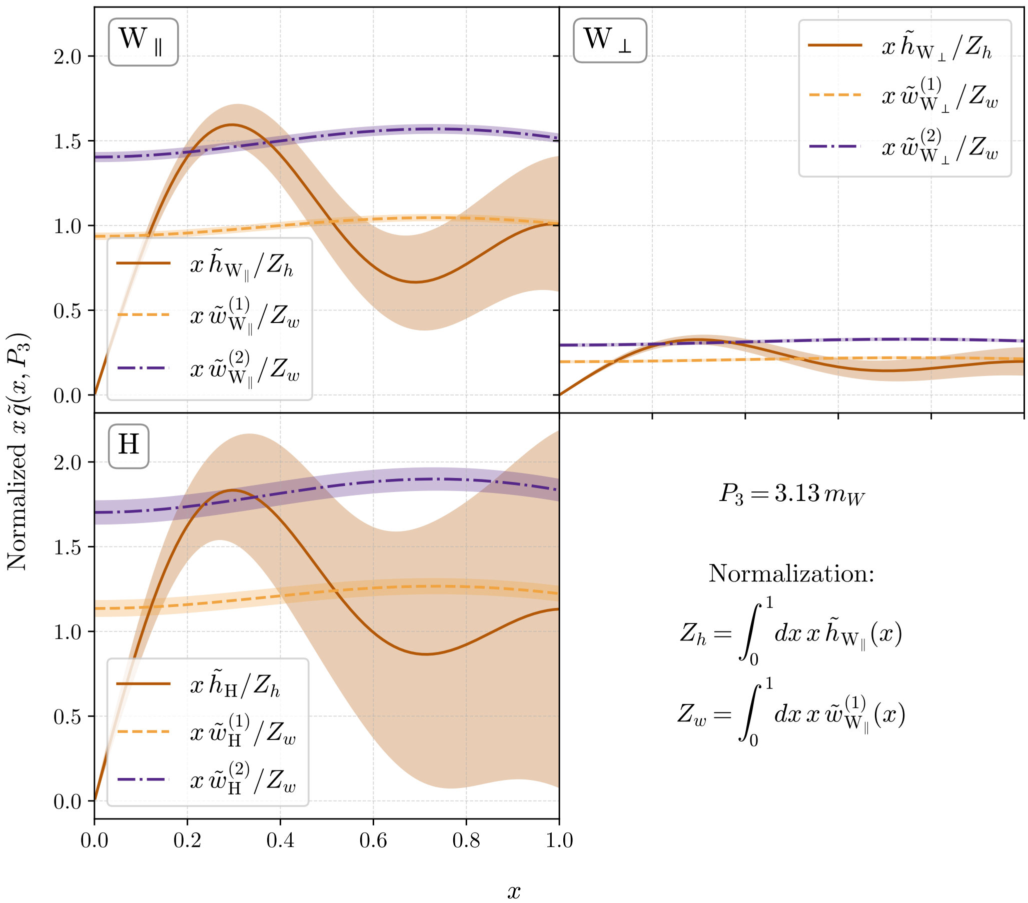

Fig. 6.27.: Obtained quasi-PDFs plotted as $x\tilde{q}(x, P_3)$ for Set 5 (with fermions) at $L = 20$ and boost momentum $P_3 = 3.13\,m_\mathrm{W} \approx 252\,\mathrm{GeV}$. The subplots correspond to the different composite states $\mathrm{W}_\parallel$, $\mathrm{W}_\perp$, and H. The quasi-PDFs are normalized to the quasi-PDFs in the $\mathrm{W}_\parallel$ mode.

This indicates that, for the investigated parameter range, the inclusion of the fermion term does not lead to a visible qualitative modification of the extracted quasi-PDFs within the present comparison.

6.5. Distinct Behavior of the $F_{1^-}^{(3)}$ Channel

In contrast to the behavior observed so far, the quasi-PDFs probed by $F_{1^-}^{(3)}$ exhibit qualitatively different features and therefore deserve a separate discussion, which is based on the results of Set 5. This probe current corresponds to a difference of tensor components that differ only by their index directions. Consequently, the individual contributions are expected to be of similar size, such that partial cancellations lead to a suppressed signal. This is consistent with the rest of the observations of this study, e.g. the similarity of the quasi-PDFs obtained by $F_{1^-}^{(1)}$ and $F_{1^-}^{(2)}$, as well as the canceling contributions of $M_{\mathrm{W}_\parallel}^{\mathrm{W}^{(3\,|\,ti)}}$ and $M_{\mathrm{W}_\parallel}^{\mathrm{W}^{(3\,|\,xy)}}$ shown in Figs. 6.7f and 6.8a. [2]

As expected, $M_{\mathrm{W}_\parallel}^{\mathrm{W}^{(3)}}$ and $M_{\mathrm{H}}^{\mathrm{W}^{(3)}}$ yield results that are compatible with zero within statistical uncertainties. Fig. 6.28 shows the matrix element for $\mathrm{W}_\parallel$ as a function of z for different boost momenta P_3. Most data points are consistent with zero within one standard deviation, with isolated deviations up to two standard deviations and no clear indication of a signal. The corresponding results for $M_{\mathrm{H}}^{\mathrm{W}^{(3)}}$ are included in the appendix (see Fig. B.16).

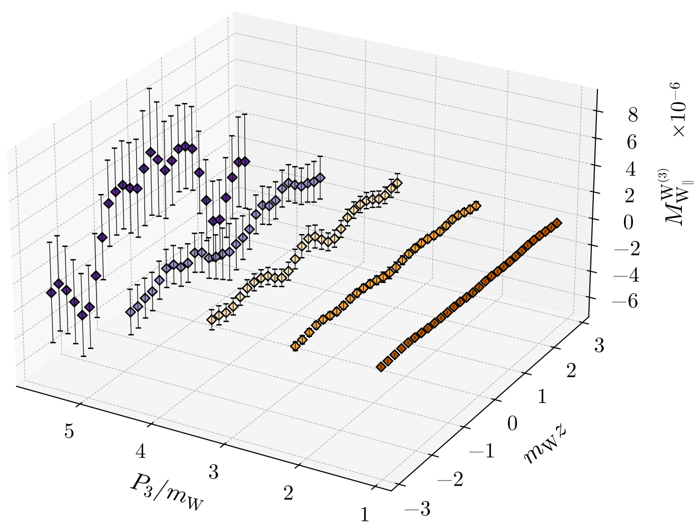

Fig. 6.28.: Momentum dependence of the matrix element $M_{\mathrm{W}_\parallel}^{\mathrm{W}^{(3)}}(z, P_3)$ for parameter Set 5 on the largest lattice volume $L = 28$.

In contrast to the absence of a signal in the $\mathrm{W}_\parallel$ and H channels, the matrix element $M_{\mathrm{W}_\perp}^{\mathrm{W}^{(3)}}$ exhibits a clear signal, as illustrated in Fig. 6.29. We observe a strong oscillatory behavior along the z-axis, symmetry around $z = 0$, and a negative value at $z = 0$. The

[2] The operator structure suggests a relation of the form $M_i^{\mathrm{W}^{(3)}} \sim M_i^{\mathrm{W}^{(3\,|\,ti)}} - 2M_i^{\mathrm{W}^{(3\,|\,xy)}}$, which is not expected to hold exactly for lattice observables.

oscillation has a frequency that appears to increase with the boost momentum and can be identified up to the fourth lattice momentum. Beyond this point, the growing uncertainties and the limited resolution in z obscure the signal.

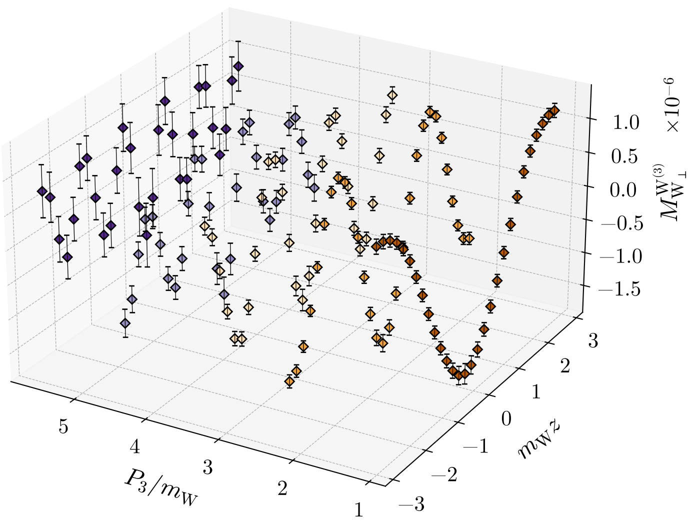

Fig. 6.29.: Momentum dependence of the matrix element $M_{\mathrm{W}_\perp}^{\mathrm{W}^{(3)}}(z, P_3)$ for parameter Set 5 on the largest lattice volume $L = 28$.

The quasi-PDFs are defined as the Fourier transform of the corresponding matrix elements. Therefore, an oscillation in the matrix element should lead to a peak in the distribution, which is observed in Fig. 6.30. Interestingly, the peak position is independent of the boost momentum and is located around $x \approx 1$ for the three lowest lattice momenta. Furthermore, the peak becomes sharper at higher boost momenta. The quasi-PDFs are normalized to the lowest momentum result, and the normalization includes an overall minus sign. The bare results for the quasi-PDFs are shown in Fig. B.44. Finally, it should be noted that the matrix elements do not decay sufficiently to zero within the lattice extent, which may introduce systematic effects in the discrete Fourier transform. These potential issues are not investigated further in this work.

The results for Set 1 show compatible behavior. The matrix elements for the H and $\mathrm{W}_\parallel$ channels, shown in Figs. B.3 and B.5, are consistent with zero. The matrix element $M_{\mathrm{W}_\perp}^{\mathrm{W}^{(3)}}$, previously shown in Fig. 6.15, still exhibits oscillatory features. However, the signal is rapidly suppressed as one moves away from $z = 0$, so that for the first and second lattice momenta no clear oscillatory pattern can be resolved. Only at the third lattice momentum does the behavior become sufficiently pronounced to identify the same qualitative structure as in Set 5.

Correspondingly, the peaks in the quasi-PDFs (see Fig. 6.31) are less pronounced. In particular, for the lowest momentum the quasi-PDF is nearly flat in x, with only a slight enhancement around $x \approx 1$. The result for the third lattice momentum, however, exhibits

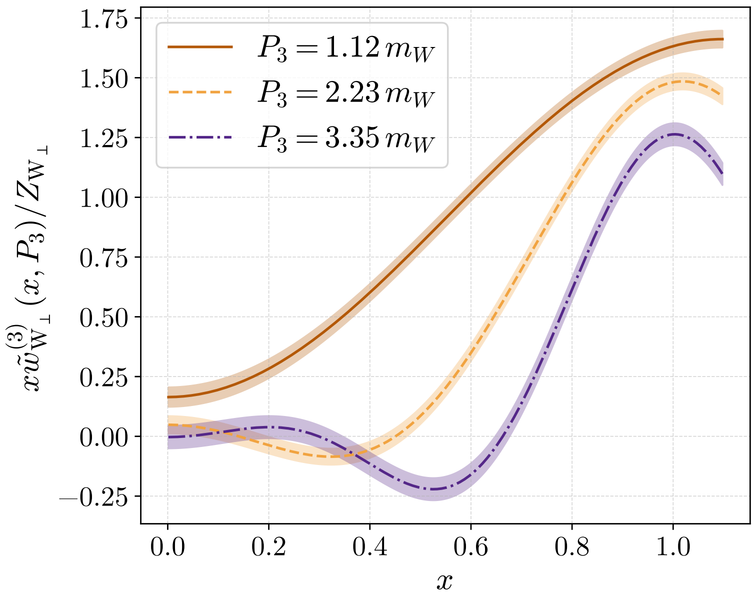

Fig. 6.30.: Quasi-PDF $x\,\tilde{w}^{(3)}_{\mathrm{W}_\perp}(x, P_3)$ as a function of x for different boost momenta P_3 (Set 5, $L = 28$). The normalization is defined as $Z_{\mathrm{W}_\perp} = \int_0^1 \mathrm{d}x\; x\, w^{(3)}_{\mathrm{W}_\perp}(x, P_3 = 1.12\, m_{\mathrm{W}})$.

a clear peak located at $x \approx 1$. The quasi-PDFs are normalized to the lowest-momentum result, and the corresponding bare quasi-PDFs are shown in Fig. 6.22.

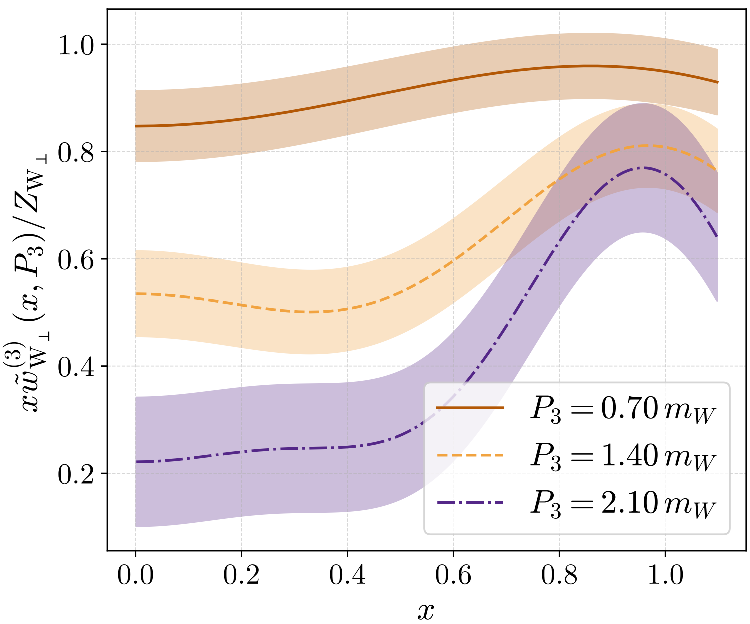

Fig. 6.31.: Quasi-PDF $x\,\tilde{w}^{(3)}_{\mathrm{W}_\perp}(x, P_3)$ as a function of x for different boost momenta P_3 (Set 1, $L = 32$). The normalization is defined as $Z_{\mathrm{W}_\perp} = \int_0^1 \mathrm{d}x\; x\, w^{(3)}_{\mathrm{W}_\perp}(x, P_3 = 0.70\, m_{\mathrm{W}})$.

Chapter 7.

Conclusion & Outlook

The extraction of the structure of the Higgs and the electroweak vector bosons from first-principles lattice QFT remains a challenging task. The quasi-PDF framework provides a way to access this information by relating spatially separated matrix elements to the corresponding light-cone distributions. In practical implementations, however, this approach requires calculations at large boost momenta and high statistical precision, resulting in substantial computational cost. In this work, we implemented this framework for the FMS composite states within a reduced electroweak setting, specifically the SU(2) gauge–scalar theory, to investigate the feasibility of this program.

The results presented in this thesis demonstrate that the relevant matrix elements can be extracted for both the physical Higgs and the physical vector bosons, for several probe currents and, in the case of the vector bosons, for different spin polarizations. Across most of the channels investigated, the matrix elements exhibit only a weak momentum dependence. While the W/Z-like probed matrix elements show strong localization at small spatial separations, and rapid decay with distance, the Higgs-like matrix elements are spatially more spread out and decay slowly. One channel corresponding to a W/Z-like PDF of the vector boson exhibits a noticeably oscillatory behavior as a function of the spatial separation. This behavior maps directly to a peak in the quasi-PDFs. For the investigated sets, these peaks lie at relatively large x, which one would expect from a naive partonic picture, where the physical vector bosons behave like the elementary ones. Although the physical origin of this feature has yet to be understood and remains speculative within the present analysis, it does indicate the potential emergence of nontrivial structures within this framework. These findings are, in general, consistent with the composite description employed in the FMS framework.

Taken together, these observations suggest that the quasi-PDF program can indeed be applied to the FMS setting and provide usable lattice signals for the considered composite states. At the same time, the present results do not yet contain a comprehensive interpretation as well as an investigation into their physical implications. Thus, these findings should be viewed as an exploratory step to a more detailed determination of the underlying structure of the physical electroweak particles.

However, a few aspects of the results deserve further comments. Firstly, across most matrix elements evaluated, the finite-size effects appear small in the volumes studied.

Carrying out the same analysis for different volumes led to no qualitative differences in the obtained results. While the Higgs-like matrix elements decay slowly, and therefore the remainder at the boundary depends on the volume, the subtraction procedure proves effective. For future analyses, investigations at lattice sizes similar to those employed in this work ($L \approx 28, 32$) appear to be sufficient for the present level of precision.

Furthermore, during the analysis it became apparent that smearing noticeably affects the matrix elements. This is especially true for the isotropic smearing of the probe currents specified in chapter 5, which directly influences the form of the matrix elements, e.g., the width of the peaks and therefore the resulting distributions. The dependence on the smearing procedure was not investigated systematically in this work.

As an exploratory study, the present work primarily establishes a first implementation of the quasi-PDF program in this reduced electroweak setting. The results raise several questions regarding the interpretation of the extracted matrix elements and indicate a number of possible continuations. Furthermore, the setting may be broadened to include additional aspects of the entire Standard Model. In the following paragraphs, several concrete directions for further investigation are outlined.

A question emerging from the results of this study is the pronounced dependence on the spin polarization. Depending on the probe current, we either obtain matrix elements that are consistent with zero for all boost momenta or vanish for high momenta. It is currently not understood whether this behavior originates from the operator construction, the choice of probe currents, or the underlying dynamics of the theory. A more detailed theoretical investigation would therefore be required to refine the interpretation of the current results.

The quasi-PDF framework generally consists of two parts: the non-perturbative calculation on the lattice and the perturbative matching to the corresponding light-cone distribution. The present work addresses only the first part of this program, and therefore, conclusions about the physical implications of the quasi-PDFs remain provisional. Completing the second step by deriving and applying the correct matching relations would allow the lattice results obtained here to be connected to their light-cone counterparts beyond the first qualitative statements provided in this thesis. Since the distributions considered here correspond to quasi-PDFs at finite momentum without matching, this important extension would enable a more direct interpretation of the calculated distributions.

The long-term goal is to describe collider experiments involving leptonic initial and final states as these correspond to the phenomenologically relevant scattering processes. Consequently, the PDFs with the most direct experimental relevance are those probing the leptonic composite states. The calculation of these distributions from first principles would therefore form the natural continuation of the present work. Achieving this objective would require extending the current program to include additional gauge-invariant lepton states together with the corresponding flavor-probing currents. However, the calculation would follow the same general strategy as used in the present analysis.

The resulting distributions could in principle provide a direct connection between the electroweak PDF formulation and experimentally accessible observables.

In the end, for a decisive physical interpretation of the present results, further experimental data is essential, in particular in the kinematic regime where the electroweak compositeness could become resolved. The proposed FCC-ee collider may provide the missing pieces that are needed to fill in our current lack of understanding.

Bibliography

[1] S. Navas et al. "Review of Particle Physics." In: *Phys. Rev. D* 110.3 (Aug. 2024), p. 030001. DOI: 10.1103/PhysRevD.110.030001.

[2] M. D. Schwartz. *Quantum Field Theory and the Standard Model*. Cambridge University Press, Dec. 2013. ISBN: 9781107034730. DOI: 10.1017/9781139540940.

[3] R. Aliberti et al. "The anomalous magnetic moment of the muon in the Standard Model: an update." In: *Phys. Rep.* 1143 (Nov. 2025), pp. 1–158. DOI: 10.1016/j.physrep.2025.08.002. arXiv: 2505.21476.

[4] A. Abada et al. "FCC-ee: The Lepton Collider: Future Circular Collider Conceptual Design Report Volume 2." In: *Eur. Phys. J. Special Topics* 228.2 (June 2019), pp. 261–623. DOI: 10.1140/epjst/e2019-900045-4.

[5] L. Egger, A. Maas, and R. Sondenheimer. "Pair production processes and flavor in gauge-invariant perturbation theory." In: *Mod. Phys. Lett. A* 32.38 (Dec. 2017), p. 1750212. DOI: 10.1142/s0217732317502121. arXiv: 1701.02881.

[6] A. Maas. "Brout–Englert–Higgs physics: From foundations to phenomenology." In: *Prog. Part. Nucl. Phys.* 106 (May 2019), pp. 132–209. DOI: 10.1016/j.ppnp.2019.02.003. arXiv: 1712.04721.

[7] C. W. Bauer, N. Ferland, and B. R. Webber. "Standard Model parton distributions at very high energies." In: *J. High Energy Phys.* 2017.8 (Aug. 2017). DOI: 10.1007/jhep08(2017)036. arXiv: 1703.08562.

[8] C. W. Bauer, N. Ferland, and B. R. Webber. "Combining initial-state resummation with fixed-order calculations of electroweak corrections." In: *J. High Energy Phys.* 2018.4 (Apr. 2018). DOI: 10.1007/jhep04(2018)125. arXiv: 1712.07147.

[9] C. W. Bauer, D. Provasoli, and B. R. Webber. "Standard Model fragmentation functions at very high energies." In: *J. High Energy Phys.* 2018.11 (Nov. 2018). DOI: 10.1007/jhep11(2018)030. arXiv: 1806.10157.

[10] C. W. Bauer and B. R. Webber. "Polarization effects in standard model parton distributions at very high energies." In: *J. High Energy Phys.* 2019.3 (Mar. 2019). DOI: 10.1007/jhep03(2019)013. arXiv: 1808.08831.

[11] T. Han, Y. Ma, and K. Xie. "High energy leptonic collisions and electroweak parton distribution functions." In: *Phys. Rev. D* 103.3 (Feb. 2021), p. L031301. DOI: 10.1103/PhysRevD.103.L031301. arXiv: 2007.14300.

[12] T. Han, Y. Ma, and K. Xie. "Quark and gluon contents of a lepton at high energies." In: *J. High Energy Phys.* 2022.2 (Feb. 2022). DOI: 10.1007/jhep02(2022)154. arXiv: 2103.09844.

[13] R. Ruiz et al. "The Effective Vector Boson Approximation in high-energy muon collisions." In: *J. High Energy Phys.* 2022.6 (June 2022). DOI: 10.1007/jhep06(2022)114. arXiv: 2111.02442.

[14] F. Garosi, D. Marzocca, and S. Trifinopoulos. "LePDF: Standard Model PDFs for high-energy lepton colliders." In: *J. High Energy Phys.* 2023.9 (Sept. 2023). DOI: 10.1007/jhep09(2023)107. arXiv: 2303.16964.

[15] V. Afferrante et al. "Testing the mechanism of lepton compositeness." In: *SciPost Phys.* 10.3 (Mar. 2021). DOI: 10.21468/scipostphys.10.3.062. arXiv: 2011.02301.

[16] G. Wieland and A. Maas. *Spectrum of the SU(2) scalar-fermion-gauge system under the influence of the Brout-Englert-Higgs effect.* Oct. 2025. DOI: 10.48550/ARXIV.2510.27457. arXiv: 2510.27457.

[17] A. Maas. "The Fröhlich–Morchio–Strocchi Mechanism: An Underestimated Legacy." In: *Trails in modern theoretical and mathematical physics: A volume in tribute to Giovanni Morchio.* Ed. by A. Cintio and A. Michelangeli. Cham: Springer International Publishing, Dec. 2023, pp. 177–205. ISBN: 9783031449888. DOI: 10.1007/978-3-031-44988-8_11. arXiv: 2305.01960.

[18] S. Elitzur. "Impossibility of spontaneously breaking local symmetries." In: *Phys. Rev. D* 12.12 (Dec. 1975), pp. 3978–3982. DOI: 10.1103/PhysRevD.12.3978.

[19] J. Fröhlich, G. Morchio, and F. Strocchi. "Higgs phenomenon without a symmetry breaking order parameter." In: *Phys. Lett. B* 97.2 (Dec. 1980), pp. 249–252. DOI: 10.1016/0370-2693(80)90594-8.

[20] J. Fröhlich, G. Morchio, and F. Strocchi. "Higgs phenomenon without symmetry breaking order parameter." In: *Nucl. Phys. B* 190.3 (Oct. 1981), pp. 553–582. DOI: 10.1016/0550-3213(81)90448-X.

[21] M. Böhm, A. Denner, and H. Joos. *Gauge Theories of the Strong and Electroweak Interaction.* Vieweg+Teubner Verlag, 2001. ISBN: 9783322801609. DOI: 10.1007/978-3-322-80160-9.

[22] R. P. Feynman. "Very High-Energy Collisions of Hadrons." In: *Phys. Rev. Lett.* 23.24 (Dec. 1969), pp. 1415–1417. DOI: 10.1103/PhysRevLett.23.1415.

[23] J. D. Bjorken and E. A. Paschos. "Inelastic Electron-Proton and γ-Proton Scattering and the Structure of the Nucleon." In: *Phys. Rev.* 185.5 (Sept. 1969), pp. 1975–1982. DOI: 10.1103/PhysRev.185.1975.

[24] C. Gattringer and C. B. Lang. *Quantum Chromodynamics on the Lattice: An Introductory Presentation.* Vol. 788. Springer Science & Business Media, 2010. ISBN: 9783642018503. DOI: 10.1007/978-3-642-01850-3.

[25] I. Montvay and G. Münster. *Quantum fields on a lattice.* Ed. by G. Münster. Cambridge monographs on mathematical physics. Cambridge: Cambridge University Press, 1994. ISBN: 9780511470783. DOI: 10.1017/cbo9780511470783.

[26] B. Riederer. "On Gauge-Scalar-Theories: The many aspects of the Brout-Englert-Higgs effect." URN: urn:nbn:at:at-ubg:1-188305. PhD thesis. Universität Graz, Feb. 2023.

[27] H. Evertz et al. "SU(2) Higgs Boson and vector Boson masses on the lattice." In: *Phys. Lett. B* 171.2–3 (Apr. 1986), pp. 271–279. DOI: 10.1016/0370-2693(86)91547-9.

[28] P. Jenny, A. Maas, and B. Riederer. "Vector boson scattering from the lattice." In: *Phys. Rev. D* 105.11 (June 2022), p. 114513. DOI: 10.1103/PhysRevD.105.114513. arXiv: 2204.02756.

[29] X. Ji. "Parton Physics on a Euclidean Lattice." In: *Phys. Rev. Lett.* 110.26 (June 2013), p. 262002. DOI: 10.1103/PhysRevLett.110.262002. arXiv: 1306.1539.

[30] K. Cichy and M. Constantinou. "A Guide to Light-Cone PDFs from Lattice QCD: An Overview of Approaches, Techniques, and Results." In: *Adv. High Energy Phys.* 2019.1 (June 2019), p. 3036904. DOI: 10.1155/2019/3036904. arXiv: 1811.07248.

[31] A. Maas and F. Reiner. "Restoring the Bloch-Nordsieck theorem in the electroweak sector of the standard model." In: *Phys. Rev. D* 108.1 (July 2023), p. 013001. DOI: 10.1103/PhysRevD.108.013001. arXiv: 2212.08470.

[32] C. Alexandrou et al. "Lattice calculation of parton distributions." In: *Phys. Rev. D* 92.1 (July 2015), p. 014502. DOI: 10.1103/PhysRevD.92.014502. arXiv: 1504.07455.

[33] W. Wang, S. Zhao, and R. Zhu. "Gluon quasidistribution function at one loop." In: *Eur. Phys. J. C* 78.2 (Feb. 2018). DOI: 10.1140/epjc/s10052-018-5617-3. arXiv: 1708.02458.

[34] Z. Fan, R. Zhang, and H.-W. Lin. "Nucleon Gluon Distribution Function from 2+1+1-Flavor Lattice QCD." In: *Int. J. Mod. Phys. A* 36.13 (Apr. 2021), p. 2150080. DOI: 10.1142/s0217751x21500809. arXiv: 2007.16113 [hep-lat].

[35] T. Khan et al. "Unpolarized gluon distribution in the nucleon from lattice quantum chromodynamics." In: *Phys. Rev. D* 104.9 (Nov. 2021), p. 094516. DOI: 10.1103/PhysRevD.104.094516. arXiv: 2107.08960.

[36] I. Balitsky, W. Morris, and A. Radyushkin. "Gluon pseudo-distributions at short distances: Forward case." In: *Phys. Lett. B* 808 (2020), p. 135621. DOI: 10.1016/j.physletb.2020.135621. arXiv: 1910.13963.

[37] W. Good, K. Hasan, and H.-W. Lin. *Toward the First Gluon Parton Distribution from the LaMET*. Sept. 2024. DOI: 10.48550/ARXIV.2409.02750. arXiv: 2409.02750.

[38] L. Del Debbio, A. Patella, and C. Pica. "Higher representations on the lattice: Numerical simulations, SU(2) with adjoint fermions." In: *Phys. Rev. D* 81.9 (May 2010), p. 094503. DOI: 10.1103/PhysRevD.81.094503. arXiv: 0805.2058.

[39] A. Maas and T. Mufti. "Two- and three-point functions in Landau gauge Yang-Mills-Higgs theory." In: *J. High Energy Phys.* 2014.4 (Apr. 2014). DOI: 10.1007/jhep04(2014)006. arXiv: 1312.4873.

[40] A. Maas and T. Mufti. "Spectroscopic analysis of the phase diagram of Yang-Mills-Higgs theory." In: *Phys. Rev. D* 91.11 (June 2015), p. 113011. DOI: 10.1103/PhysRevD.91.113011. arXiv: 1412.6440.

[41] O. Philipsen, M. Teper, and H. Wittig. "On the mass spectrum of the SU(2) Higgs model in 2+1 dimensions." In: *Nucl. Phys. B* 469.3 (June 1996), pp. 445–469. DOI: 10.1016/0550-3213(96)00156-3. arXiv: hep-lat/9602006.

[42] M. Wurtz and R. Lewis. "Higgs and W boson spectrum from lattice simulations." In: *Phys. Rev. D* 88.5 (Sept. 2013), p. 054510. DOI: 10.1103/PhysRevD.88.054510. arXiv: 1307.1492.

Appendix A.

Further details on the extraction of matrix elements

This appendix gathers additional information regarding the extraction of matrix elements and the corresponding quasi-PDF, which is not essential for the main discussion.

A.1. Additional Simulation Parameters

The used fit ranges for the source-sink separations for the different lattice sizes are displayed in Table A.1.

Table A.1.: Source-sink separation fit ranges for different lattice sizes L.

L	$t_s^{\min}$	$t_s^{\max}$
8	2	4
12	2	4
16	2	4
20	2	5
24	2	5
28	2	5
32	2	5

The maximal Wilson-line extent $z_{\max}$ for the two types of quasi-PDFs (Higgs-like or W/Z-like) is listed in Table A.2.

Table A.2.: Maximal Wilson-line extent $z_{\max}$ as a function of the lattice size L for the different quasi-PDF types.

	$\tilde{h}_i$	$\tilde{w}_i$
$z_{\max}$	$3L/4$	$L/2$

A.2. Overview of Quasi-PDFs

For reference, this section provides a complete overview of all quasi-PDFs considered in this work, together with the corresponding matrix elements, correlation functions, and internal data labels.

Table A.3.: Overview of different quasi-PDF types with corresponding matrix element, three-point function, two-point function and label used in data files.

No.	quasi-PDF	M_i^j	$C^{3\text{pt}}$	$C^{2\text{pt}}$	Label
1	$\tilde{h}_{\mathrm{H}}$	$M_{\mathrm{H}}^{\mathrm{H}}$	$C_{\mathrm{HH}}^{3\mathrm{pt}}$	$C_{\mathrm{H}}^{2\mathrm{pt}}$	`HH`
2	$\tilde{h}_{\mathrm{W}_\parallel}$	$M_{\mathrm{W}_\parallel}^{\mathrm{H}}$	$C_{\mathrm{HW}_\parallel}^{3\mathrm{pt}}$	$C_{\mathrm{W}}^{2\mathrm{pt}}$	`HW_LON`
3	$\tilde{h}_{\mathrm{W}_\perp}$	$M_{\mathrm{W}_\perp}^{\mathrm{H}}$	$C_{\mathrm{HW}_\perp}^{3\mathrm{pt}}$	$C_{\mathrm{W}}^{2\mathrm{pt}}$	`HW_TRA`
4	$\tilde{w}_{\mathrm{H}}^{(1)}$	$M_{\mathrm{H}}^{\mathrm{W}^{(1)}}$	$C_{\mathrm{WH}^{(1)}}^{3\mathrm{pt}}$	$C_{\mathrm{H}}^{2\mathrm{pt}}$	`WH_1`
5	$\tilde{w}_{\mathrm{H}}^{(2)}$	$M_{\mathrm{H}}^{\mathrm{W}^{(2)}}$	$C_{\mathrm{WH}^{(2)}}^{3\mathrm{pt}}$	$C_{\mathrm{H}}^{2\mathrm{pt}}$	`WH_2`
6	$\tilde{w}_{\mathrm{H}}^{(3)}$	$M_{\mathrm{H}}^{\mathrm{W}^{(3)}}$	$C_{\mathrm{WH}^{(3)}}^{3\mathrm{pt}}$	$C_{\mathrm{H}}^{2\mathrm{pt}}$	`WH_3`
7	$\tilde{w}_{\mathrm{H}}^{(3\,\vert\,ti)}$	$M_{\mathrm{H}}^{\mathrm{W}^{(3\,\vert\,ti)}}$	$C_{\mathrm{WH}^{(3\,\vert\,ti)}}^{3\mathrm{pt}}$	$C_{\mathrm{H}}^{2\mathrm{pt}}$	`WH_3_TI`
8	$\tilde{w}_{\mathrm{H}}^{(3\,\vert\,xy)}$	$M_{\mathrm{H}}^{\mathrm{W}^{(3\,\vert\,xy)}}$	$C_{\mathrm{WH}^{(3\,\vert\,xy)}}^{3\mathrm{pt}}$	$C_{\mathrm{H}}^{2\mathrm{pt}}$	`WH_3_XY`
9	$\tilde{w}_{\mathrm{W}_\parallel}^{(1)}$	$M_{\mathrm{W}_\parallel}^{\mathrm{W}^{(1)}}$	$C_{\mathrm{WW}_\parallel^{(1)}}^{3\mathrm{pt}}$	$C_{\mathrm{W}}^{2\mathrm{pt}}$	`WW_LON_1`
10	$\tilde{w}_{\mathrm{W}_\parallel}^{(2)}$	$M_{\mathrm{W}_\parallel}^{\mathrm{W}^{(2)}}$	$C_{\mathrm{WW}_\parallel^{(2)}}^{3\mathrm{pt}}$	$C_{\mathrm{W}}^{2\mathrm{pt}}$	`WW_LON_2`
11	$\tilde{w}_{\mathrm{W}_\parallel}^{(3)}$	$M_{\mathrm{W}_\parallel}^{\mathrm{W}^{(3)}}$	$C_{\mathrm{WW}_\parallel^{(3)}}^{3\mathrm{pt}}$	$C_{\mathrm{W}}^{2\mathrm{pt}}$	`WW_LON_3`
12	$\tilde{w}_{\mathrm{W}_\parallel}^{(3\,\vert\,ti)}$	$M_{\mathrm{W}_\parallel}^{\mathrm{W}^{(3\,\vert\,ti)}}$	$C_{\mathrm{WW}_\parallel^{(3\,\vert\,ti)}}^{3\mathrm{pt}}$	$C_{\mathrm{W}}^{2\mathrm{pt}}$	`WW_LON_3_TI`
13	$\tilde{w}_{\mathrm{W}_\parallel}^{(3\,\vert\,xy)}$	$M_{\mathrm{W}_\parallel}^{\mathrm{W}^{(3\,\vert\,xy)}}$	$C_{\mathrm{WW}_\parallel^{(3\,\vert\,xy)}}^{3\mathrm{pt}}$	$C_{\mathrm{W}}^{2\mathrm{pt}}$	`WW_LON_3_XY`
14	$\tilde{w}_{\mathrm{W}_\perp}^{(1)}$	$M_{\mathrm{W}_\perp}^{\mathrm{W}^{(1)}}$	$C_{\mathrm{WW}_\perp^{(1)}}^{3\mathrm{pt}}$	$C_{\mathrm{W}}^{2\mathrm{pt}}$	`WW_TRA_1`
15	$\tilde{w}_{\mathrm{W}_\perp}^{(2)}$	$M_{\mathrm{W}_\perp}^{\mathrm{W}^{(2)}}$	$C_{\mathrm{WW}_\perp^{(2)}}^{3\mathrm{pt}}$	$C_{\mathrm{W}}^{2\mathrm{pt}}$	`WW_TRA_2`
16	$\tilde{w}_{\mathrm{W}_\perp}^{(3)}$	$M_{\mathrm{W}_\perp}^{\mathrm{W}^{(3)}}$	$C_{\mathrm{WW}_\perp^{(3)}}^{3\mathrm{pt}}$	$C_{\mathrm{W}}^{2\mathrm{pt}}$	`WW_TRA_3`
17	$\tilde{w}_{\mathrm{W}_\perp}^{(3\,\vert\,ti)}$	$M_{\mathrm{W}_\perp}^{\mathrm{W}^{(3\,\vert\,ti)}}$	$C_{\mathrm{WW}_\perp^{(3\,\vert\,ti)}}^{3\mathrm{pt}}$	$C_{\mathrm{W}}^{2\mathrm{pt}}$	`WW_TRA_3_TI`
18	$\tilde{w}_{\mathrm{W}_\perp}^{(3\,\vert\,xy)}$	$M_{\mathrm{W}_\perp}^{\mathrm{W}^{(3\,\vert\,xy)}}$	$C_{\mathrm{WW}_\perp^{(3\,\vert\,xy)}}^{3\mathrm{pt}}$	$C_{\mathrm{W}}^{2\mathrm{pt}}$	`WW_TRA_3_XY`

Appendix B.

Additional results

B.1. Additional Correlation Functions

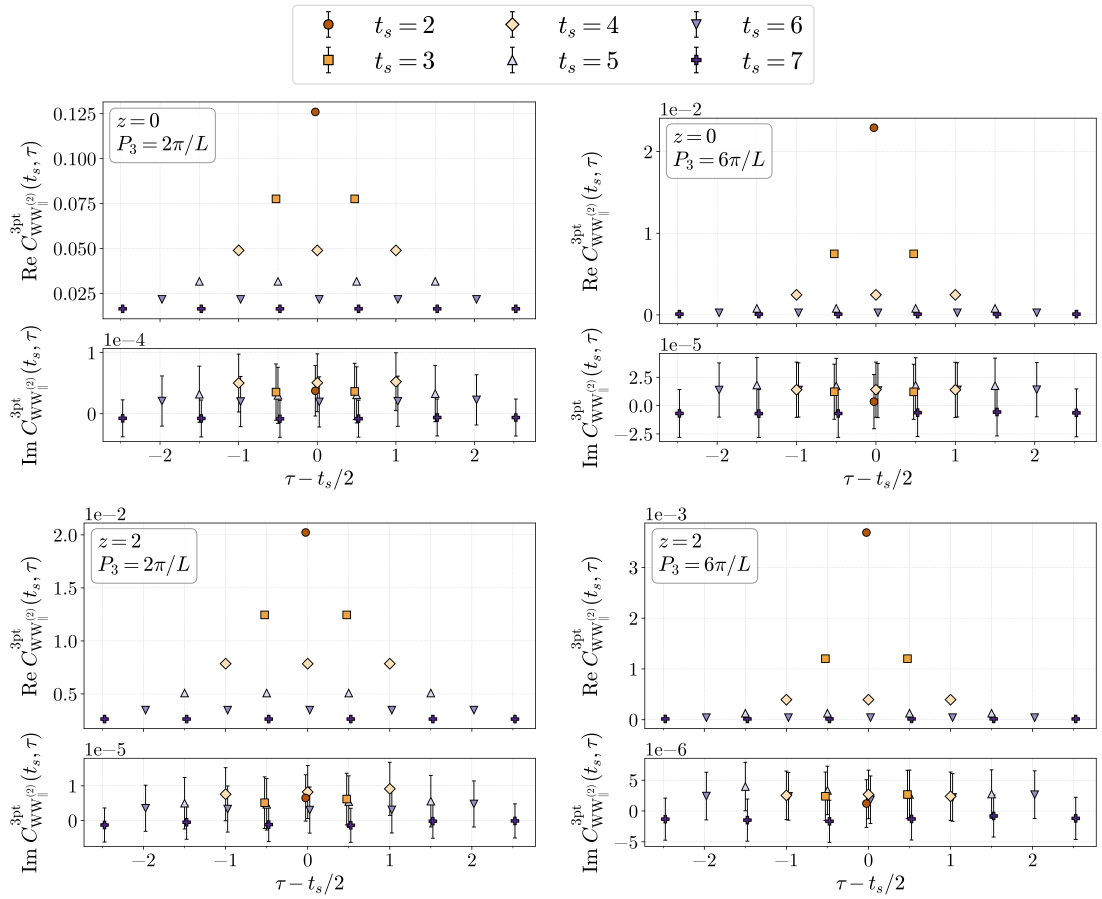

Fig. B.1.: Representative three-point correlation functions $C^{\mathrm{3pt}}_{\mathrm{WW}^{(2)}_{\parallel}}$ for different sink–source separations t_s, plotted as a function of $\tau - t_s/2$. The left column shows results for $P_3 = 2\pi/L$, while the right column corresponds to $P_3 = 6\pi/L$. Data are taken from Set 1 on a lattice of size $L = 16$.

B.2. Complete Matrix-Element Plots for Set 1

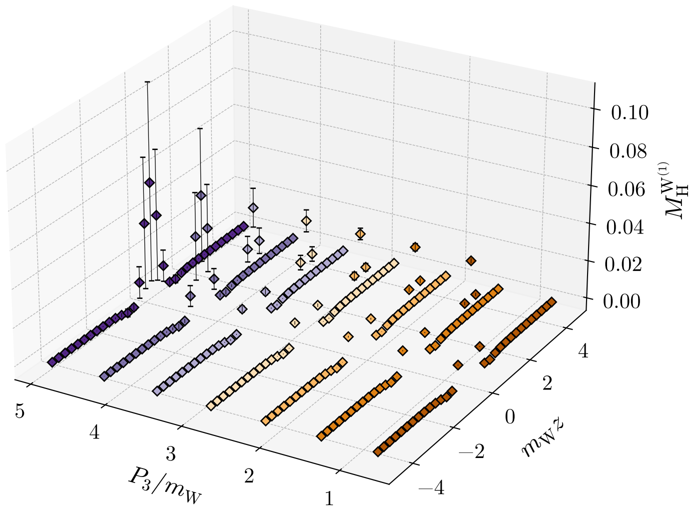

Fig. B.2.: Momentum dependence of the matrix element $M_{\mathrm{H}}^{\mathrm{W}^{(1)}}(z, P_3)$ for parameter Set 1 on the largest lattice volume $L = 32$.

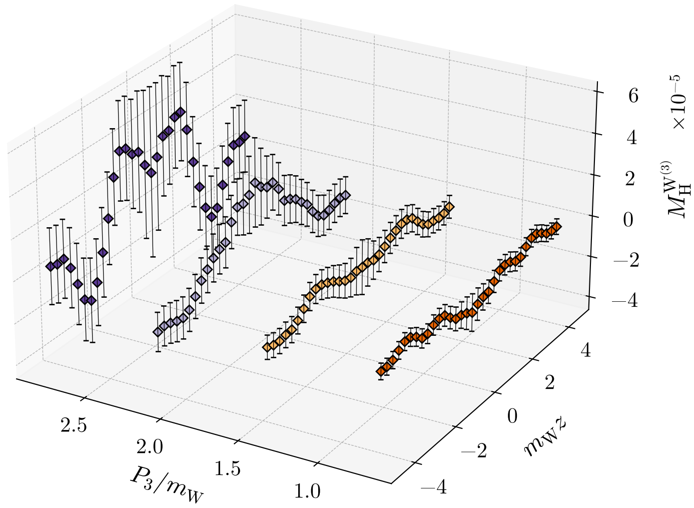

Fig. B.3.: Momentum dependence of the matrix element $M_{\mathrm{H}}^{\mathrm{W}^{(3)}}(z, P_3)$ for parameter Set 1 on the largest lattice volume $L = 32$.

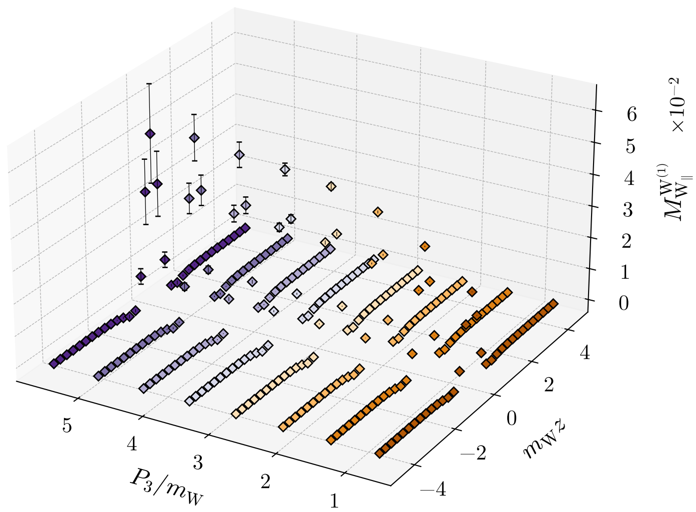

Fig. B.4.: Momentum dependence of the matrix element $M_{\mathrm{W}_\parallel}^{\mathrm{W}^{(1)}}(z, P_3)$ for parameter Set 1 on the largest lattice volume $L = 32$.

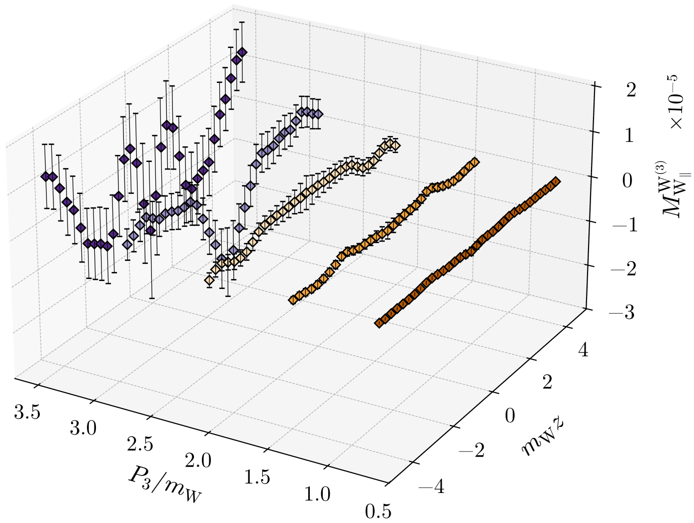

Fig. B.5.: Momentum dependence of the matrix element $M_{\mathrm{W}_\parallel}^{\mathrm{W}^{(3)}}(z, P_3)$ for parameter Set 1 on the largest lattice volume $L = 32$.

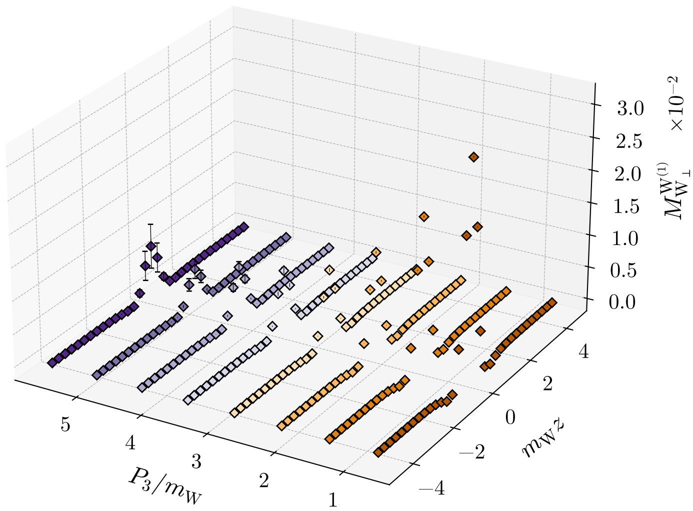

Fig. B.6.: Momentum dependence of the matrix element $M_{\mathrm{W}_\perp}^{\mathrm{W}^{(1)}}(z, P_3)$ for parameter Set 1 on the largest lattice volume $L = 32$.

B.3. Finite-Volume Effects on the Unimproved Matrix Elements (Set 1)

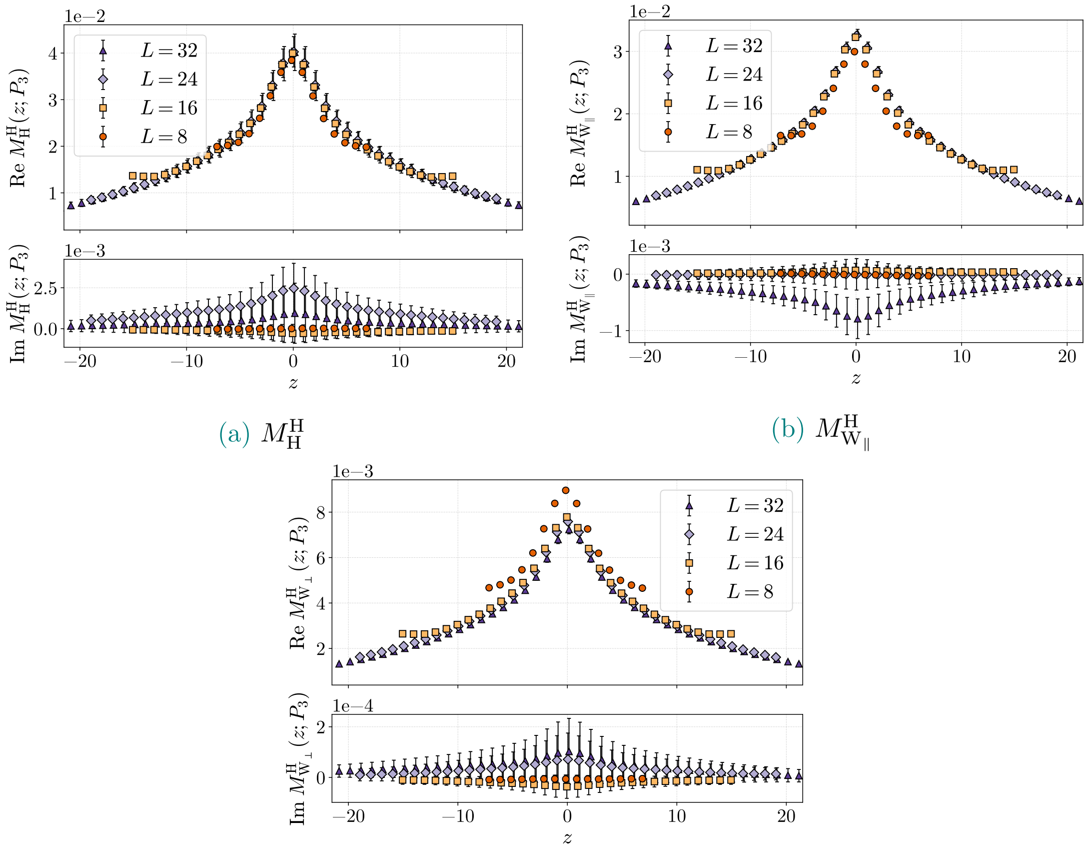

(a) $M^{\mathrm{H}}_{\mathrm{H}}$

(b) $M^{\mathrm{H}}_{\mathrm{W}_\parallel}$

(c) $M^{\mathrm{H}}_{\mathrm{W}_\perp}$

Fig. B.7.: Finite-size effects in the real and imaginary parts of the unimproved matrix elements $M_i^{\mathrm{H}}(z, P_3)$ for parameter Set 1 at fixed boost momentum $P_3 = 2\pi/8$ (in lattice units). For each matrix element, results from four lattice volumes $L = 8, 16, 24, 32$ are compared.

B.4. Finite-Volume Effects on the Matrix Elements (Set 5)

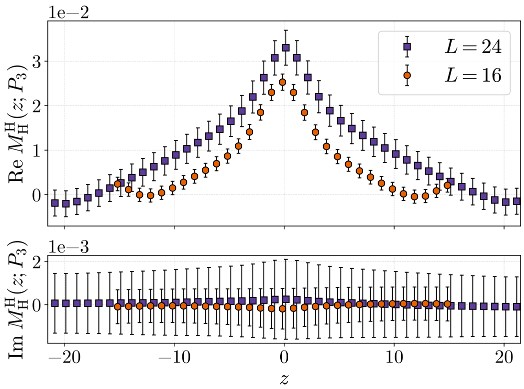

(a) $M_{\mathrm{H}}^{\mathrm{H}}$

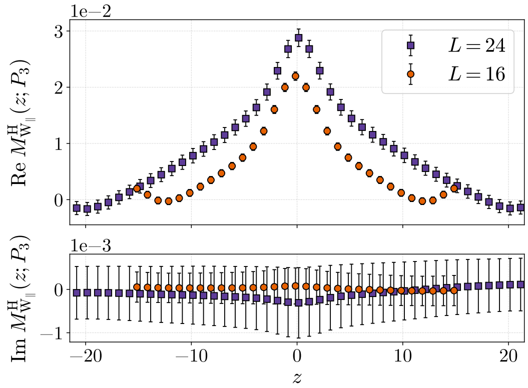

(b) $M_{\mathrm{W}_\parallel}^{\mathrm{H}}$

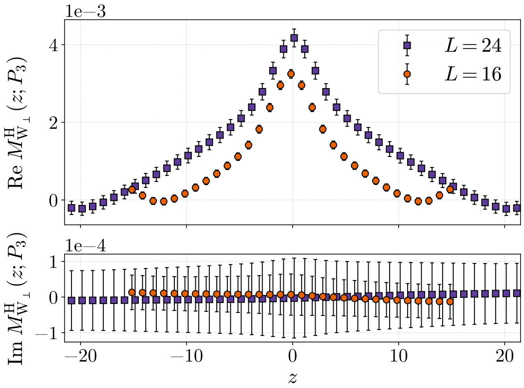

(c) $M_{\mathrm{W}_\perp}^{\mathrm{H}}$

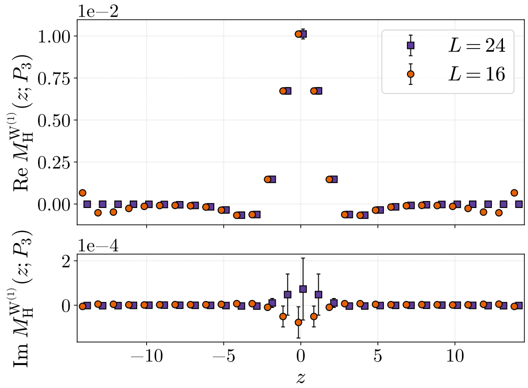

(d) $M_{\mathrm{H}}^{\mathrm{W}^{(1)}}$

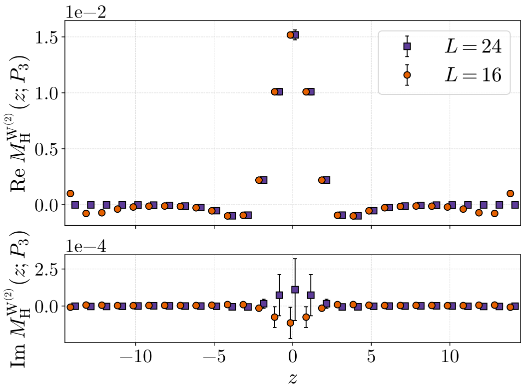

(e) $M_{\mathrm{H}}^{\mathrm{W}^{(2)}}$

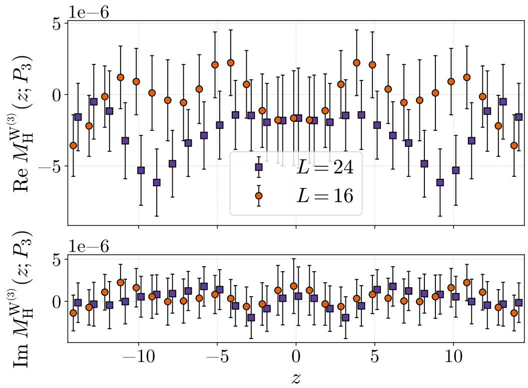

(f) $M_{\mathrm{H}}^{\mathrm{W}^{(3)}}$

Fig. B.8.: Finite-size effects in the real and imaginary parts of the matrix elements $M_i(z, P_3)$ for parameter Set 5 at fixed boost momentum $P_3 = 2\pi/8$ (in lattice units). For each matrix element, results from two lattice volumes $L = 16, 24$ are compared. Panels (a)–(f) show matrix elements 1–6.

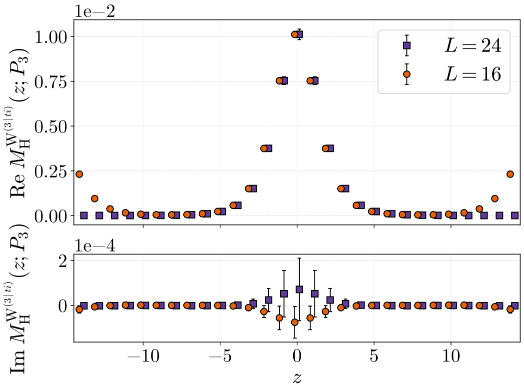

(a) $M_{\mathrm{H}}^{\mathrm{W}^{(3\,|\,ti)}}$

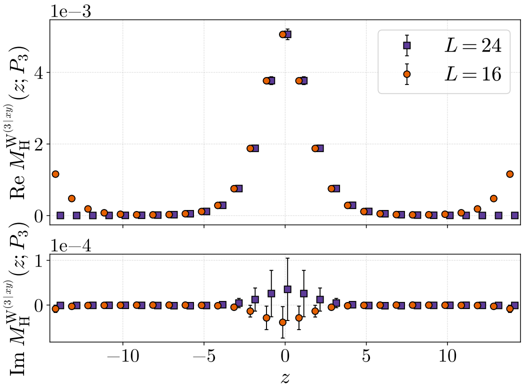

(b) $M_{\mathrm{H}}^{\mathrm{W}^{(3\,|\,ti)}}$

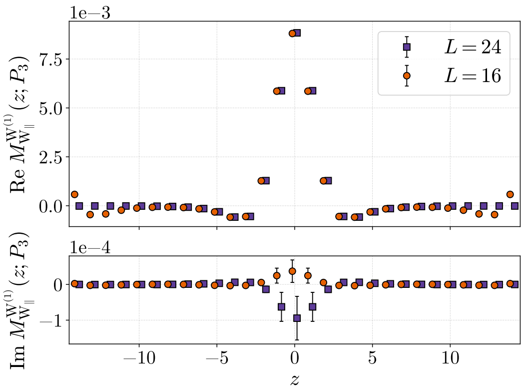

(c) $M_{\mathrm{W}_\parallel}^{\mathrm{W}^{(1)}}$

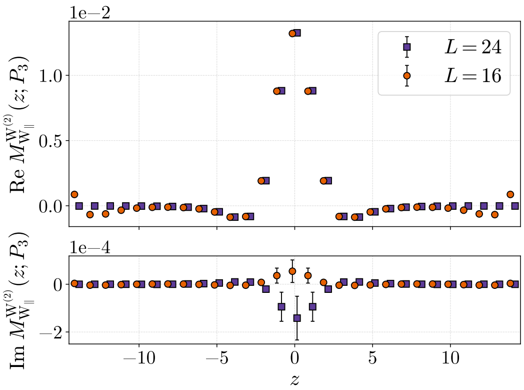

(d) $M_{\mathrm{W}_\parallel}^{\mathrm{W}^{(2)}}$

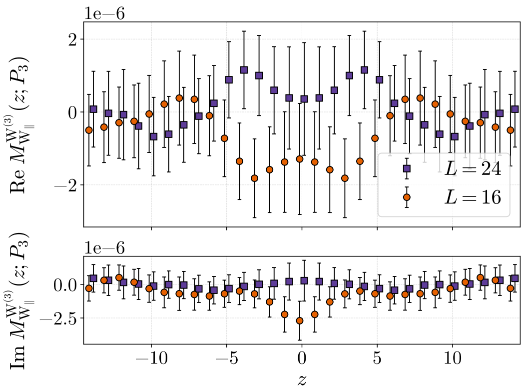

(e) $M_{\mathrm{W}_\parallel}^{\mathrm{W}^{(3)}}$

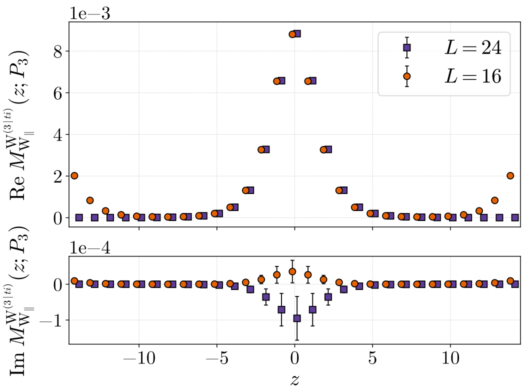

(f) $M_{\mathrm{W}_\parallel}^{\mathrm{W}^{(3\,|\,ti)}}$

Fig. B.9.: Same as Fig. B.8, but for matrix elements 7–12.

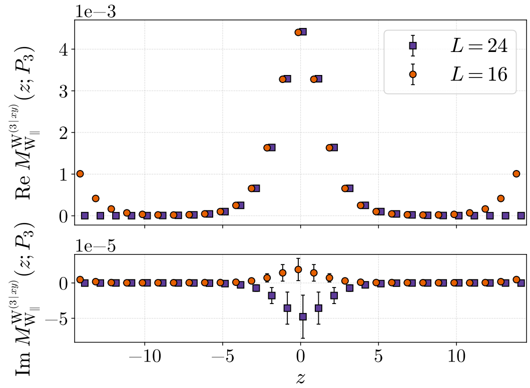

(a) $M_{\mathrm{W}_\parallel}^{\mathrm{W}^{(3\,|\,xy)}}$

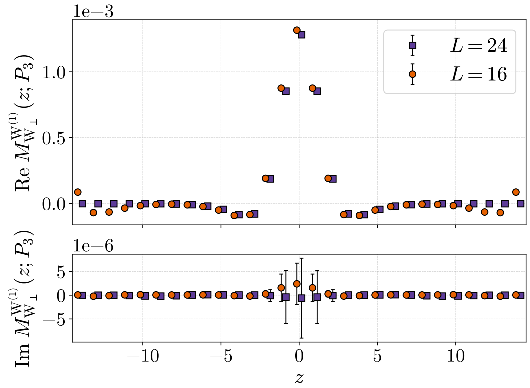

(b) $M_{\mathrm{W}_\perp}^{\mathrm{W}^{(1)}}$

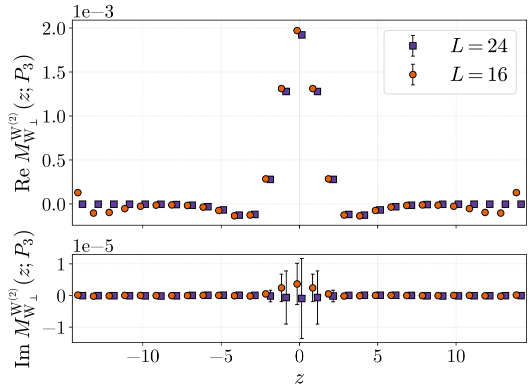

(c) $M_{\mathrm{W}_\perp}^{\mathrm{W}^{(2)}}$

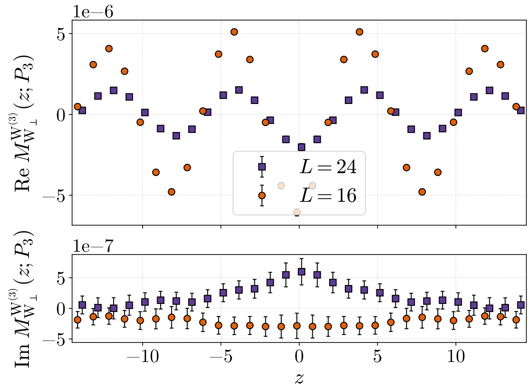

(d) $M_{\mathrm{W}_\perp}^{\mathrm{W}^{(3)}}$

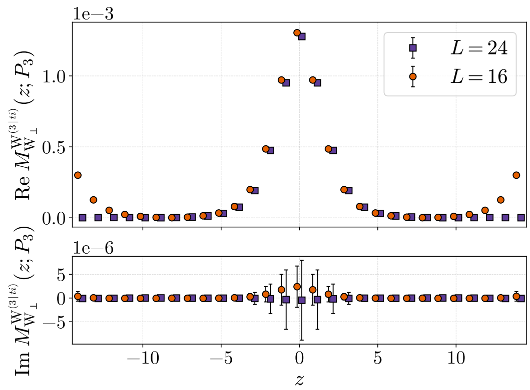

(e) $M_{\mathrm{W}_\perp}^{\mathrm{W}^{(3\,|\,ti)}}$

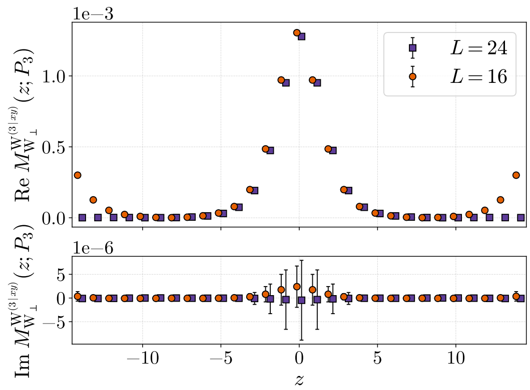

(f) $M_{\mathrm{W}_\perp}^{\mathrm{W}^{(3\,|\,xy)}}$

Fig. B.10.: Same as Fig. B.8, but for matrix elements 13–18.

B.5. Momentum Dependence of the Matrix Elements (Set 5)

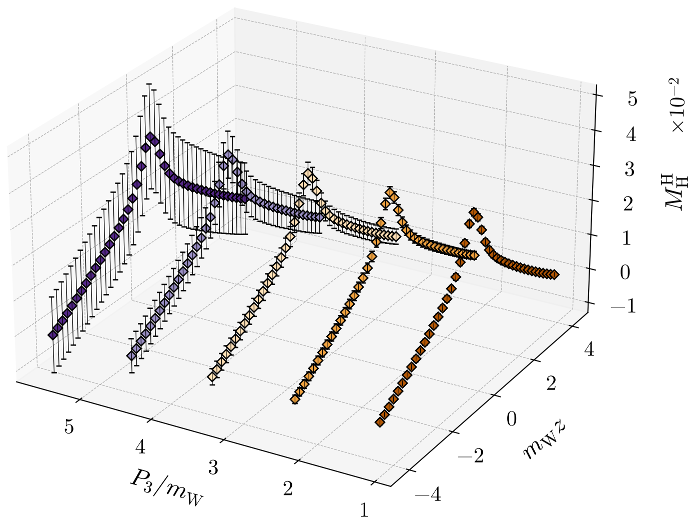

Fig. B.11.: Momentum dependence of the matrix element $M_{\mathrm{H}}^{\mathrm{H}}(z, P_3)$ for parameter Set 5 on the largest lattice volume $L = 28$

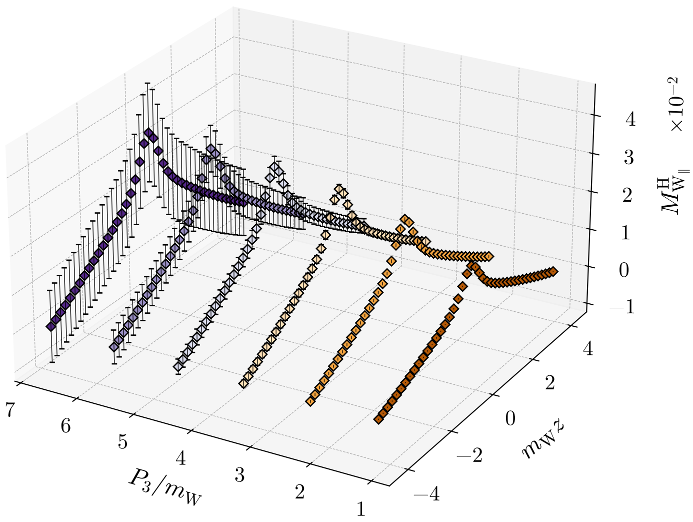

Fig. B.12.: Momentum dependence of the matrix element $M^{\mathrm{H}}_{\mathrm{W}_\parallel}(z, P_3)$ for parameter Set 5 on the largest lattice volume $L = 28$.

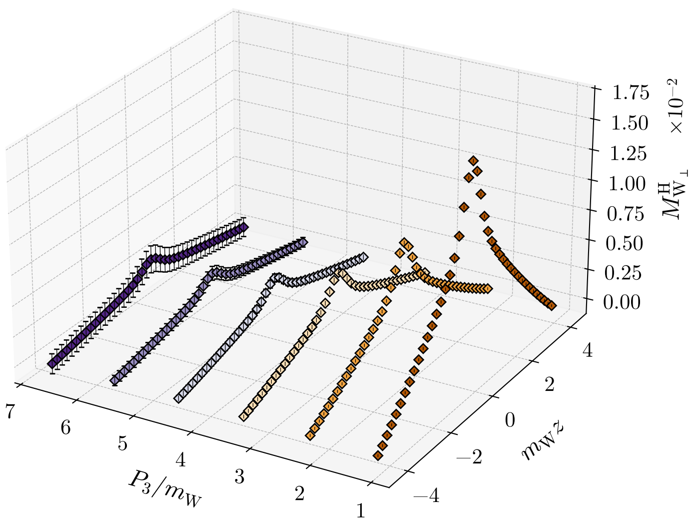

Fig. B.13.: Momentum dependence of the matrix element $M^{\mathrm{H}}_{\mathrm{W}_\perp}(z, P_3)$ for parameter Set 5 on the largest lattice volume $L = 28$.

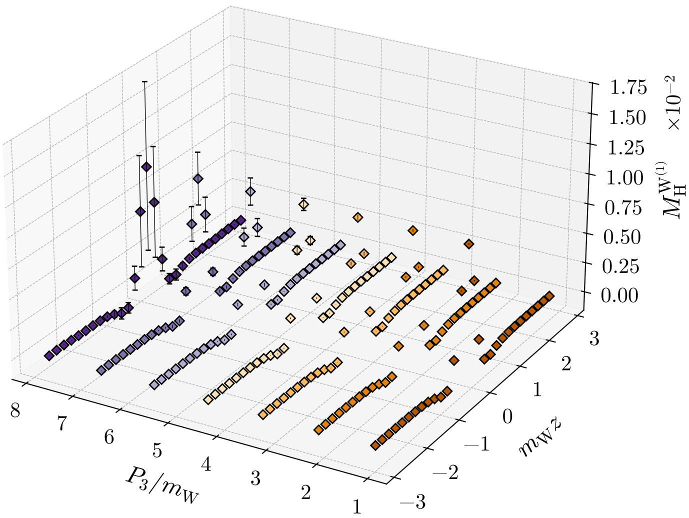

Fig. B.14.: Momentum dependence of the matrix element $M_{\mathrm{H}}^{\mathrm{W}^{(1)}}(z, P_3)$ for parameter Set 5 on the largest lattice volume $L = 28$

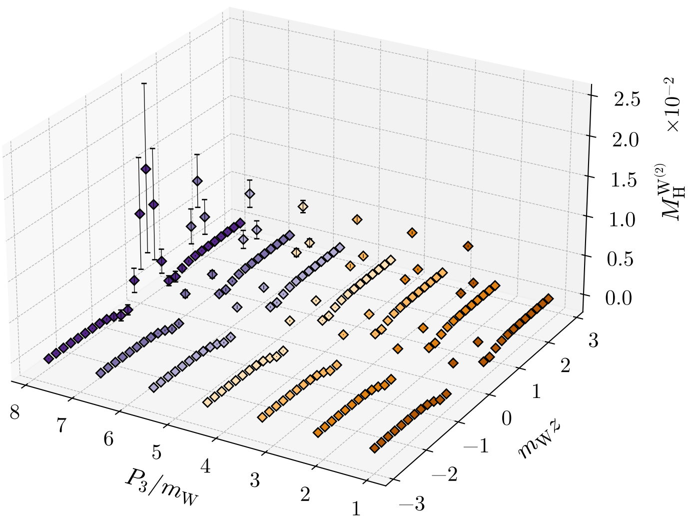

Fig. B.15.: Momentum dependence of the matrix element $M_{\mathrm{H}}^{\mathrm{W}^{(2)}}(z, P_3)$ for parameter Set 5 on the largest lattice volume $L = 28$.

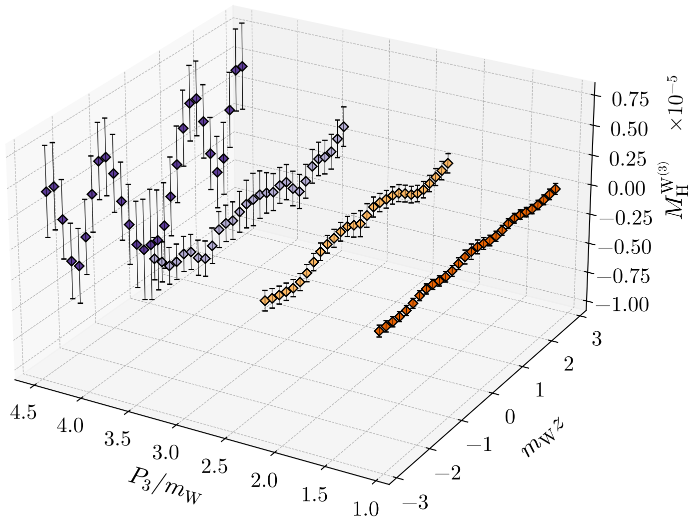

Fig. B.16.: Momentum dependence of the matrix element $M_{\mathrm{H}}^{\mathrm{W}^{(3)}}(z, P_3)$ for parameter Set 5 on the largest lattice volume $L = 28$.

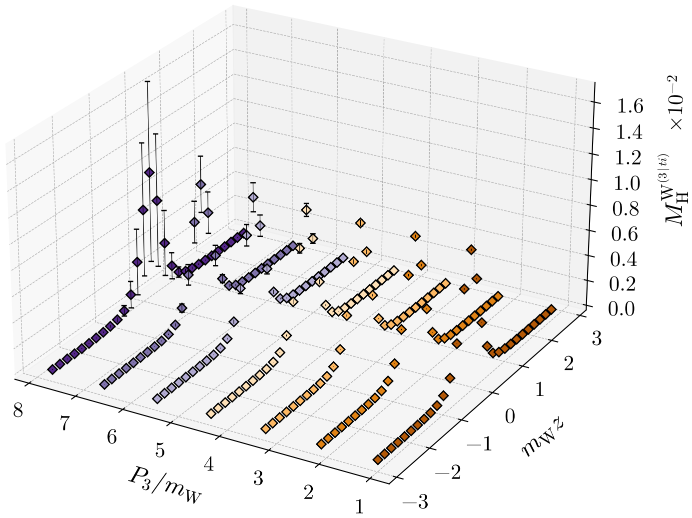

Fig. B.17.: Momentum dependence of the matrix element $M_{\mathrm{H}}^{\mathrm{W}^{(3\,|\,ti)}}(z, P_3)$ for parameter Set 5 on the largest lattice volume $L = 28$

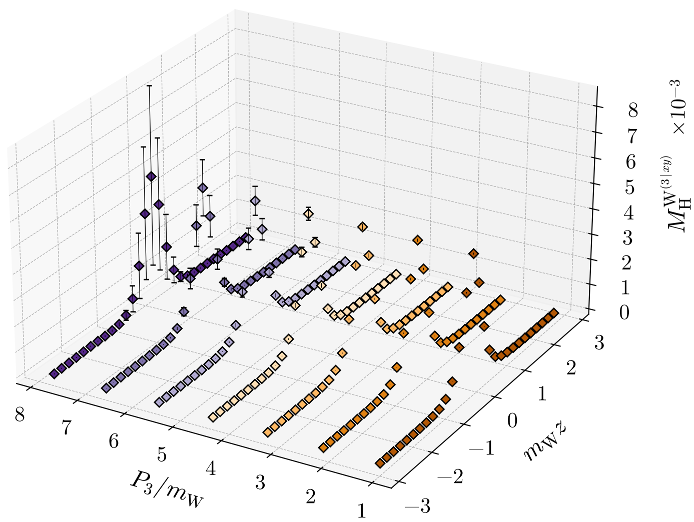

Fig. B.18.: Momentum dependence of the matrix element $M_{\mathrm{H}}^{\mathrm{W}(3\,|\,xy)}(z, P_3)$ for parameter Set 5 on the largest lattice volume $L = 28$.

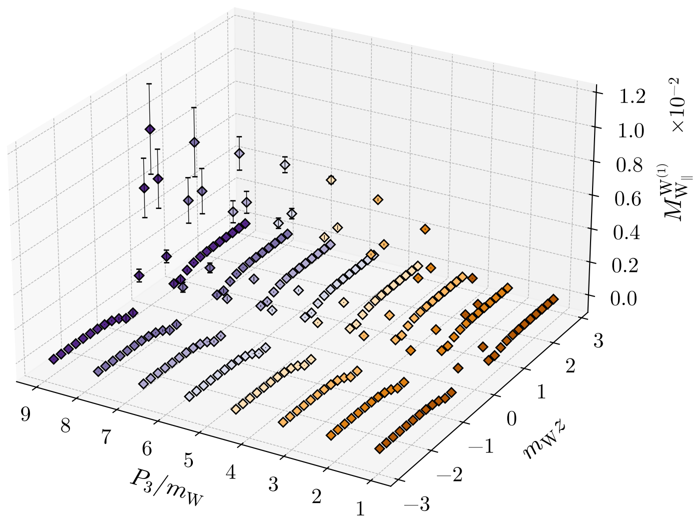

Fig. B.19.: Momentum dependence of the matrix element $M_{\mathrm{W}_\parallel}^{\mathrm{W}(1)}(z, P_3)$ for parameter Set 5 on the largest lattice volume $L = 28$.

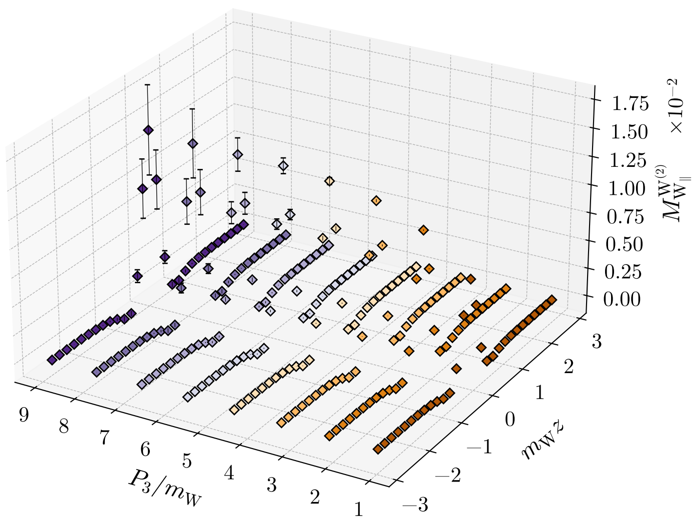

Fig. B.20.: Momentum dependence of the matrix element $M_{\mathrm{W}_\parallel}^{\mathrm{W}^{(2)}}(z, P_3)$ for parameter Set 5 on the largest lattice volume $L = 28$

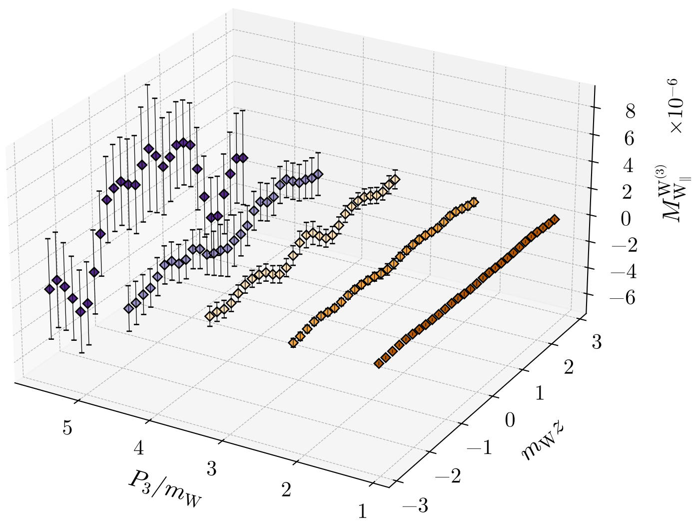

Fig. B.21.: Momentum dependence of the matrix element $M_{\mathrm{W}_\parallel}^{\mathrm{W}^{(3)}}(z, P_3)$ for parameter Set 5 on the largest lattice volume $L = 28$.

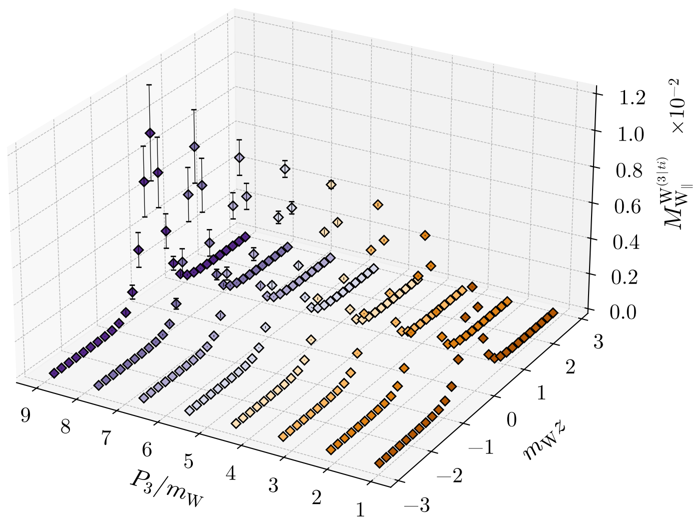

Fig. B.22.: Momentum dependence of the matrix element $M_{W_\parallel}^{W(3\,|\,ti)}(z, P_3)$ for parameter Set 5 on the largest lattice volume $L = 28$.

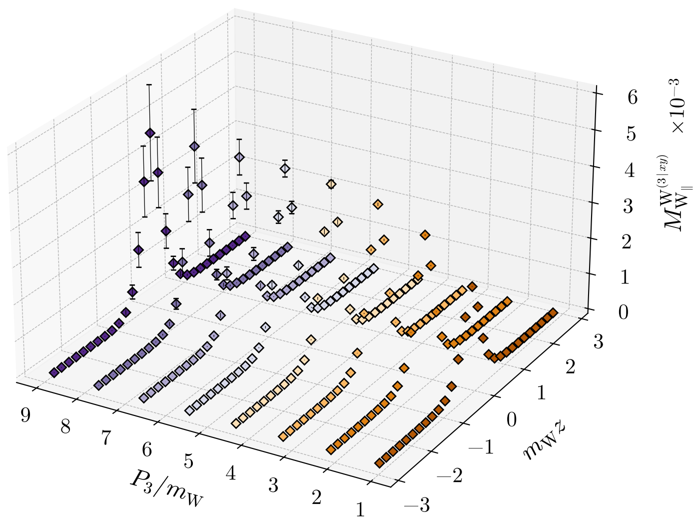

Fig. B.23.: Momentum dependence of the matrix element $M_{W_\parallel}^{W(3\,|\,xy)}(z, P_3)$ for parameter Set 5 on the largest lattice volume $L = 28$.

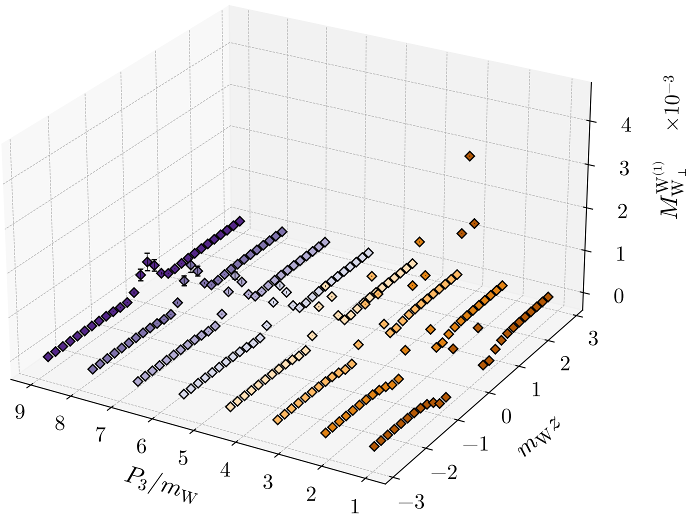

Fig. B.24.: Momentum dependence of the matrix element $M_{\mathrm{W}_\perp}^{\mathrm{W}^{(1)}}(z, P_3)$ for parameter Set 5 on the largest lattice volume $L = 28$.

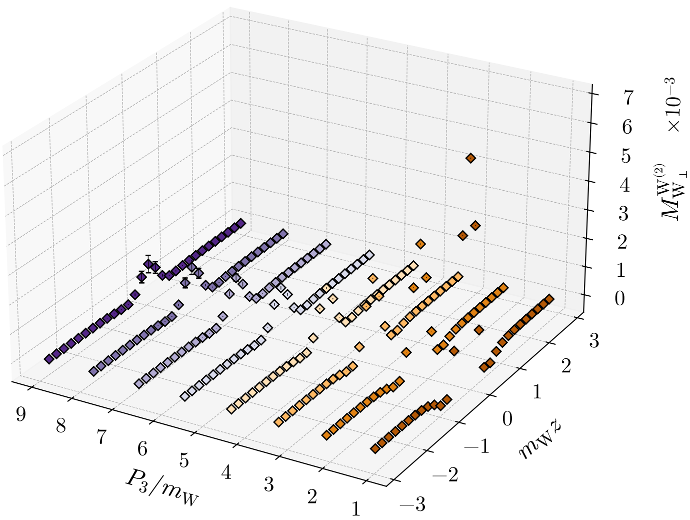

Fig. B.25.: Momentum dependence of the matrix element $M_{\mathrm{W}_\perp}^{\mathrm{W}^{(2)}}(z, P_3)$ for parameter Set 5 on the largest lattice volume $L = 28$

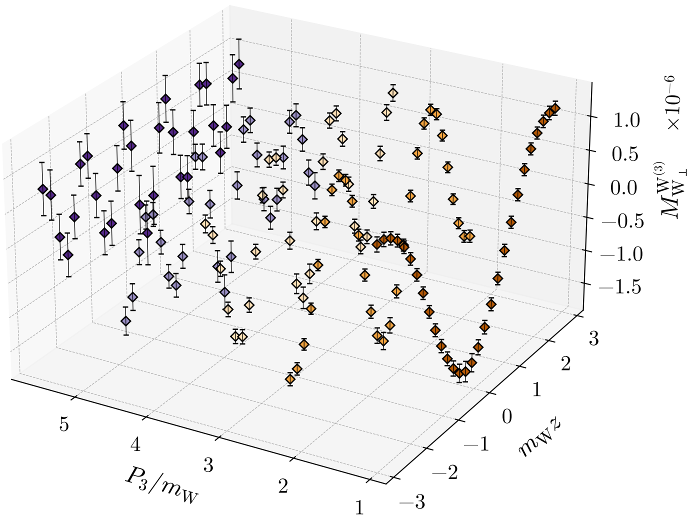

Fig. B.26.: Momentum dependence of the matrix element $M_{\mathrm{W}_\perp}^{\mathrm{W}(3)}(z, P_3)$ for parameter Set 5 on the largest lattice volume $L = 28$.

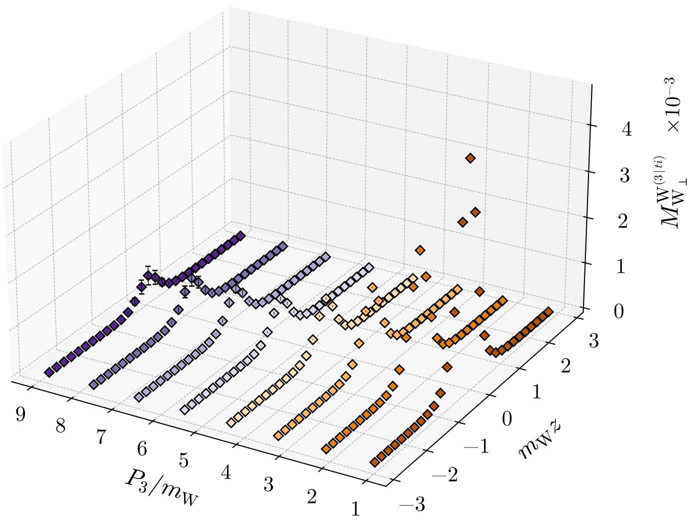

Fig. B.27.: Momentum dependence of the matrix element $M_{\mathrm{W}_\perp}^{\mathrm{W}(3\,|\,ti)}(z, P_3)$ for parameter Set 5 on the largest lattice volume $L = 28$.

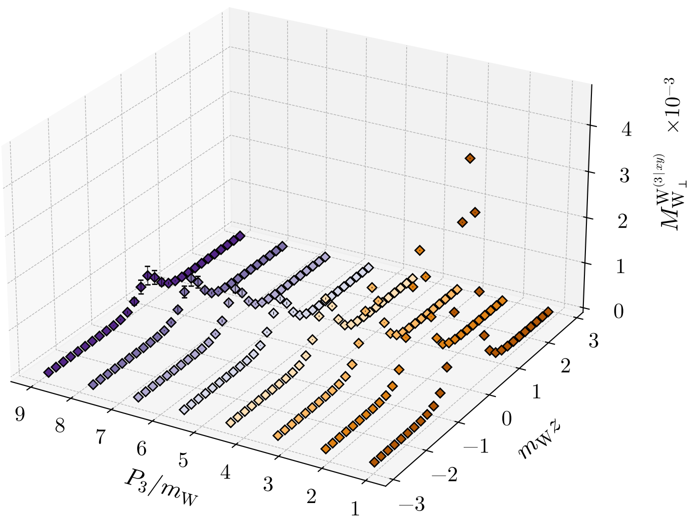

Fig. B.28.: Momentum dependence of the matrix element $M_{\mathrm{W}_\perp}^{\mathrm{W}(3\,|\,xy)}(z, P_3)$ for parameter Set 5 on the largest lattice volume $L = 28$.

B.6. Quasi-PDF Results for Set 5

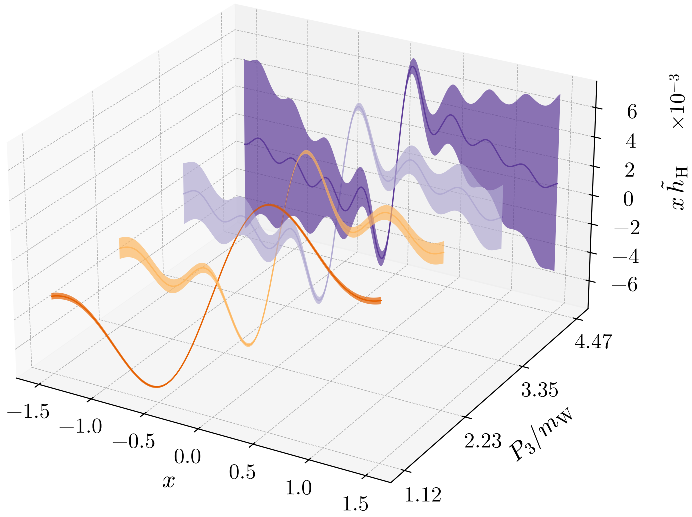

Fig. B.29.: Quasi-PDF $x\,\tilde{h}_{\mathrm{H}}(x, P_3)$ as a function of x and P_3/m_{W} (Set 5, $L = 28$).

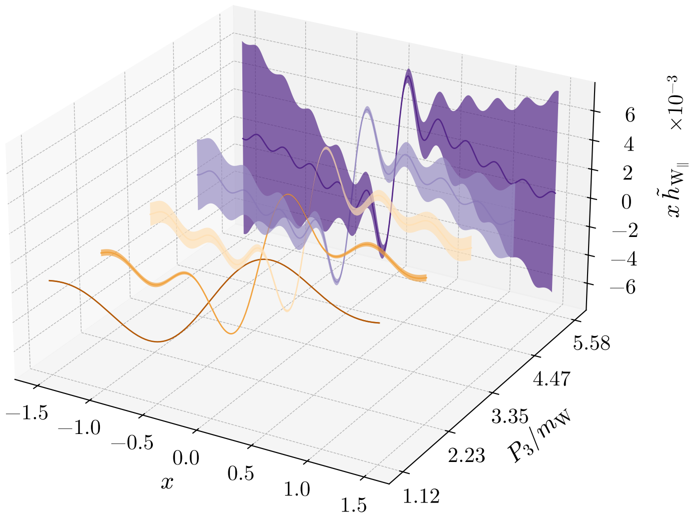

Fig. B.30.: Quasi-PDF $x\,\tilde{h}_{\mathrm{W}_\parallel}(x, P_3)$ as a function of x and P_3/m_{W} (Set 5, $L = 28$).

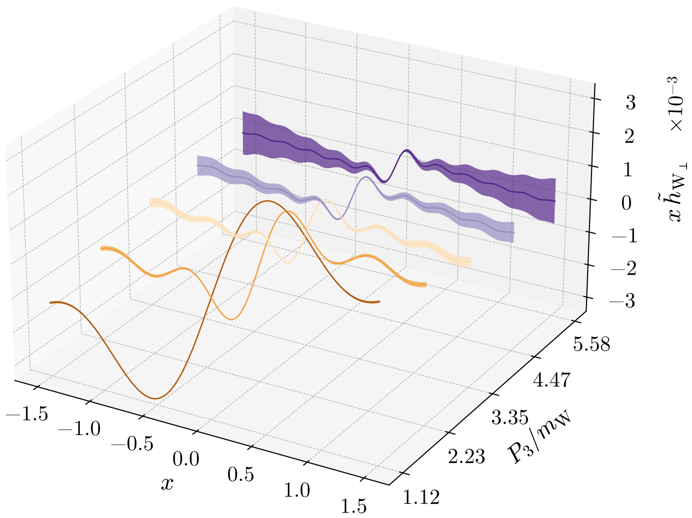

Fig. B.31.: Quasi-PDF $x\,\tilde{h}_{\mathrm{W}_\perp}(x, P_3)$ as a function of x and P_3/m_{W} (Set 5, $L = 28$).

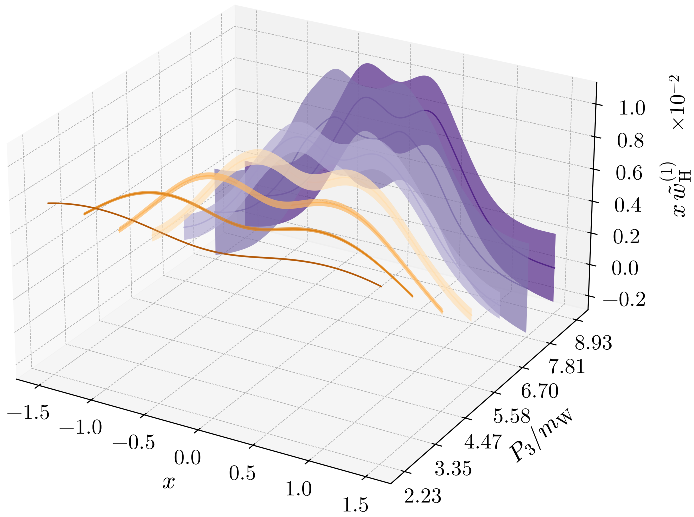

Fig. B.32.: Quasi-PDF $x\,\tilde{w}_{\mathrm{H}}^{(1)}(x, P_3)$ as a function of x and P_3/m_{W} (Set 5, $L = 28$).

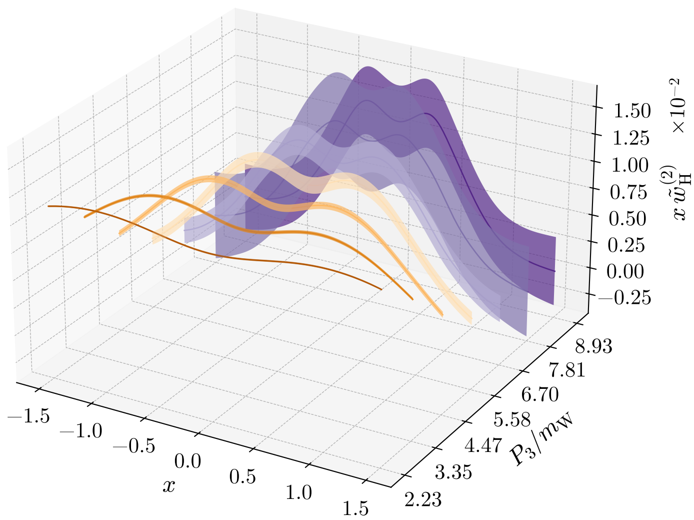

Fig. B.33.: Quasi-PDF $x\,\tilde{w}_{\mathrm{H}}^{(2)}(x, P_3)$ as a function of x and P_3/m_{W} (Set 5, $L = 28$).

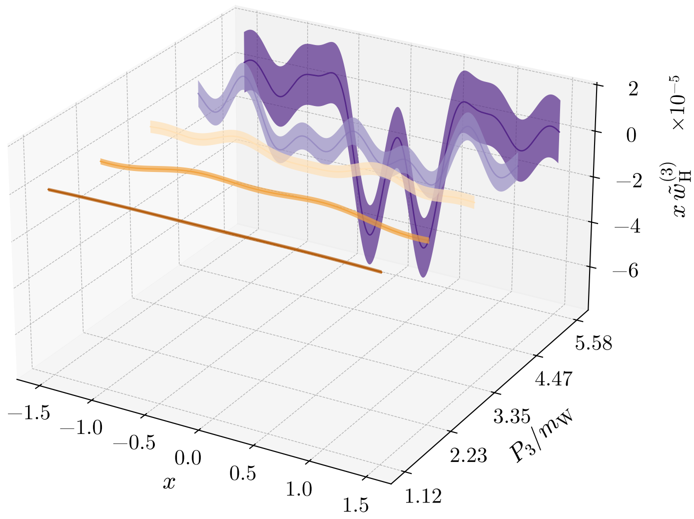

Fig. B.34.: Quasi-PDF $x\,\tilde{w}_{\mathrm{H}}^{(3)}(x, P_3)$ as a function of x and P_3/m_{W} (Set 5, $L = 28$).

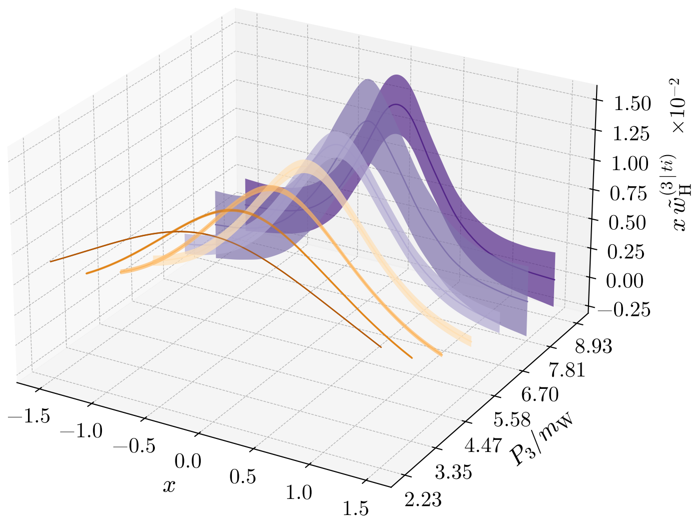

Fig. B.35.: Quasi-PDF $x\,\tilde{w}_{\mathrm{H}}^{(3\,|\,ti)}(x, P_3)$ as a function of x and P_3/m_{W} (Set 5, $L = 28$).

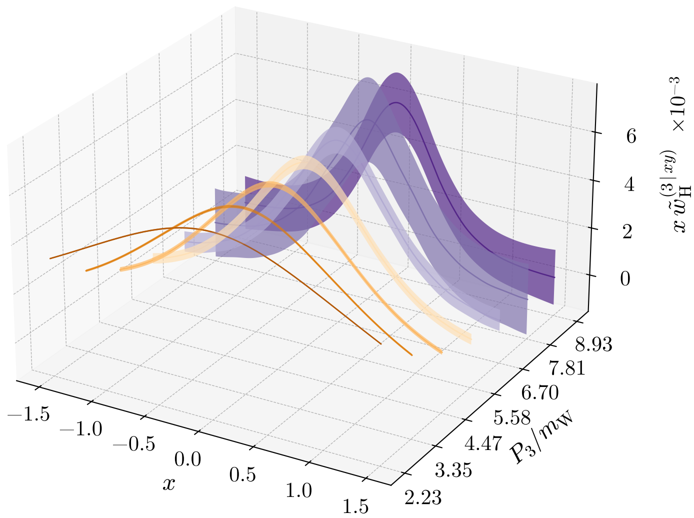

Fig. B.36.: Quasi-PDF $x\,\tilde{w}_\mathrm{H}^{(3\,|\,xy)}(x, P_3)$ as a function of x and P_3/m_W (Set 5, $L = 28$).

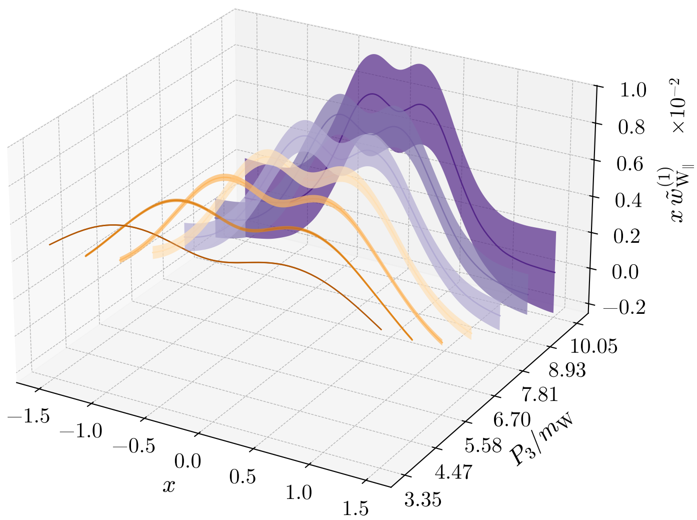

Fig. B.37.: Quasi-PDF $x\,\tilde{w}_{\mathrm{W}_\parallel}^{(1)}(x, P_3)$ as a function of x and P_3/m_W (Set 5, $L = 28$).

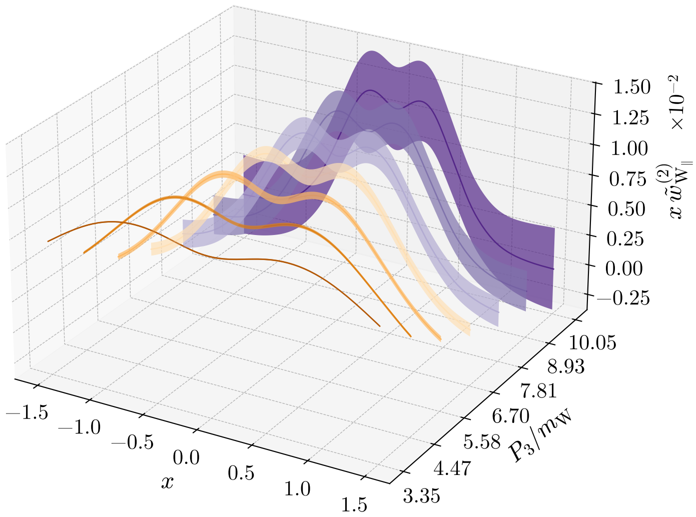

Fig. B.38.: Quasi-PDF $x\,\tilde{w}^{(2)}_{\mathrm{W}_\parallel}(x, P_3)$ as a function of x and P_3/m_W (Set 5, $L = 28$).

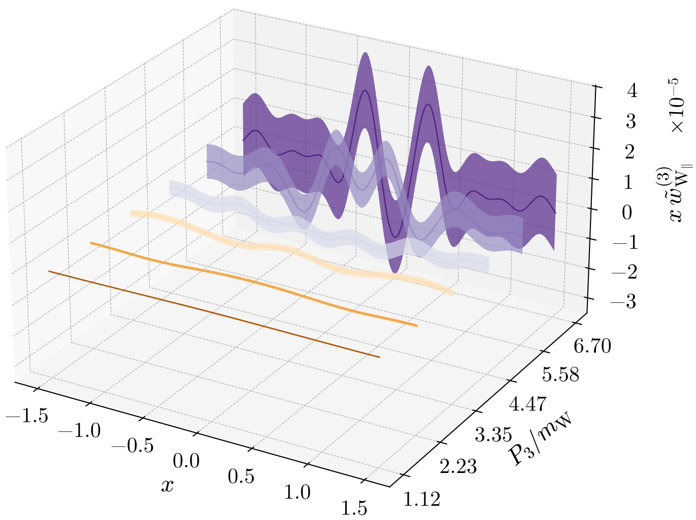

Fig. B.39.: Quasi-PDF $x\,\tilde{w}^{(3)}_{\mathrm{W}_\parallel}(x, P_3)$ as a function of x and P_3/m_W (Set 5, $L = 28$).

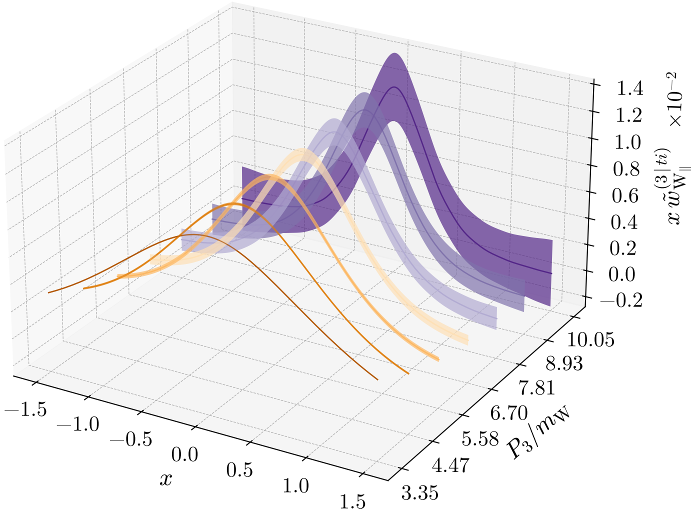

Fig. B.40.: Quasi-PDF $x\,\tilde{w}^{(3\,|\,ti)}_{\mathrm{W}_\parallel}(x, P_3)$ as a function of x and P_3/m_W (Set 5, $L = 28$).

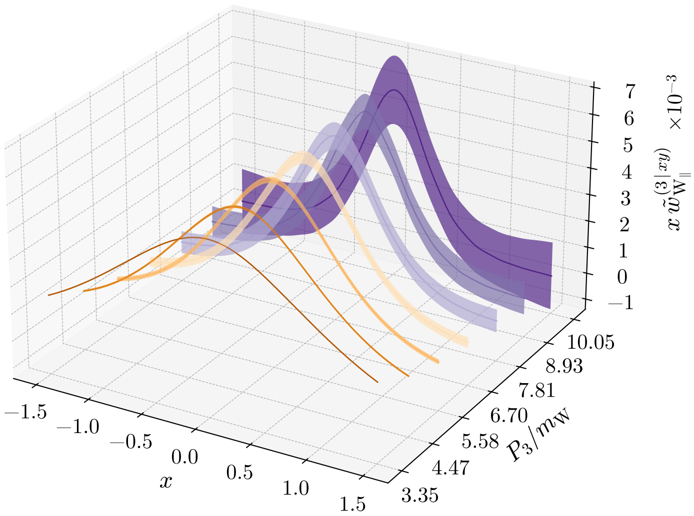

Fig. B.41.: Quasi-PDF $x\,\tilde{w}^{(3\,|\,xy)}_{\mathrm{W}_\parallel}(x, P_3)$ as a function of x and P_3/m_W (Set 5, $L = 28$).

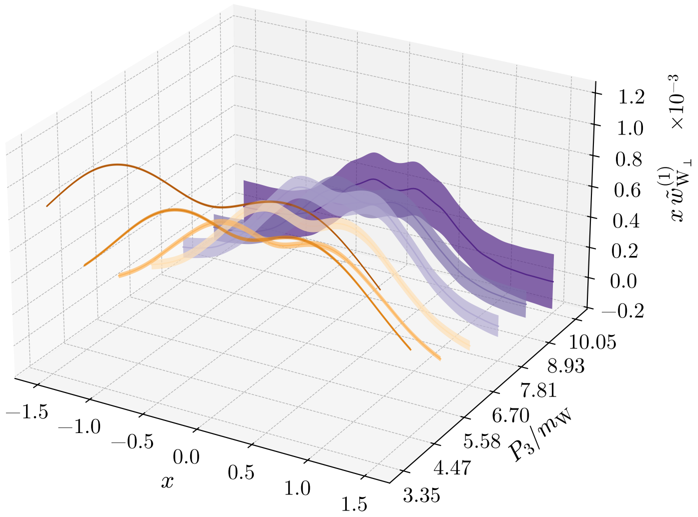

Fig. B.42.: Quasi-PDF $x\,\tilde{w}^{(1)}_{\mathrm{W}_\perp}(x, P_3)$ as a function of x and P_3/m_W (Set 5, $L = 28$).

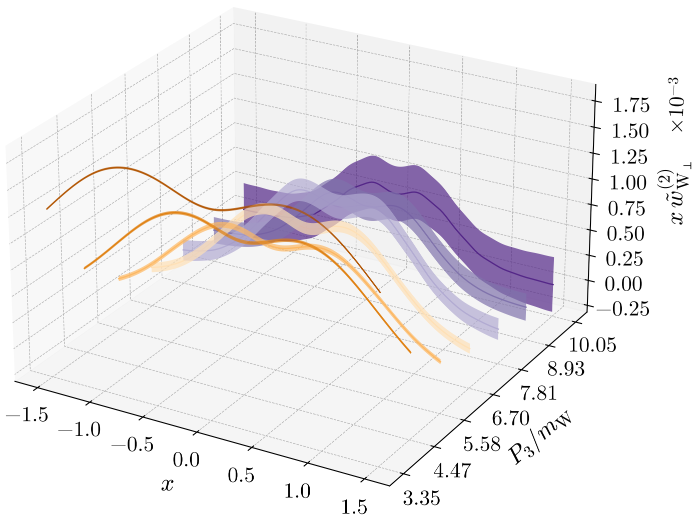

Fig. B.43.: Quasi-PDF $x\,\tilde{w}^{(2)}_{\mathrm{W}_\perp}(x, P_3)$ as a function of x and P_3/m_W (Set 5, $L = 28$).

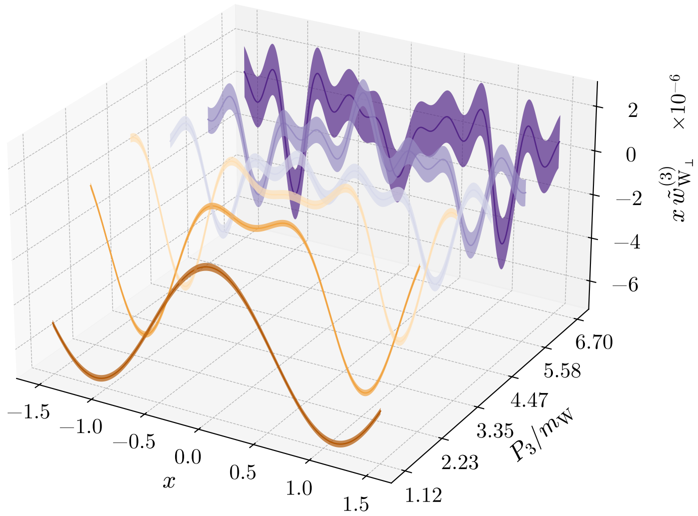

Fig. B.44.: Quasi-PDF $x\,\tilde{w}^{(3)}_{\mathrm{W}_\perp}(x, P_3)$ as a function of x and P_3/m_W (Set 5, $L = 28$).

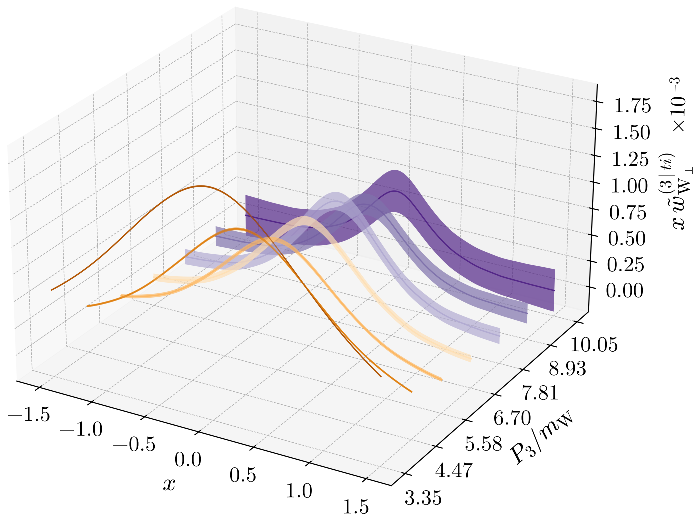

Fig. B.45.: Quasi-PDF $x\,\tilde{w}^{(3\,|\,ti)}_{\mathrm{W}_\perp}(x, P_3)$ as a function of x and P_3/m_W (Set 5, $L = 28$).

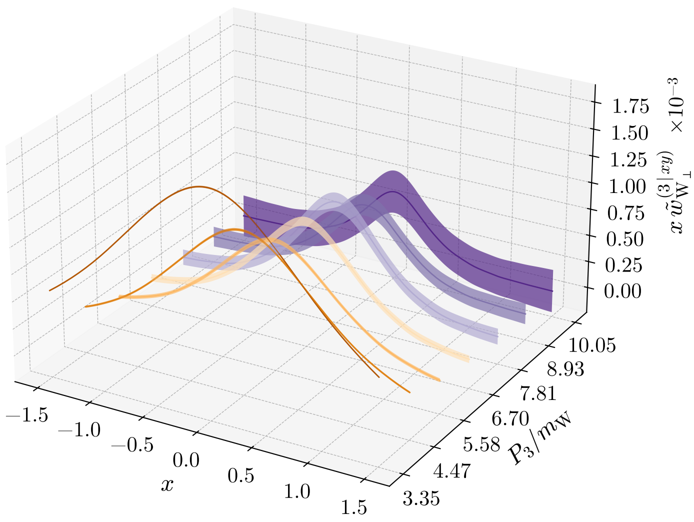

Fig. B.46.: Quasi-PDF $x\,\tilde{w}_{\mathrm{W}_\perp}^{(3\,|\,xy)}(x, P_3)$ as a function of x and P_3/m_W (Set 5, $L = 28$).

AFFIDAVIT

I declare that I have authored this thesis independently, that I have not used other than the declared sources/resources, and that I have explicitly indicated all material which has been quoted either literally or by content from the sources used. The text document uploaded to UNIGRAZonline or TUGRAZonline is identical to the present master's thesis.

Graz, June 21, 2026

Patrick Jenny